


Summer 2011

Excitation-Induced Ge Quantum Dot Growth on Si(100)-2X1 by Pulsed Laser Deposition

Ali Oguz Er
Old Dominion University

Follow this and additional works at: https://digitalcommons.odu.edu/physics_etds

 Part of the [Condensed Matter Physics Commons](#), [Materials Science and Engineering Commons](#), and the [Optics Commons](#)

Recommended Citation

Er, Ali O.. "Excitation-Induced Ge Quantum Dot Growth on Si(100)-2X1 by Pulsed Laser Deposition" (2011). Doctor of Philosophy (PhD), dissertation, Physics, Old Dominion University, DOI: 10.25777/6jwv-nk16
https://digitalcommons.odu.edu/physics_etds/46

This Dissertation is brought to you for free and open access by the Physics at ODU Digital Commons. It has been accepted for inclusion in Physics Theses & Dissertations by an authorized administrator of ODU Digital Commons. For more information, please contact digitalcommons@odu.edu.

EXCITATION-INDUCED GE QUANTUM DOT GROWTH ON SI(100)-2X1 BY
PULSED LASER DEPOSITION

by

Ali Oguz Er
M.S. May 2005, Old Dominion University
B.Sc. December 2003, Middle East Technical University, Turkey

A Dissertation Submitted to the Faculty of
Old Dominion University in Partial Fulfillment of the
Requirements for the Degree of

DOCTOR OF PHILOSOPHY

PHYSICS

OLD DOMINION UNIVERSITY
August 2011

Approved by:

Lepsha Vuskovic (Director)

Hani Elsayed-Ali (Co-Director)

Alex Odunov (Member)

Moskov Amarian (Member)

Gon Namkoong (Member)

ABSTRACT

EXCITATION-INDUCED GE QUANTUM DOT GROWTH ON SI(100)-2X1 BY PULSED LASER DEPOSITION

Ali Oguz Er

Old Dominion University, 2011

Director: Prof. Dr. Hani Elsayed-Ali

Self-assembled Ge quantum dots (QD) are grown on Si(100)-(2×1) with laser excitation during growth processes by pulsed laser deposition (PLD). *In situ* reflection-high energy electron diffraction (RHEED) and post-deposition atomic force microscopy (AFM) are used to study the growth dynamics and morphology of the QDs. A Q-switched Nd:YAG laser ($\lambda = 1064$ nm, 40 ns pulse width, 5 J/cm² fluence, and 10 Hz repetition rate) were used to ablate germanium and irradiate the silicon substrate. Ge QD formation on Si(100)-(2x1) with different substrate temperatures and excitation laser energy densities was studied. The excitation laser reduces the epitaxial growth temperature to 250 °C for a 22 ML film. In addition, applying the excitation laser to the substrate during the growth changes the QD morphology and density and improves the uniformity of quantum dots fabricated at 390 °C. At room temperature, applying the excitation laser during growth decreases the surface roughness although epitaxial growth could not be achieved.

We have also studied the surface diffusion coefficient of Ge during pulsed laser deposition of Ge on Si(100)-(2x1) with different excitation laser energy densities. Applying the excitation laser to the substrate during the growth increases the surface diffusion coefficient, changes the QD morphology and density, and improves the size uniformity of the grown quantum dots.

To study the effect of high intensity ultrafast laser pulses, Ge quantum dots on Si(100) were grown in an ultrahigh vacuum (UHV) chamber (base pressure $\sim 7.0 \times 10^{-10}$ Torr) by femtosecond pulsed laser deposition. The results show that excitation laser reduces the epitaxial growth temperature to ~ 70 °C. This result could lead to nonthermal method to achieve low temperature epitaxy which limits the redistribution of impurities, reduces intermixing in heteroepitaxy, and restricts the generation of defects by thermal stress.

We have ruled out thermal effects and some of the desorption models. Although further studies are needed to elucidate the mechanism involved, a purely electronic mechanism of enhanced surface diffusion of Ge atoms is proposed.

© Copyright, 2011, by Ali Oguz Er, All Rights Reserved

This thesis is dedicated to Mehmet Fatih Karatoprak.

ACKNOWLEDGEMENTS

First and foremost I would like to thank to my advisor Hani E. Elsayed-Ali. It has been an honor for me to be his PhD student. I appreciate all his contributions of time, ideas, funding to make my PhD studies productive and stimulating. He was my biggest chance during my academic training at ODU. I wish him all success and happiness. I am also thankful for the excellent example he has provided as a successful scientist and professor.

I am grateful to all those who have given me their friendship and provided me with lifts and practical helps. I am particularly indebted to Serkan, Bayram, Islam, Mustafa, Ashraf, Hasan Cinar and others for supporting me during my entire work.

I particularly thank to Yuksel Ufuktepe who increased our productivity and helped to get through during tough times. His contribution to our NbN work is utmost importance. We wouldn't be very successful without his supervision and experience.

I'd like to thank my entire committee for taking the time to review my dissertation and providing valuable insight and suggestions. I'm honored to have obtained the seal of approval from Lepsha Vuskovic, Alex Godunov, Gon Namkoong, and Moskov Amarian.

Lastly, I would like to thank to my family for all their love and encouragement. For my parents who raised me in very difficult situations and supported me in all my pursuit. I also want to thank to my beloved brother Emin and sister Zeynep for their presence and continuous support. I am thankful for the love, support, help and friendship I received from my wife Aynur whose support during my Phd thesis is greatly appreciated. And I am thankful for my children, Alper Yusuf and Sena Bahar, whom I love and adore. I

can't imagine a life without them I can't describe my love for them. Words are just not enough. I can't explain. I wish all the best for their life.

I am eternally grateful for all the wonderful things God has given me and shown me - not material things but life, friends, family, insight into my life, and the ability to love and be loved. The list is endless! He is truly the greatest and He is truly the way to all that is good!

TABLE OF CONTENTS

	Page
LIST OF TABLES	ix
LIST OF FIGURES	x
INTRODUCTION	1
PULSED LASER DEPOSITION	8
INTRODUCTION	11
MECHANISM OF PULSED LASER DEPOSITION	11
PARTICULATE FORMATION	20
REFLECTION HIGH-ENERGY ELECTRON DIFFRACTION	22
INTRODUCTION	22
RHEED SETUP AND ALTERNATIVES	24
RHEED THEORETICAL MODEL	28
OBTAINING RHEED PATTERNS	36
INDEXING RHEED PATTERNS	39
THE SCANNING TUNNELING MICROSCOPE	45
OVERVIEW	45
THEORY	48
INSTRUMENTATION	51
SI(100) SURFACE	55
EXCITATION-INDUCED GERMANIUM QUANTUM DOT FORMATION ON SI(100)-(2X1)	57
INTRODUCTION	57
EXPERIMENT	59
RESULTS AND DISCUSSIONS	61
CONCLUSION	86
ELECTRONICALLY ENHANCED SURFACE DIFFUSION DURING GE GROWTH ON SI(100)	88
INTRODUCTION	88
EXPERIMENT	90
RESULTS AND DISCUSSIONS	91
CONCLUSION	102

	Page
LOW TEMPERATURE EPITAXIAL GROWTH OF GE QUANTUM DOT ON SI(100)-(2X1) BY FEMTOSECOND LASER EXCITATION	104
INTRODUCTION	104
EXPERIMENT	104
RESULTS	106
DISCUSSIONS.....	109
CONCLUSION.....	111
THE PULSED LASER ASSISTED GROWTH OF GE QUANTUM DOT ON SI(100)- 2X1: A STM STUDY	113
INTRODUCTION	104
EXPERIMENT	116
RESULTS AND DISCUSSIONS.....	117
CONCLUSION.....	124
CONCLUSIONS.....	126
RHEED	126
STM	127
BIBLIOGRAPHY.....	129
APPENDIXES	146
VITA	178

LIST OF TABLES

Table	Page
1. Data extracted from Fig. 7	41
2. Interplanar distances	41
3. Comparison of the angles.....	43

LIST OF FIGURES

Figure	Page
1. Lycurgus Chalice	1
2. A typical PLD mechanism	8
3. Mechanism of Pulsed Laser Deposition	12
4. A typical RHEED mechanism	22
5. Kinematic theory of RHEED	30
6. (a) Diamond structure of silicon	37
7. The expected XRD pattern of Ge crystal	40
8. Transmission RHEED pattern of Ge QD.....	40
9. Indexed transmission pattern of Ge QD.....	43
10. Basic principles of STM	46
11. Manipulating the surface by STM	47
12. Filled and empty states in tip and sample	48
13. Clean reconstructed Si(100) surface	55
14. (a) RHEED pattern at different deposition times for a substrate temperature of 390 °C.	62
15. (a) RHEED pattern obtained at different deposition times.....	64
16. (a) For deposition at 250 °C without an excitation laser, the RHEED pattern decays continuously with coverage resulting in a diffuse pattern..	66
17. (a) RHEED pattern of 22 ML Ge deposited at 250 °C with an excitation laser of 37 ± 4 mJ/cm^2 shows a transmission pattern.	67

18. (a) RHEED pattern of 22 ML Ge deposited at 250 °C with an excitation laser of 77 ± 7 mJ/cm ²	68
19. (a) RHEED patterns recorded at different Ge coverage deposited at 250 °C with an ablation laser of 5 J/cm ² and an excitation laser of 106 ± 10 mJ/cm ²	70
20. (a) RHEED patterns recorded at different Ge coverage deposited at room temperature with an ablation laser energy density of 5 J/cm ² and corresponding AFM image of the final 22 ML Ge film.....	73
21. Intensity of the specular spot after termination of Ge deposition with the substrate maintained at 250 °C for a Ge coverage of ~22 ML.....	74
22. The excitation laser energy density is (a) 18 ± 2 mJ/cm ² , (b) 40 ± 4 mJ/cm ² , (c) 52 ± 5 mJ/cm ² , (d) 70 ± 7 mJ/cm ² , (e) 90 ± 10 mJ/cm ² , (f) 106 ± 10 mJ/cm ²	92
23. The AFM images of the individual islands with excitation energy density of (a) 18 ± 2 mJ/cm ² , (b) 40 ± 4 mJ/cm ² , (c) 52 ± 5 mJ/cm ² , (d) 70 ± 7 mJ/cm ² , (e) 90 ± 10 mJ/cm ² , (f) 106 ± 10 mJ/cm ²	93
24. The surface diffusion coefficient versus excitation laser energy density after 8000 deposition pulses (22 ML)..	96
25. RHEED patterns during Ge deposition on Si(100)-(2x1) at ~70 °C with excitation laser of ~30 mJ/cm ²	106
26. (a) AFM image and line scans of two islands, and (b) its corresponding Ge quantum dot size distribution for film grown at 70 °C with excitation.	107
27. RHEED pattern and AFM image of Ge quantum dots on Si(100)-(2x1) grown at 70 °C without the excitation laser.....	108
28. Clean Si(100)-2x1 surface with 40x40 nm ² area	117

29. Two-dimensional STM image with 500x500 nm ² area obtained at 250 °C.	118
30. Three-dimensional STM image with 500x500 nm ² area obtained at 250 °C.	119
31. Ge coverage on Si(100) at (a) 2 ML, (b) 4 ML, (c) 5 ML, and (d) 6 ML when 75 5 mJ/cm ² excitation laser energy density was used	120
32. Individual islands when (a) 25 mJ/cm ² , (b) 50 mJ/cm ² , (c) 75 mJ/cm ² , and 100 mJ/cm ² is used.....	121
33. RHEED chamber top view.....	146
34. Sample manipulator	147
35. Sample manipulator and substrate holder.	148
36. Germanium target and target holder.	149
37. Lumonics YAG Master (YM) 200 laser system.	151
38. System design and components	153
39. Gate Valve	154
40. Carousel for samples and tips	155
41. Tip Holder	156
42. STM Matrix cable connections.....	157
43. PLD STM bake out	158
44. Matrix interface software	159
45. Absorption and emission spectra of Ti:Sapphire	165
46. Principle of chirped pulse amplification (CPA).....	167
47. Principle of pulse stretching using negative GVD.....	168
48. Photodiode signal from oscillator shows modelocking	170
49. Pulse train from amplifier	171

50. Amplifier beam path 172

CHAPTER I

INTRODUCTION

Although the study of nanomaterials has taken too much interest, nanomaterials has a long and rich history. The early civilizations have actually used nanoscale materials for many applications and. For example, pottery using nano-sized particles has been in use for thousands of years. The oldest known such object is thought to be the Lycurgus chalice, which dates back to the late fourth century A.D, shown in Figure 1.



FIG 1. Lycurgus Chalice.

The Roman chalice has a raised frieze showing the myth of King Lycurgus, and is made from glass which appears jade green in reflected light, but when light is shone directly through the glass it appears translucent red. This unusual optical effect is caused by 40ppm (parts per million) gold and 300 ppm silver contained within the glass producing 70nm particles. The colored glass for decorative purpose that contained embedded metallic nanoparticles was used by the Mesopotamian civilizations around 2500 B.C [1]. A special case of nanocrystals comprised of a semiconductor is known as quantum dot.

Quantum dots, also known as nanocrystals, are a special class of materials known as semiconductors, which are crystals composed of periodic groups of II-VI, III-V, or IV-VI materials. These tiny nano-scale dots can confine the electrons in a three-dimensional space. After exciting these electrons with light, they re-emit the light of a precise wavelength as they go back to lower energy levels. The dot's small size gives researchers incredibly unusual properties to investigate potential applications. In today's modern world, many important modern electronics industry applications such as LED and personal computer rely on semiconductors because their electrical conductivity can be greatly altered via external stimulus such as photon, ions, electrons and voltage etc. As new technologies start to rely more on semi-conductors, their shortcomings are more and more apparent. Conventional semi-conductors are used very frequently in electrical circuits, however; they have been found to be too big and too slow. Since they have limited ranges of tolerance for the frequency of the current they carry, the low tolerance of traditional semi-conductors often creates a problem to circuits, and many of its other applications. As engineers search for a faster and more compatible alternative to conventional semiconductors they have discovered quantum dots, a new form of semiconductors that model atoms. Quantum dots are so important because different quantum dots can be made to tolerate different current frequencies through a much larger range than conventional ones. Their uniqueness comes from their sizes, ranging from 1-40 nanometers (a billionth of a meter) in diameter, these pseudo-atoms take semiconductors to a whole new level and can allow devices to work almost at the speed of light. These truly amazing materials start to behave greatly different at such a small size. Because quantum dots' electron energy levels are discrete, which makes them zero

dimensional, rather than continuous, scientist could easily alter the bandgap by adding or removing of just a few atoms to the quantum dot. The band-gap of a quantum dot is what determines which frequencies it will respond to, so being able to change the band-gap is what gives scientists more control and more flexibility when dealing with its applications. Quantum dots of the same material, but with different sizes, can emit light of different colors. For example, smaller dots would emit blue light will larger ones will emit red light. The physical reason is the quantum confinement effect. The coloration is directly related to the energy levels of the quantum dot. It is the bandgap energy that determines the energy (and hence color) of the fluorescent light is inversely proportional to the square of the size of the quantum dot.

One of the many interesting possible applications will be for anti-counterfeiting solutions. The worldwide counterfeit goods trade, excluding counterfeit money, is believed to be on the order of \$1 trillion annually. The U.N. estimates counterfeit drug sales alone were over \$300 billion in 2008, while the World Customs Organization believes that other counterfeit goods sold for more than \$600 billion. The U.S. based Center for Medicines in the Public Interest predicts that counterfeit drug sales will reach \$75 billion globally in 2010, an increase of more than 90 percent from 2005. These losses practically cost hundreds of thousands jobs lost.¹ The secure solution comes from the handy miracle nanoparticles. This tiny zero dimensional light-emitting nanoparticles could protect goods from counterfeiting. Due to their particulate and nanoscale size, quantum dots can easily be blended with polymers, gels, or inks and printed onto most surfaces. The complexity of their manufacturing process also makes them almost

¹ <http://www.cbc.ca/news/interactives/map-counterfeit-goods/>

impossible to counterfeit. Since quantum dots are also highly stable, extremely bright and absorptive, they offer advancements in solid state lighting, solar collector and electronic display technology. They can be engineered to be responsive to a specific frequency of light and suspend them in ink that they would print onto money or any good. If we shine the light with the same frequency with ink solution has been engineered for, this will reveal whether or not the money is real or counterfeit.

The quantum dots have been successfully grown by self-assembly processes. Due to their longer carrier lifetime, reduction phonon scattering and lower detector noise, the quantum dot structures are good candidate for possible optoelectronic devices [2].

The self-assembled Ge quantum dots grown on Si substrates have a potential to be monolithically integrated with advanced Si-based technology comparing to other optoelectronic III-V and other materials. One of the requirement for quantum dot to be useful is their small size L , which directly related to lattice mismatch ϵ as $L \sim \epsilon^2$. Therefore, Ge on silicon has the highest possible lattice mismatch which makes the smallest possible dot size that can be achieved [3].

Growth of Ge on Si is a classical model of the Stranski-Krastanov growth-mode, also known as layer-plus-island growth, where growth starts in a uniform layer-by-layer growth up to ~ 3 monolayer [1 monolayer (ML) is equivalent to 6.78×10^{14} atoms/cm² on a Si(100) surface.] The lattice mismatch (misfit) between Ge and Si ($a_{\text{Ge}} = 0.566$ nm, $a_{\text{Si}} = 0.543$ nm) causes elastic strain which increases as the Ge film grows on the Si surface. With the increase of strain energy, the competition between chemical potential of the deposited film and strain energy eventually causes the film to continue through three-dimensional (3D) island growth beyond a critical layer thickness around 3 ML. The value

of the misfit is the key factor for the relief mechanism. Three dimensional island formation leads to a partial relaxation of strain. Those islands could be dislocation free or coherent and their shapes change during growth. The first faceted islands, in the shape of square-based pyramids or rectangular-based hut clusters with four facets, appear following completion of the wetting layer. Those huts are rectangular-shaped $\{105\}$ -faceted clusters with a contact angle $\sim 11^\circ$ with $\{100\}$ planes, whereas at higher temperatures another kind of multifaceted, larger dome-shape islands coexist with huts [4, 5]. While hut clusters are $\{105\}$ -faceted and have a 15-20 nm average size, the dome islands, are mainly bound by steeper facets such as $\{113\}$, $\{102\}$ making $\sim 25^\circ$ and 26° , respectively, with the substrate, and have an average size of 50-100 nm [6, 7]. The evolution of the $\{105\}$ -faceted hut clusters to $\{105\}$ -, $\{113\}$ -, and $\{15\ 3\ 23\}$ -faceted domes, is well documented along with the final larger $\{111\}$ -faceted superdomes containing dislocations [7]. It was shown that the $\{105\}$ facet is energetically favorable on smaller islands, while the $\{113\}$ facet is favorable on larger islands [8]. The shape of the initial islands was found to depend on the deposition technique. For example, if Sb is used as a surfactant in the molecular beam epitaxy (MBE) of Ge/Si(100), the initial island shape changes from $\{105\}$ -faceted to $\{117\}$ -faceted [9]. If Ge is grown by liquid phase epitaxy (LPE), $\{115\}$ -faceted islands are first observed instead of the $\{105\}$ -faceted ones, and as the coverage increases, $\{111\}$ -faceted pyramids are formed [10, 11].

Low temperature thin film growth is strongly desirable in microelectronic fabrication. In Si/Ge, it has been long recognized that one way to suppress misfit dislocations is by lowering the growth temperature [12]. To lower the epitaxial growth temperature, extrinsic assistance by energetic particles, such as ions, electrons and

photons, have been used to add energy to promote the migration of adsorbed atoms at the surface [13-15]. Pulsed laser induced electronic processes leading to surface structural modifications have been shown to occur when the laser intensity is below the melt threshold [16-19]. Recent scanning tunneling microscopy (STM) studies have demonstrated that laser pulses well below the melt and ablation thresholds induce bond rupture at individual atomic sites on several semiconductor surfaces via a process that is purely electronic [20-22]. The laser-induced electronic bond rupture causes structural changes on the surface which depend strongly on the surface studied.

PLD is a powerful technique for growing thin films from the vapor phase. A high power pulsed laser is focused onto a target of the material to be grown. As a result, a plume of vaporized material is emitted and then collected on the substrate. PLD has attracted too much attention for growing high quality films of superconductors [23-26], magnetoresistant materials [27-29], semiconductors [30-35], ferroelectrics [36-39] and many others. Compared to other vapor phase deposition methods, PLD is particularly suitable for multilayer growth, since the laser can be used to ablate different doped semiconductor targets, one after another, while growing the doped material in the form of thin films [40].

This dissertation is based on the journal publications [33, 34, 41] and is organized as follows. Chapter II presents an overview of PLD as a thin film deposition technique. In this chapter, an overview of pulsed deposition technique as well as theory behind it will be addressed. Chapter III gives information about the elements of reflection high-energy electron diffraction (RHEED), both theoretical and experimental. This chapter also contains detailed calculations of the Si(100) and Ge(100) reciprocal lattices and the

indexing of the electron transmission pattern resulting from diffraction through the Ge QD formed by PLD. In chapter IV, excitation-induced Ge quantum dot growth will be investigated by *in situ* RHEED and *ex situ* AFM. The effect of femtosecond laser pulse irradiation of Ge target during will growth process is studied. Surface diffusion during germanium deposition on silicon substrate will be examined by using RHEED recovery curve measurement technique. Chapter VI investigates the formation mechanism of germanium on silicon substrate under femtosecond laser ablation. Each chapter will be self-contained, having its own introduction, and conclusion.

CHAPTER II

PULSED LASER DEPOSITION

II. 1. INTRODUCTION

Pulsed laser deposition (PLD) is a thin film deposition (specifically a physical vapor deposition, PVD) technique where a high-power pulsed laser beam is focused inside vacuum chamber to ablate the target of the desired composition. A typical PLD mechanism is shown in Fig. 2.

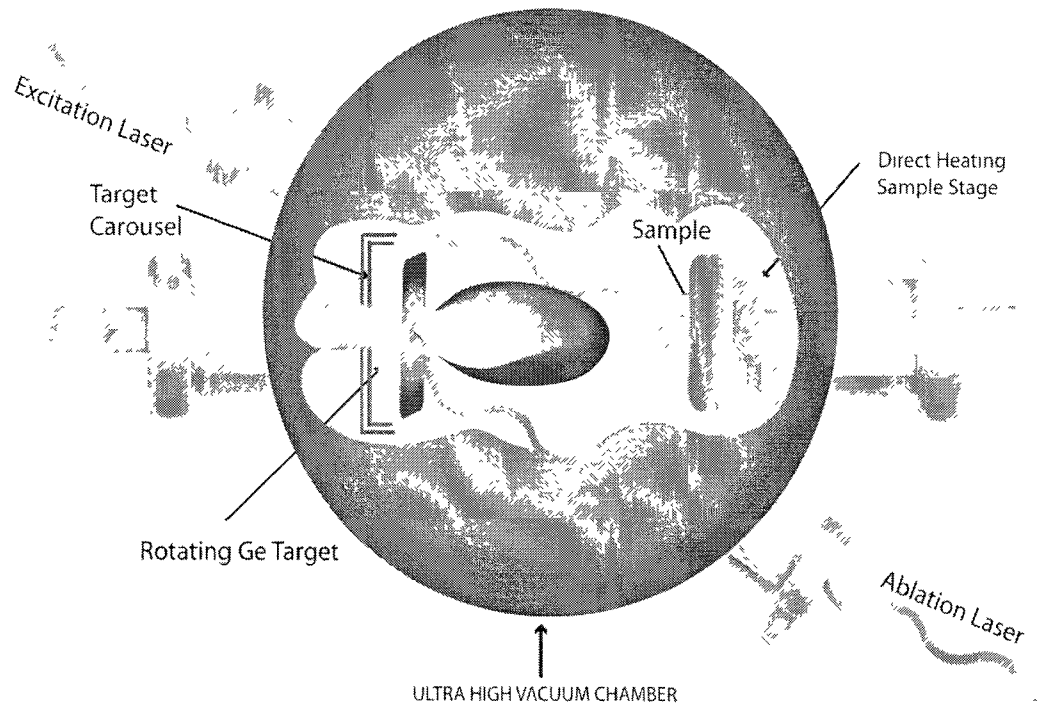


FIG. 2. A typical PLD mechanism.

Material is then vaporized from the target and deposited as a thin film on a substrate, such as a silicon wafer facing the target. This process can occur in ultra high vacuum or in the presence of a background gas, such as oxygen that is commonly used

when depositing oxides to fully oxygenate the deposited films [42, 43]. Laser ablation was first used in 1965 using ruby laser [44]. However, it wasn't until 1980's that it attracted too much attention in research lab. Parallel to developments in lasers, pulsed laser deposition (PLD) has become more and more popular in any research environment. PLD was the first technique used to deposit a superconducting $\text{YBa}_2\text{Cu}_3\text{O}_7$ thin film. Since that time, PLD has attracted too much attention for growing high quality films of superconductors [23-26], magnetoresistant materials [27-29, 45], semiconductors [30-34, 46], ferroelectrics [36-38] and many others. Among the interesting features of PLD are:

- (i) The high preservation of stoichiometry
- (ii) Its adaptability to grow multicomponent or multilayered films
- (iii) The ability to grow a thin film out of any material regardless of its melting point
- (iv) The high energy of the ablated particles may have beneficial effects on film properties
- (v) PLD consists of periods of high deposition rate (on the microsecond time scale $\sim 1\text{-}20 \mu\text{s}$) followed by periods of no deposition (on the millisecond to the second time scale), allowing for surface relaxation that may lead to producing smoother films
- (vi) Flexible, easy to implement
- (vii) Growth in any environment
- (viii) Greater control of growth
- (ix) Resonant interactions possible (i.e., plasmons in metals, absorption peaks in dielectrics and semiconductors)

Along with its advantageous features, PLD has also some major drawback that delays its use in industry. Those are, in particular:

- (i) the production of macroscopic eject during the ablation process;
- (ii) impurities in the target material;
- (iii) crystallographic defects in the film caused by bombardment by high kinetic energy ablation particles; and
- (iv) Inhomogeneous flux and angular energy distributions within the ablation plume.

Pulsed laser deposition may seem quite easy however it is actually a rather complex physical phenomenon when investigated deeply. The laser fluence and repetition rate are the parameters that most influence the stoichiometry and morphology. One of the big advantages of PLD is high instantaneous deposition rate. Low deposition rates could lead to long deposition times. For this reason, the experimental controls of PLD are often manipulated to maximize the deposition rate. The deposition rate can be increased by decreasing the target to substrate distance, or increasing the laser energy/fluence. Generally, it is easier to adjust the deposition rate by changing target-to-substrate distance than by changing laser energy. However, in certain cases, this option is limited due to the requirement of uniform deposition thickness. Alternatively, fluence could be increased since it could results in increased ablation volume, and hence increased deposition. However, it should be noted that under high fluence conditions unwanted ablation mechanisms may become important. In PLD, instantaneous deposition rate is $\sim 10^6$ ML/second due to short laser pulse duration and small temporal spread of the ablated species. It has been shown that plasma plume expands very rapidly ($\sim 10^6$ cm/s) to

the surface [47]. The plume expansion results in a plume width of around several microseconds at a 10 Hz repetition rate [48-50]. This results in an instantaneous deposition rate in the 100s of \AA s^{-1} . Rapid deposition of energetic species helps to raise the surface temperature. Therefore, lower temperature epitaxial growth could be achieved by PLD.

II. 2. MECHANISM OF PULSED LASER DEPOSITION

The mechanism of PLD can be divided four main stages, (a) initial laser interaction with target, (b) dynamics of the ablated species, (c) deposition of those species, and (d) nucleation and growth of on the substrate, as can be seen in Fig. 3. Each of those steps is material specific and as well as dependent on other experimental parameters such as pulse width, wavelength, background pressure, laser energy density, substrate type and deposition temperature. Those processes could be seen in the following Fig. 3.

II. 2. 1. LASER-TARGET INTERACTION

In the first stage of PLD, the laser beam is focused onto target to be ablated. Laser ablation can be categorized into various mechanisms such as photothermal, photochemical, hydrodynamical and exfoliation, and ultrafast laser ablation depending on the pulse width [42, 51, 52]. If the pulse width is longer than electron-phonon relaxation time and characteristic time of electron heat conduction time, ablation is considered as conventional equilibrium evaporation and thermal ablation. If pulse width is smaller than those equilibrium times, ablation is then considered as non-thermal and it contains many physical phenomena. In photothermal ablation, laser is absorbed by target and it heats up the lattice, which will then melts and vaporizes the target. For metal targets, laser absorption by free electrons takes place via an inverse Bremsstrahlung

mechanism. Thermalization of these hot electrons takes place through (i) heat transport into the bulk by thermal diffusion and (ii) electron-phonon coupling by transferring their energy to the lattice. However, in photochemical ablation, laser energy is directly absorbed by chemical bonds. And this mechanism generally requires higher energy than photothermal ablation. In hydrodynamical ablation, bulk material, particulate and droplets could be ejected due to ablation.

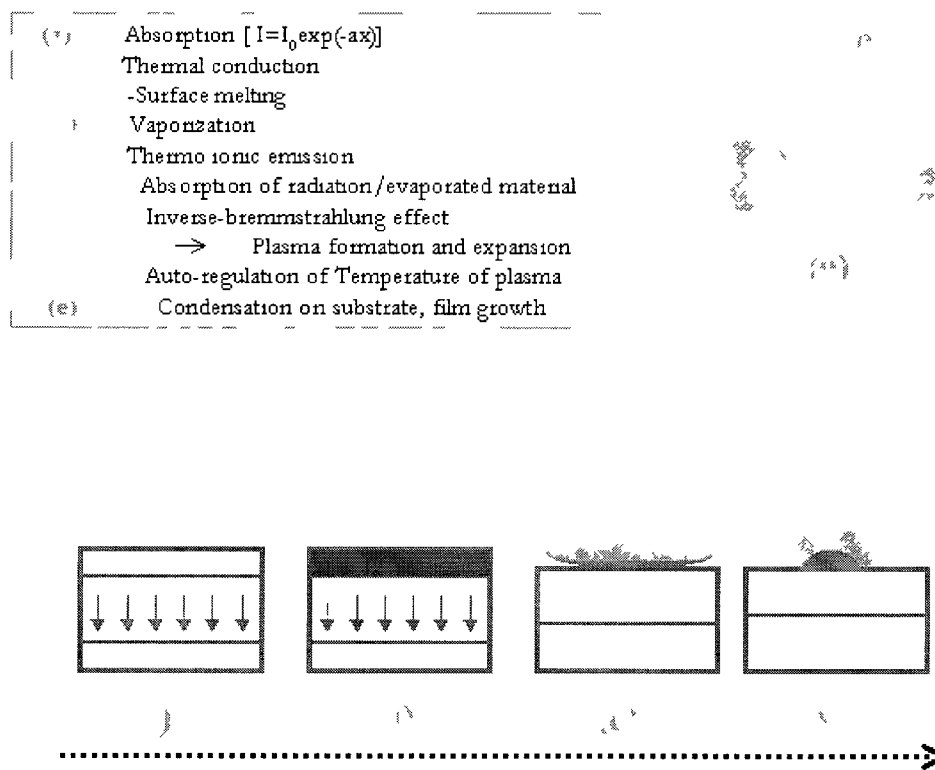


FIG. 3. Mechanism of Pulsed Laser Deposition.

Laser ablation generally occurs in nanosecond range while plume expansion is within microseconds. The target material will be ejected if the laser energy is higher than ablation threshold of the target.

At low laser flux in thermal ablation, the material is heated by the absorbed laser energy and evaporates or sublimates, whereas at high laser flux and short pulse duration, the material is typically converted to plasma. Ablation is related to direct transmission from solid to gaseous state without liquid phase and involves many physical phenomena such as collisional, thermal, and electrical excitation. Laser ablation induces the conversion of an initial electronic or vibrational photoexcitation into kinetic energy of nuclear motion, leading to the ejection of atoms, ions, molecules, and even clusters from a surface. It is possible to ablate material with a continuous wave laser beam if the laser intensity is high enough. The laser absorption depth and thus the amount of material removed by a single laser pulse depend on the material's optical properties and the laser wavelength. Given the laser pulse duration, one can estimate the *depth of heat penetration*, which is the distance that heat can be transferred to during the laser pulse $D=(4\alpha dT)^{1/2}$, where D is the depth of heat penetration α is the diffusivity of materials, dT is the pulse duration . Conversely, one can estimate the minimum pulse duration needed to penetrate a certain depth from the same formula [53].

When femtosecond pulses are used, processes related with ablation are greatly changed [51]. Femtosecond pulse duration is significantly smaller than electron-phonon coupling ($\sim 10^{-12}$ sec.), the conventional thermal deposition is also very limited, and thus ablation is considered direct solid-vapor transition. Therefore, it is considered as possible alternative solution for particulate formation during film growth [54, 55]. Some of the nonthermal ablation processes are: desorption induced electronic transition (DIET), collisional sputtering, hydrodynamic sputtering, and fracto emission [42, 44, 56-58]. The important parameters determining the effect of the laser pulse length on the ablation

process include: the heat diffusivity of the material, velocity of sound and the time scale for electron-electron thermalization and electron-phonon coupling, which was shown to be on the order of ~ 1 picosecond [59]. The important thermal processes, which occur in laser ablation, have been shown to be greatly modified once the laser pulses are shortened to a picosecond or femtosecond time scale [60, 61]. Due to better spatial concentration of ultrashort pulses compared to ns pulses, they decrease the required laser (threshold) fluence for ablation, increase the thermal gradient in the target, decrease the amount of energy lost to plasma and increase energy coupling to vaporize rather than melt the target.

II. 2. 2. PLUME FORMATION

In the second stage of laser ablation mechanism, the ablated material will form a plasma plume which will move toward to the sample due to Coulomb repulsion and recoil from target surface by following a cosine function of cone angle of plasma. This plasma is highly luminous, forward-directed, confined, and transient in nature and it can be deposited with less contamination than unconfined plasma in sputter deposition. Exploring the nature of the plume and its dependence on the properties of the ablating laser is important to understand how to control the growth of thin films by the PLD [42, 43]. Extensive theoretical and experimental work is being performed in order to study the characteristics of the plume, such as plume expansion, plasma density, energy distribution of species, and effect of background pressure on these parameters [62-64]. Properties of plume, such as degree of ionization, and temperature of plasma species can evolve quickly and strongly depending on many parameters such as the laser wavelength,

laser energy density and repetition rate, pulse duration, spot size on target, ambient gas composition and pressure, and target composition and surface quality [42].

Background gas affects the plasma plume parameters due to collision, attenuating, and thermalizing the plume species. Therefore, the background pressure effects important film parameters like deposition rate and kinetic energy distribution of adatoms [42]. Diagnostic of the laser-produced plasma [49, 65], can be used to understand and control the properties of the grown film [33].

As a rule of thumb, it has been found that fluencies two to three times higher than ablation threshold (which can be accurately enough approximated by the fluence which produces luminous plasma) are an optimum value and the substrate temperature should be at least higher than $0.3T_m$ [42], where T_m is the melting temperature in K, to obtain good crystallinity, although epitaxial films have been grown at lower temperatures than those used by other temperatures. However, lower deposition temperature will prevent or at least harmful film and/or ambient gas-substrate interaction, unwanted substrate interdiffusion processes and re-evaporation of volatile components. Increasing the laser energy usually results in two threshold effects: significant material removal and appearance of the luminous plasma plume. These threshold effects are most often described by evaporation and subsequent absorption of part of laser pulse by the vapor. The evaporation threshold can be understood by the exponential increase in the vapor pressure with the temperature predicted by the Clausius-Clapeyron relation equation.

$$P = A \exp(-\Delta H_{\text{vap}} / R T) \quad (1)$$

where R ($= 8.3145 \text{ J mol}^{-1} \text{ K}^{-1}$) and A are the gas constant. This is known as the Clausius-Clapeyron equation. If P_1 and P_2 are the pressures at two temperatures T_1 and T_2 , and ΔH_{vap} is the enthalpy of vaporization, the equation has following form:

$$\ln(P_1/P_2) = (-\Delta H_{\text{vap}} / R)(1/T_2 - 1/T_1) \quad (2)$$

The Clausius-Clapeyron equation allows us to estimate the vapor pressure at another temperature, if the vapor pressure is known at some temperature, and if the enthalpy of vaporization is known. Typical plasma temperatures measured by emission spectroscopy during the initial expansion $\sim 10,000 \text{ K}$, well above the boiling points of most materials ($\sim 3000 \text{ K}$). Heating of the plasma to these temperatures is thought to occur by inverse-Bremsstrahlung (IB) absorption of the laser light in a free-free transition of an electron-ion pair. The principle for IB is that when enough energy (in the form of photons) is moving through a small volume, the atoms in that volume become so excited that they are stripped of their electrons, becoming ionized. Higher still energy level rips apart the molecules, forming plasma. Absorption of a photon by an electron in the field of a nucleus, in another saying, when the electrons are present near the surface they strongly couple to the electromagnetic radiation and are accelerated and collide with any plasma ions or any nearby solid or gas phase atoms (inverse-Bremsstrahlung, IB) The initial ion and electron densities of the vaporized material from a target at its boiling temperature or higher are too small to account for significant IB absorption. The energy absorbed in the plasma is rapidly shared among the individual particles, raising their temperature and partially shielding the surface from further exposure to the laser pulse thus limiting the amount of material evaporated, decreasing the overall efficiency of the process. If more than one monolayer of the target gets evaporated per pulse then adjacent to the surface a

thin layer of vaporized material known as the Knudsen layer is formed, where vapor is not in translational equilibrium, exhibiting a half Maxwellian velocity distribution. Due to collisions among the atoms they acquire a full Maxwellian distribution with a center of mass velocity (10^4 ms^{-1}) and they propagate forward. The plasma clouds expand perpendicular to the target and cools down. Also, the degree of ionization is reduced due to recombination. The plasma will be thin and flat extending over area of the surface exposed to the laser pulse. Soon after its formation and until the end of the surface exposed to the laser pulse, it can be considered to be isothermal, with temperatures exceeding 10^3 K . Immediately after irradiation, the amount of the material augmenting the plasma will drop considerably. The plume will then expand preferentially away from target in the direction where the greatest density gradients are accelerating the species to top speeds of several kms^{-1} (up to 1000 times the usual speeds encountered during thermal evaporation). This expansion can push any existing gases away from target setting up a pressure wave.

The third stage of pulsed laser deposition determines the quality of the deposited films. The ejected high energy particles impinge onto substrate surface and start film formation once thermalized region is formed. These regions serve as source for condensation of particles. When condensation is high enough, a thermal equilibrium is reached and film grows on the substrate.

II. 2. 3. THIN FILM FORMATION

In the last stage of PLD, nucleation and growth processes occur. Those processes depend on many factors such as density, energy, ionization degree, target, substrate, as well as temperature and other environmental conditions. Processes in thin film formation

are following, in order: chemi- and physi-sorption, condensation, surface diffusion and nucleation. Depending on the surface energy between target and substrate, nucleation continues as layer by layer growth (Frank-Van der Merwe), three-dimensional island formation (Volmer-Weber) or layer-plus-island formation (Stranski-Krastanov). For example, Growth of Ge on Si is a classical model of the Stranski-Krastanov growth-mode, also known as layer-plus-island growth, where growth starts in a uniform layer-by-layer growth up to ~3 monolayer [1 monolayer (ML) is equivalent to 6.78×10^{14} atoms/cm² on a Si(100) surface.] The lattice mismatch (misfit) between Ge and Si ($a_{\text{Ge}} = 0.566$ nm, $a_{\text{Si}} = 0.543$ nm) causes elastic strain which increases as the Ge film grows on the Si surface. With the increase of strain energy, the competition between chemical potential of the deposited film and strain energy eventually causes the film to continue through three-dimensional (3D) island growth beyond a critical layer thickness around 3 ML. The value of the misfit is the key factor for the relief mechanism. Three dimensional island formation leads to a partial relaxation of strain. Those islands could be dislocation free or coherent and their shapes change during growth.

Surface processes responsible for nucleation and growth depend on several factors such as impinging rate of atoms, substrate conditions, and temperature. There are two important parameters in film growth, namely temperature T and supersaturation m , defined as ratio R is the actual deposition rate, and R_e is the equilibrium value at the temperature T , and thermodynamic driving force $\Delta\mu = kT \ln(R/R_e)$, where k is Boltzman constant [52]. $\Delta\mu$ is zero in equilibrium and it is positive during condensation and negative during sublimation or evaporation. The deposition rate of adatoms R is given by following formula, $R = p / (2\pi m k_B T)^{1/2}$, where m is the atomic mass. Atoms arriving from

repulsion between surface species, and externally supplied energy [53]. The surface diffusion coefficient D is known, as mentioned above, to follow an Arrhenius form with temperature and is proportional to the vibrational energy in the reaction coordinate [53].

II. 3. PARTICULATE FORMATION

PLD is notorious for creating particulates during deposition. They are ranging from sub-micron to several micrometers [57]. Those particulates could be a big problem for integrated-circuit fabrication and other critical applications. Their crystalline structure may vary as well; for example, for laser ablation of amorphous Si by picosecond Nd:YAG laser, both crystalline and amorphous particulates have been observed [66]. Particulates formation has mainly three mechanisms, namely splashing, recoil pressure and fracto-emission, shown in Fig. 3 above. In splashing, a thin layer of the surface superheats above the vaporization temperature and a molten overlayer is blown off and disintegrates into liquid droplets [67-69]. However, in recoil pressure, vaporized materials exert some sort of pressure on the molten layer, formed by laser irradiation, and as a result liquid droplets are ejected [70]. Lastly, fracto-emission is the process in which emission from the microcracks in the target is caused by laser-induced thermal shocks [71]. Particulates formation is affected by a number of parameters such as target, laser parameters, surface quality and laser energy density. For instance, increasing target density can minimize the particulate formation [51], and it was shown that use of ultrafast pulses could eliminate the formation of particulates due to the lower thermal losses compared to the ns pulses, which causes smaller amount of molten material and liquid droplets in the plume [55, 71, 72]. Target surface quality also effects the particulate formation. For example, the probability of fractures emission from rough surfaces is quite

the vapor at a rate R can be absorbed on surface with a residence time τ_{ad} determined by adsorption energy, E_{ad} , and it is defined as $\tau_{ad} = \nu_{ad} \exp(-E_{ad}/k_B T)$, where ν_{ad} specifies a pre-exponential factor as an atomic vibration frequency. During residence time, adatoms diffuse over the surface with diffusion energy E_d and diffusion coefficient D . It is expected that $E_d < E_{ad}$. If desorption processes will take place, E_{ad} will denote as E_d^* a desorption energy and τ_{ad} is the adatom lifetime before desorption. Adatom diffusion is derived from considering a random walk in 2D, and 2D diffusion coefficient is given by $D = D_0 \exp(-E_d/k_B T)$, where $D_0 = [\nu_0 (a_d)^2 / 4]$ is diffusion coefficient constant corresponding to the pre-exponential and a_d is the jump distance of the order of the surface repeat distance. The number of substrate sites visited by an adatom in time τ_{ad} is $D\tau_{ad}/N_0$, where N_0 is the real density of such sites, of the same order as $(a_d)^{-2}$. In the case thin film growth on vicinal surfaces and using simple model for surface diffusion based on Einstein relation, assuming no anisotropy, then $l = (2D\tau_{ad})^{1/2}$ where l is the mean displacement of adatom from the arrival site before capture.

Surface diffusion of particles is one of the most important determinants of film structure because it allows the adsorbing species not only to find each other, and most active sites but also to find epitaxial growth sites [53]. The surface temperature of the substrate determines the diffusion processes. For surface diffusion to occur, a certain amount of energy must be available to the adatoms. This energy can originate from kinetic or potential energy of the adsorbate or can be supplied thermally by substrate heating. The rate of surface diffusion depends on a variety of factors, including the energy of the incoming adsorbate, the strength of the surface-adatom bond, orientation of the surface lattice, densities of atomic steps, surface reconstruction, attraction and

high. Therefore, using rotated polished targets minimizes the particulates formation by exposing fresh target areas to laser all the time. Laser wavelength may play an important role for this problem. It was reported that YBC and BiSrCaCuO films deposited with 1.064 μm were rough, in contrast to the smoother ones deposited with UV wavelengths [54, 57]. However, the wavelength that yields the best film morphology depends on the target material. There have been some investigations to reduce the particulate formation such as using molten targets, electrostatic deflectors to reduce particle content of film, mechanical chopping to filter out low speed particles [73], second pulse to vaporize the in-flight particulates [74], and heated screen to reflect the non-particulate flux onto substrate [75].

CHAPTER III

REFLECTION HIGH-ENERGY ELECTRON DIFFRACTION

III. 1. INTRODUCTION

Reflection high-energy electron diffraction (RHEED) is the analytical tool of choice for monitoring the growth of a range of materials including semiconductors (II-VI, III-V, IV) metals and oxides in high vacuum by various deposition methods since it is very sensitive to surface structure, morphology and surface phase transitions [76, 77].

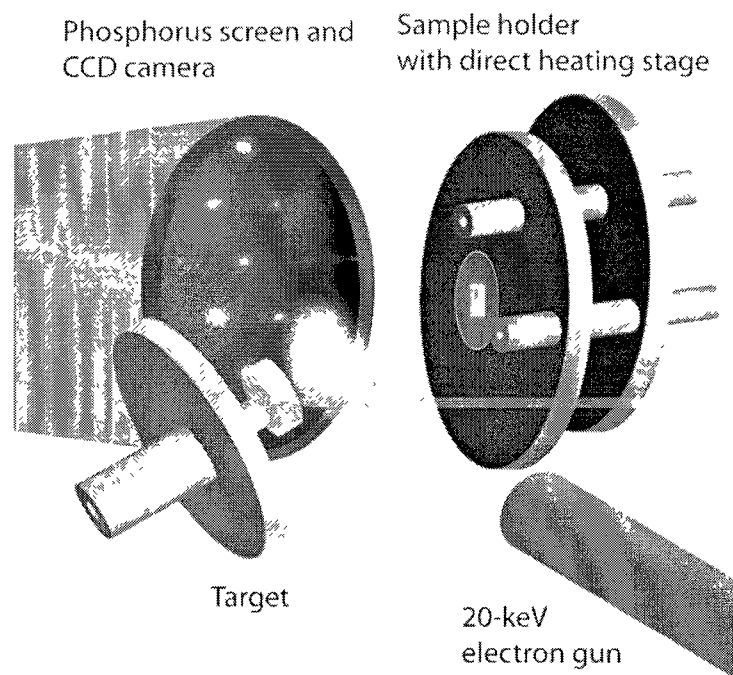


FIG. 4. A typical RHEED mechanism.

The RHEED idea is very simple. An accelerated high-energy (5-100 keV) electron beam hits the surface with a grazing angle $\sim 3^\circ$ and scattered electrons form the diffraction pattern on the phosphorus screen. The feature of glancing angle makes RHEED very

sensitive to surface, rather than bulk material. The main advantages of RHEED as a surface science tool are its simplicity (both setup and operation), low cost, ability of *in vivo* and *in situ* surface monitoring, high sensitivity to surface changes, and compatibility with medium and ultrahigh vacuum environments.

The sample RHEED setup was shown in Fig. 4. Electron gun and phosphorus screen are in the opposite side of the chamber and also they are far from the growth process so that they don't interfere with growth process. This technique can reveal almost perfectly instantaneous changes either in the coverage of the sample surface by adsorbate or in the surface structure of a thin film. RHEED has been used as a basic monitoring tool for many kinds of crystal structures and their growth since 1928 when Shoji Nishikawa and Seishi Kikuchi used it to examine the surface structures [78]. They directed a beam of 50 keV electrons from a gas discharge on a cleavage face of calcite at a grazing incidence of 6° . Diffraction patterns were recorded on photographic plates placed 6.4 cm behind the crystal, normal to the primary beam. Due to its sensitivity to surface changes such as deposition, adsorption and transition from 2D to 3D, RHEED is widely used both in research field and in industry to probe the growth real time [76, 77, 79, 80]. The real time dynamic RHEED patterns allow the monitoring of the growth and give the information about the surface morphology [81-84]. Static RHEED patterns obtained when growth is interrupted yield information about the most likely surface structure, surface lattice reconstruction, the probing the in-plane orientation distribution [85-87]. Chevron angles and oscillation along the chevron tails in RHEED pattern can be used to determine the lateral facet orientation and dot heights [88]. RHEED is also used to monitor the chemical composition of crystals and to observe the growth of insulator

crystals such as organic films and alkali halide films, which are easily damaged by electron beams [89, 90]. The dynamical theory of electron scattering also predicts the temperature measurement based on RHEED intensity analysis [91]. The penetration depth of these fast electrons can be quite large, in the range of several hundred angstroms. However, because of the glancing angle of incident electrons, they only penetrate a few monolayers into the surface. RHEED provide large elastic scattering cross-section for forward-scattered electrons which involves strong interaction such as dynamical scattering and plasmon excitation processes with the periodic potential of the crystal surface [76, 77, 92, 93]. Therefore, dynamical scattering is very strong and this technique cannot be described quantitatively by kinematic approach. However, kinematic approach can still be used for interpreting the physical and understanding and qualitative description of RHEED. In this chapter, an introduction to basic theoretical and experimental Rheed principles along with some calculations will be given.

III. 2. RHEED SETUP AND ALTERNATIVES

III. 2. 1. RHEED SETUP

RHEED has many advantages as a surface science tool. It has a very simple setup, shown in Fig. 4, low cost, easy operation and maintenance, ability for *in situ* and *in vivo* monitoring, high sensitivity to surface changes and amenability to MBE, PLD, CVD and almost any high and ultra-high vacuum chamber system [76, 77, 94-96]. The main parts of any RHEED systems consist of an electron gun, sample, substrate, phosphor screen, charge-coupled (CCD) camera, software to analyze the image, computer, and vacuum deposition chamber. For high pressure, system differential pumping is used and the electron path is kept as low as possible to minimize the scattering losses [95]. The

electron gun produces a well collimated mono-energetic high-energy beam that strikes the surface with a grazing angle $\sim 3^\circ$. In RHEED, the incident electron beam is supposed to be monoenergetic, infinitesimally thin and collimated and the beam energy is very high so that the radius of the Ewald sphere is very large compared to the dimensions of the surface unit mesh. The electron gun should also have small angular divergence at the sample and small spot size on phosphorus screen. The angular divergence should be less than 0.5-1.0 mrad for Si sample [77]. This beam interacts with the surface and undergoes multiple scattering processes, which results the diffraction pattern of the substrate displayed on the phosphor screen. This screen consist of a phosphor covered, indium-thin-oxide (ITO) pyrex disk. ITO is used to prevent charging on the screen. This electron beam is ejected from hair-pin shaped tungsten which is heated by passing the high current. Positive voltage is applied first; filament (cathode) is heated until the stream of electron is produced. Those electrons are accelerated by the positive potential down the column where negative voltage applied to focus the beam. As the electrons move toward the anode, electrons emitted from the filament's side are repelled by the Wehnelt cap toward the optic axis. The electrons at the bottom of the space charge (nearest to the anode) can exit the gun area through the small (<1 mm) hole in the Wehnelt Cap. At the end of the accelerating column, two sets of electrostatic or electromagnetic deflectors are used to control the movement of the e-beam in two dimensions.

The diffracted electrons for both static and time-resolved data acquisition are collected on a phosphor screen to get a visible diffraction pattern and then image is captured with a suitable CCD camera and then transferred to the computer for further

analysis. The RHEED system we use in our lab consists of the following components/parts:

- (1) Electron gun: RDA-002G model electron gun produces, accelerates and collimates nearly mono-energetic electron beams with energies around 30 keV. The continuous wave (CW) electron gun is simply a tungsten filament, which is heated to emit electrons. These electrons are then accelerated to high energies by a series of electrostatic dynodes and are focused by means of electrostatic or electromagnetic lenses. At the end of the accelerating column, two sets of electrostatic or electromagnetic deflectors are used to control the movement of the e-beam in two dimensions
- (2) Substrate: We put the sample Si (100) that causes diffraction of the electron beam.
- (3) Phosphor screen: It is used to transform the diffracted electrons into a visible diffraction pattern. Fast decay phosphor screens may be used for some time resolved studies.
- (4) Charge-coupled device (CCD) camera: KSA K30FW model camera is used to capture the diffraction patterns off the phosphor screen. High frame cameras may be used for time resolved studies.
- (5) Computer: It is used to analyze further for obtained RHEED pattern.

More information about RHEED setup will be given in appendices.

III. 2. 2. RHEED ALTERNATIVES

One can obtain the information about the long-range order of the top surface layers at different azimuthal and incident angles [97]. Computer-controlled automated mechanisms was developed to change the angle of incidence automatically instead

manually, via magnetic deflectors, and to record the data [98]. Elsayed-Ali *et al.* showed that the use of ultrafast laser pulses to drive a RHEED gun makes it possible to collect information about the behavior of atoms at the surface in picosecond periods of time [99]. The excitation probability for surface plasmon becomes larger at smaller incident glancing angles and energy loss spectra of the diffraction spots and energy filtered rocking-curves can be measured with an energy resolution of ~ 3 eV in RHEED apparatus equipped with an energy filter [100]. Energy filter is also used to separate the inelastic diffuse background from elastic contribution of the scattered electrons [101] and improves the shape of RHEED pattern. A cone-shaped convergent beam (CB) is used for acquisition of the rocking curves instead of collimated beam [102]. In the case of CB-RHEED, each of these non-parallel beams will result in its own separate pattern. Hence, the resultant pattern from a flat surface consists of disc-shaped pattern rather than spots in the ordinary RHEED [103].

Time-resolved RHEED is another RHEED modification which consists of an amplified femtosecond laser system, a laser-driven electron gun, a magnetic lens, deflection plates, and an image intensifier with a CCD camera. Combining the RHEED system with the time resolved technique allows studying transient non-equilibrium surface structures, which are very critical to the understanding of laser-initiated phase transitions and dynamics at surfaces [99, 104-106]. The basic idea of this technique is the use of an ultrafast laser pulse to create electron pulse with equal time duration. These photo-generated electrons can be collimated and focused to make them suitable for obtaining a good diffraction pattern from the surface. Photo-activated electron gun instead conventional continuous current-pass filament based gun is used to generate

electron pulse synchronized with a laser pulse. An ultrafast laser beam is split in two parts. The first part uses the optical delay line and serves as a pump pulse which is directed on to the sample in order to excite the surface. The second part is frequency tripled/quadrupled laser pulses by using nonlinear optical crystals. These pulses are directed onto the backside of the photocathode of a pulsed electron gun. The short electron pulses with a temporal width comparable to that of the laser are created by photoemission. The electrons are focused onto the sample by using an electrostatic lens under a grazing angle of incidence and probes the first few atomic layers. The scattered electrons are detected in a multi channel plate-detector (MCP). The resulting diffraction patterns are recorded with a cooled CCD-camera and the images are stored for further analysis [107]. The electron pulses probe the surface at fixed times. The moment of excitation can be varied by changing the path length for the pumping laser light in the delay line. This enables the setting of a delay between pump and probe pulse so that the pump pulse arrives before the probe pulse or the excitation occurs after the electron pulses probed the surface. Diffraction images recorded at different fixed delays reveal a direct measure of the dynamic changes of the surface structure. Time resolved RHEED can be used as a surface-lattice temperature by means of the transient surface Debye-Waller effect by synchronizing the electron pulse with the heating laser pulse [108, 109].

III. 3. RHEED THEORETICAL MODEL

RHEED data can be interpreted by either kinematical or dynamical scattering analysis [76, 77, 94]. The kinematic theory of RHEED which assumes that the electrons are scattered elastically from the surface and that only the incident beam produces diffracted beams so that locations of diffraction maxima will be predicted. However,

kinematic theory doesn't provide information for the relative intensities of diffraction maxima. To obtain the information about their relative intensities, one should use the dynamical RHEED theory which allows for multiple scattering events at the surface in addition to inelastic scattering effects and is a much more complicated approach.

III. 3. 1. Kinematic Scattering Analysis

The many characteristics of the RHEED pattern can be qualitatively understood by using simple kinematic scattering theory, which is actually a single scattering theory. This, in most cases, is sufficient to describe most features of the experimental RHEED pattern and that the fit is even sensitive enough to perform structure refinement. This theory is widely used for experimental calculations due to its simplicity. In the kinematic approximation, a diffracted beam is generated when a reciprocal lattice point lies on the surface of Ewald sphere which is a sphere that has its origin as the origin of the k_0 and radius of its magnitude, shown in Fig. 5. Ewald's spheres show the allowed diffraction conditions for kinematically scattered electrons in a given RHEED setup. The diffraction pattern at the screen relates to the Ewald's sphere geometry, so RHEED users can directly calculate the reciprocal lattice of the sample with a RHEED pattern, the energy of the incident electrons and the distance from the detector to the sample. The Ewald's sphere is centered on the sample surface with a radius equal to the reciprocal of the wavelength of the incident electrons, shown in Fig. 5. The following equation gives this relationship.

$$k_0 = \frac{2\pi}{\lambda} \quad (3)$$

where λ is the wavelength. Diffraction conditions are satisfied where the rods of reciprocal lattice intersect the Ewald's sphere. Therefore, the magnitude of a vector from

the origin of the Ewald's sphere to the intersection of any reciprocal lattice rods is equal in magnitude to that of the incident beam.

$$k_0 = k_i \quad (4)$$

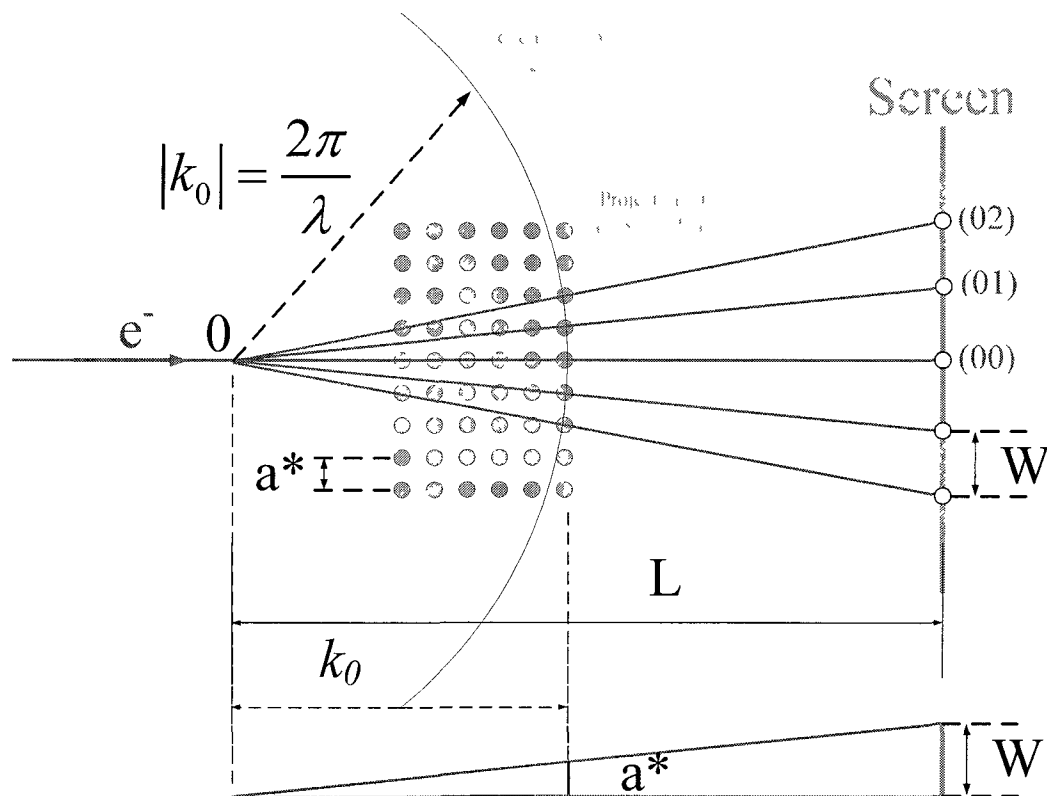


FIG. 5. Kinematic theory of RHEED.

This is the special case of elastic scattering where k_0 is the incident electron wave vector and k_i is the electron wave vector at any intersection of reciprocal lattice with Ewald's sphere.

An arbitrary vector \vec{G} defines the reciprocal lattice vector between the ends of any two k vectors. Vector \vec{G} is useful for finding distance between arbitrary planes in the crystal. Vector \vec{G} is calculated using Equation 5.

$$\vec{G} = \vec{k}_i - \vec{k}_0 \quad (5)$$

Many of the reciprocal lattice rods meet the diffraction condition; however the RHEED system is designed such that only the low orders of diffraction are incident on the detector. The RHEED pattern at the detector is a projection only of the k vectors that are within the angular range that contains the detector. The size and position of the detector determine which of the diffracted electrons are within the angular range that reaches the detector, so the geometry of the RHEED pattern can be related back to the geometry of the reciprocal lattice of the sample surface through use of trigonometric relations and the distance from the sample to detector. The magnitude of the k wavevector for the high-energy electrons is given by relativistic equation:

$$\vec{k}_0 = \frac{1}{\hbar} \sqrt{2m_0 E + \frac{E^2}{c^2}} \quad (6)$$

where m_0 is the electron rest mass, q is its charge and V is the accelerating potential. Expression (6) is sometimes written as

$$\lambda = \frac{\hbar}{\sqrt{2m_0 qV + \{qV/c\}^2}} \cong \frac{12.3}{\sqrt{V(1 + 1.195 \times 10^{-6} V)}} \quad (7)$$

where the wavelength λ is measured in Å and V is in volts. The amount of relativistic correction, in our case ~3%, is usually often sufficient to use the nonrelativistic approximation for qualitative analysis. In RHEED, radius of Ewald sphere is much larger than the reciprocal lattice unit of the sample. The incident wavevector is 785 nm^{-1} as a

result of using 20 keV electron gun. This is about 71 times larger than the reciprocal lattice unit of silicon. One can easily see that this will result in most likely planar cut through the first few Brillouin zones. Along with the small scattering angles, this large Ewald sphere enable us to determine kinematic interpretation of RHEED patterns, since for many purposes distortions can be neglected and the usual small-angle approximations for trigonometric functions are valid [76]. Lattice spacing can be successfully calculated by using simple kinematical model for RHEED. The spots on the RHEED screen are results of the intersection of Ewald sphere with the reciprocal lattice rods at a given condition. Image on the screen is actually the projection of that spots. One can apply the simple trigonometric relationship of two triangles in this figure to get the following relation:

$$\frac{W}{L} \cong \frac{a^*}{|k_0|} \quad (8)$$

where W is the streak spacing, L is the sample-to-screen distance. It should be noticed that changing the azimuthal angle would yield completely different diffraction pattern, since Ewald sphere would intersect the different reciprocal lattice rods. The picture we observe on the fluorescent screen as result of electron interacting with the semiconductor surface is a trace of events taking place in the reciprocal lattice. The streak spacing corresponds to the lateral rod spacing for a particular azimuthally orientation of the sample with respect to the incident beam. The relation between a^* of the reciprocal lattice rods and spacing W of the RHEED streaks observed on the screen is illustrated in the following figure. Miller indices are attributed to the rods and features (spots or streaks) in the RHEED pattern. We can derive the following equation from Fig. 5 by using principle similar triangle.

$$W/L \sim a^*/2\pi/\lambda \quad (9)$$

Hence,

$$W = a^* \lambda L / 2 \pi \quad (10)$$

Frequently, the only diffraction spots or streaks seen on the screen are due to one row of rods and they make up the zeroth order Laue ring.

The positions of RHEED patterns can be generally obtained by using kinematic theory which assumes that the electrons are scattered elastically from the sample surface and only incident beam produces the diffracted beams. However, to get the intensity of these beams and quantitative analysis requires dynamical theory which is very strong due to interactions between electrons and sample. In this theory, multiple scattering at the surface and as well as inelastic scattering effect is also considered.

III. 3. 2. DYNAMICAL SCATTERING ANALYSIS

The multiple scattering effects are always present in electron diffraction since electrons are charged particles and their interactions with solids are rather strong compared to X-rays or neutrons. Therefore, electron diffraction must be described by dynamical scattering. Also, dynamical theory takes account of extra adsorption due to multiple scattering, shifts in peak position due to non-zero phase of transmission coefficients, and extra structure arising from flux sharing of different beams. The first dynamical theory of dynamical theory of electron diffraction was developed by Bethe [110] in order to give quantitative account of experimental observation by Davisson and Germer [111]. In their experiment, electron beam was fired on nickel crystal and the intensity of scattering electron beam was measured as a function of direction. The existing dynamical RHEED theories may be classified into four distinct types, namely,

(1) multislice theory, (2) semi-reciprocal theory, (3) Green's function's theory and (4) Bloch wave theory [112]. The dynamical theory has been introduced to overcome the single scattering problems.

The dynamical theory is based on Bloch wave solution of the Schrodinger equation for a system with a fast electron placed in a periodic potential. For a plane wave, if scattering potential $V(r)$ is weak and it is distributed in small region [94], then the wave observed at a large distance from the scattering zone is

$$\psi \approx \exp(2\pi i K_o.r) + f(\varphi) \frac{\exp(2\pi i r)}{r} \quad (11)$$

Where $f(\varphi)$ indicates the amplitude of the scattered wave as a function of the scattering semi-angle. The amplitude with which an incident plane wave $\exp(2\pi i K_o.r)$ is scattered to an exit plane wave $\exp(2\pi i K.r)$ is calculated based on the first Born approximation,

$$f(u) = -\frac{m_0}{2\pi\hbar^2} \int_{-\infty}^{\infty} dr \exp(-2\pi i u.r) V(r) \quad (12)$$

Where $hu=h(K-K_0)$ is the momentum transfer of the incident electron. The Born approximation assumes single scattering; that is, the electron is scattered only once. This assumption is the basis of the kinematical scattering theory. Equation above explicitly implies that the scattering amplitude under the single-scattering approximation is proportional to the Fourier transform of the scattering object potential [94]. If the atomic potential is spherical symmetric, i.e., $V(r)=V(r)$. Then above equation becomes

$$f(\varphi) = -\frac{2m_0}{\hbar^2} \int_0^{\infty} dr \frac{\sin(2\pi ur)}{2\pi ur} V(r)r^2 \quad (13)$$

Where 2φ is the scattering angle, and $u=K-K_0$ with $u=2K_0\sin\varphi$. The elastic scattering obeys the law of conservation of energy, or equivalent $|K|^2 = |K_0|^2$.

From the above equation, the scattering power of the atom is determined by the Fourier transform of its electrostatic potential, thus the electron scattering factor of the atom is defined as

$$f^e(u) = \int_{-\infty}^{\infty} dr \exp(-4\pi i s \cdot r) V(r) \quad (14)$$

Where the scattering vector is defined as $s=u/2$, with $|s| = \sin\varphi / \lambda$ and u a reciprocal space vector. The electron scattering factor is usually given as a function of s . The electron scattering factor define in Eq. 14 is a quantity that characterizes the scattering power of an atom and its independent of accelerating voltage.

We then applied kinematic theory to the scattering amplitude from a crystal surface. For simplification, the contribution made by the top atomic layer of the surface is considered. Under the rigid body approximation, the potential distributed in the surface can be written generally as a superposition of the potential distribution from each atom site r_i ,

$$U_s(r) = \sum_i U_i(r-r_i) \quad (15)$$

where i refers to the i th atom site on the surface. According to the first Born approximation, the scattering amplitude is a Fourier transform of U_s

$$U_s(u) = FT[U_s(r)] = \sum_i f_i^e(u) \exp(-2\pi i u \cdot r_i) \quad (16)$$

The kinematically diffracted intensity is,

$$I_s(u) = |U_s(u)|^2 = \sum_i \sum_j f_i^e(u) \exp(-2\pi i u \cdot (r - r_j)) \quad (17)$$

This is the general equation for RHEED. The diffracted intensity $I_s(u)$ can be predicted from different structure surfaces such as disordered surfaces, surfaces with islands, and stepped surfaces [94]. As can be seen clearly, it is really hard to use dynamical theory frequently for the analysis. The additional information about the other dynamical scattering theories can be obtained elsewhere [76, 77, 94, 113, 114].

RHEED in-plane rocking curves are used to determine the crystal structures of ultrathin films and atomic arrangement on the surface may even be obtained by fitting experimental results to the calculations [115]. They are obtained by changing the glancing angle to get the refracted beam dependence on the incidence angle of the primary beam. The resulting intensity distributions are characterized by a FWHM, which is related to in-plane orientation distribution. Rocking curve only requires the intensity measurements and intra-sample intensity comparisons which are not sensitive to experimental variations [86]. The rocking curves and the azimuthal plots, which are obtained by recording the intensities of a certain diffracted beam as a function of the azimuthal angle, are used to determine the atomic arrangement at the surface and surface symmetry.

III. 4. OBTAINING RHEED PATTERNS

For pure reflection RHEED of a given surface of known orientation, 2D indexing is used. Recalling that RHEED is an image of the surface lattice in the reciprocal space, a pre-calculation of the reciprocal lattice mesh of that surface is needed. These calculations are necessary to determine the direction of the incident electron beam relative to the surface structure. In the case of an unknown crystal surface, calculations are performed for different crystal surfaces till a good match between the experimental and the

calculated structure is found. Below, the reciprocal lattices of Si (100) and Ge (100) surfaces are calculated.

III. 4. 1. CALCULATION OF RECIPROCAL LATTICE OF Si(100)

The crystal structure of silicon is diamond, shown in Fig. 6; we can see that in the following figure by using crystalmaker software free version.

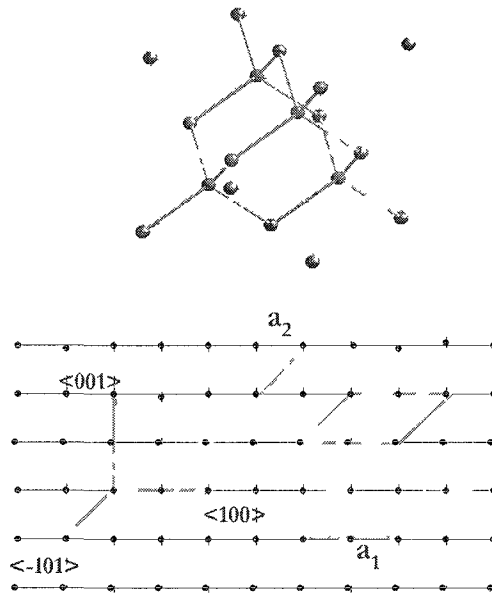


FIG. 6. (a) Diamond structure of silicon. (b) Real Net of the Si (100).

The lattice parameter is $a = 5.431 \text{ \AA}$. So, we can calculate the area of unit mesh by using the following equation.

The reciprocal lattice basis vectors are defined as

$$\bar{a}_1^* = 2\pi \frac{\bar{a}_2 \times \hat{n}}{A} \quad (18)$$

$$\bar{a}_2^* = 2\pi \frac{\hat{n} \times \bar{a}_1}{A} \quad (19)$$

where the area A is

$$A = \bar{a}_1 \cdot (\bar{a}_2 \times \hat{n}) \quad (20)$$

Silicon has a diamond structure, which is shown in Fig. 6(a). The lattice parameter is $a = 5.431 \text{ \AA}$. So, using Fig. 6(b), the real lattice vectors of Si(100) mesh are

$$\underline{a}_1 = 5.431 \langle 010 \rangle \text{ \AA} \quad (21)$$

$$\underline{a}_2 = \frac{5.431}{\sqrt{2}} \frac{1}{\sqrt{2}} \langle 011 \rangle = 2.716 \langle 011 \rangle \text{ \AA}, \quad (22)$$

and the unit vector normal to the surface is $\underline{n} = \langle 100 \rangle$.

The inter-planer spacing between the planes is quarter of the lattice parameters, which is $a/4$ in this case, i.e., 1.358 \AA .

The area of the unit mesh is

$$A = \bar{a}_1 \cdot (\bar{a}_2 \times \hat{n}) = \frac{(5.431)^2}{2} \begin{vmatrix} 0 & 1 & 0 \\ 0 & 1 & 1 \\ 1 & 0 & 0 \end{vmatrix} = 14.748 \text{ \AA}^2 \quad (23)$$

Therefore if we substitute these values in Eqs. 18 and 19, we will find reciprocal lattice parameters,

$$\bar{a}_1^* = 2\pi \frac{\bar{a}_2 \times \hat{n}}{A} = \frac{2\pi}{14.748} [2.7155 \langle 011 \rangle \times \langle 100 \rangle] = 1.157 \langle 01\bar{1} \rangle \text{ \AA}^{-1} \quad (24)$$

$$\Rightarrow |\bar{a}_1^*| = 1.636 \text{ \AA}^{-1}$$

$$\bar{a}_2^* = 2\pi \frac{\hat{n} \times \bar{a}_1}{A} = \frac{2\pi}{14.748} [5.431 \langle 100 \rangle \times \langle 010 \rangle] = 2.314 \text{ \AA}^{-1} \quad (25)$$

The reciprocal lattice would have the shape shown in Fig. 6(b).

III. 4. 2. CALCULATION OF RECIPROCAL LATTICE OF GE(100)

The crystal structure of Germanium is also diamond with lattice parameters of $a = 5.646 \text{ \AA}$. So, by using same figure, one can easily calculate the real lattice vectors of Ge (100) mesh are

$$\begin{aligned} \underline{a}_1 &= 5.646 \langle 010 \rangle \text{ \AA}, \\ \underline{a}_2 &= \frac{5.646}{\sqrt{2}} \frac{1}{\sqrt{2}} \langle 011 \rangle = 2.823 \langle 011 \rangle \text{ \AA}, \end{aligned} \quad (26)$$

and the unit vector normal to the surface is $\underline{n} = \langle 100 \rangle$.

The inter-planer spacing between the $\{100\}$ planes is $a/4$, i.e., 1.412 \AA .

The area of the unit mesh is

$$A = \underline{a}_1 \cdot (\underline{a}_2 \times \hat{n}) = \frac{(5.646)^2}{2} \begin{vmatrix} 0 & 1 & 0 \\ 0 & 1 & 1 \\ 1 & 0 & 0 \end{vmatrix} = 15.939 \text{ \AA}^2. \quad (27)$$

Hence, by substituting the values for the area and the lattice parameters in Eqs. (18) and (19), the reciprocal lattice parameters are

$$\underline{a}_1^* = 2\pi \frac{\underline{a}_2 \times \hat{n}}{A} = \frac{2\pi}{15.939} [2.823 \langle 011 \rangle \times \langle 100 \rangle] = 1.113 \langle 01\bar{1} \rangle \text{ \AA}^{-1} \quad (28)$$

$$\Rightarrow |\underline{a}_1^*| = 1.574 \text{ \AA}^{-1}$$

$$\underline{a}_2^* = 2\pi \frac{\hat{n} \times \underline{a}_1}{A} = \frac{2\pi}{15.939} [5.646 \langle 100 \rangle \times \langle 010 \rangle] = 2.226 \langle 001 \rangle \text{ \AA}^{-1} \quad (29)$$

III. 5. INDEXING TRANSMISSION RHEED PATTERNS

Transmission RHEED patterns are indexed using three indices, similar to diffraction from bulk materials and selected area electron diffraction (SAED) [116].

Different alternatives can be used to index transmission patterns. The following procedure is used to index transmission spots from Ge QD.

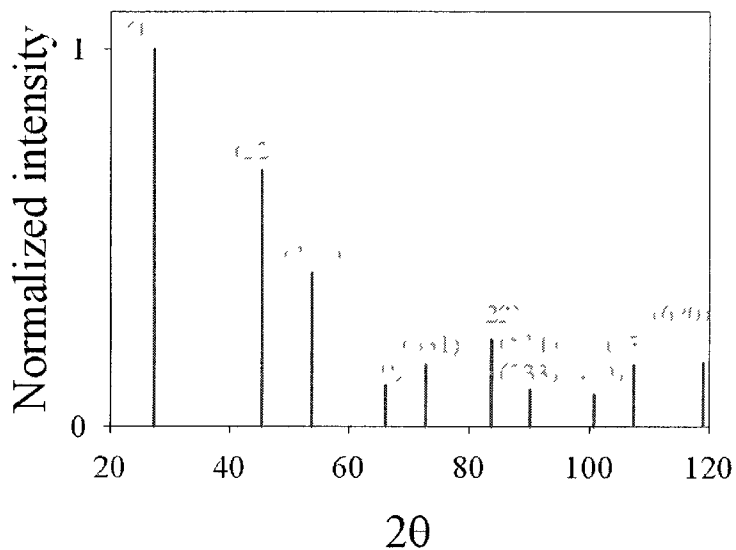


FIG. 7. The expected XRD pattern of Ge crystal.

1. Use "Diamond" software to generate the expected XRD pattern of Ge crystal, Fig.

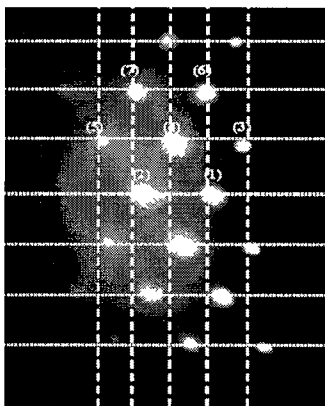


FIG. 8. Transmission RHEED pattern of Ge QD.

2. You may also use “CaRIne” software to generate similar powder diffraction patterns, however, some values may differ slightly.

TABLE 1. Data extracted from Fig. 7. We calculated interplanar distances, d , of the associated planes.

Theoretical calculations					
(hkl)	2θ	λ (Å)	d (Å)	$d/2$ (Å)	$2d$ (Å)
111	27.28	1.541	3.26894	1.63447	6.53788
220	45.3	1.541	2.001736	1.000868	4.003472
311	59.8	1.541	1.707333	0.853666	714666
400	65.99	1.541	1.415525	0.707763	2.83105
331	72.8	1.541	1.298976	0.649488	2.597952
422	89.6	1.541	1.905807	0.952903	3.811613
333/511	90.05	1.541	2.50377	1.251885	5.00754
440	100.73	1.541	2.949317	1.474658	5.898633
531	107.3	1.541	74106	1.72053	6.882119
620	118.86	1.541	3.799634	1.899817	7.599267

3. From the graph, extract the angles associated with the diffraction planes.
4. Take one point as your (000) point. Here we take one point on the shadow edge.

TABLE 2. Interplanar distances. We calculated from the measurement of spot distances in Fig.8.

Experimental measurements						
Spot	λ (Å)	R (cm)	α_{ij}	d (Å)	$d/2$ (Å)	$2d$ (Å)
1	0.111	1.22619	0	3.077825	1.538913	6.15565
2	0.111	2.440476	0	1.54642	0.77321	3.092839
3	0.111	1.064345	52.8	845842	1.772921	7.091684
4	0.111	2.035714	25.2	1.853895	0.926947	3.707789
5	0.111	3.133333	15.2	1.204468	0.602234	2.408936
6	0.111	2.088333	59	1.807183	0.903591	914366
7	0.111	2.988095	34.8	1.263012	0.631506	2.526024

5. Use these data to calculate the interplanar distances of the above planes, Table 1.
6. Obtain a RHEED diffraction pattern of Ge QD at a certain azimuth, Fig. 8.
7. Measure the distances of the transmission spots to the (000) point in “cm” and the angles they make with the line perpendicular to the surface and passing through the (000), Table 2.
8. Use $d_{hkl} = \frac{\lambda L}{Z}$ and the calculated electron wavelength to convert the above distances into d -values, Table 2.
9. Compare the measured values to the calculated ones to assign Miller indices to each spot. Tabulate all the possible indices, since it is normal to find more than one set for each spot.
10. You have to consider an error margin, Δd , in the measured values of d -value due to uncertainties in the spacing measurement and in the camera constant calibration.
11. For each possible hkl candidate, calculate the angles between these spots, α_{ij} , using the dot product rule, $\alpha_{ij} = \cos^{-1} \frac{\bar{a}_i \cdot \bar{a}_j}{|a_i| |a_j|}$.
12. Use the elimination process by comparing the measured and calculated angles, in order to assign the correct indices.
13. Determine the zone axis $[uvw]$. This is done by considering any two known $[hkl]$ vectors within the diffracted zone such and finding out the components $u = k_1 l_2 - k_2 l_1$, $v = l_1 h_2 - l_2 h_1$, and $w = h_1 k_2 - h_2 k_1$.

14. Follow the same process to find the correct indexing for each spot, taking advantage of the already indexed ones and by making use of the calculated zone axis, since the zone equation, $hu + kv + lw = 0$, is always satisfied.

TABLE 3. Comparison of the angles. The calculated and measured values of angles between the index planes.

Angles comparisons			
Spot	Index	$\alpha_{\text{calculated}}$ (degrees)	α_{measured} (degrees)
1	(200)	0	0
2	(400)	0	0
3	(111)	54.7	52.8
4	(311)	25.2	25.2
5	(511)	15.7	15.2
6	(222)	54.7	59
7	(422)	35.3	34.8

It is clear that only the first pair has an angle value that agrees with the measured one, i.e., spot (1) is (200) and spot (3) is (111). This implies that the zone axis is $[0\bar{1}1]$.

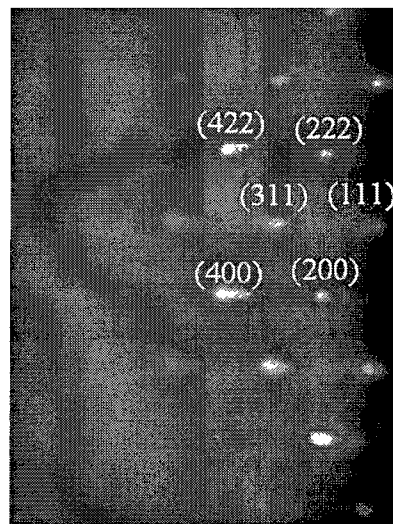


FIG. 9. Indexed transmission pattern of Ge QD.

15. Follow the above procedure till all spot are indexed.

By comparing Tables 1 and 2 and considering Fig. 8, the expected indices for spot (1) are (200) and (440), those for spot (2) are (400) and (880), for spot (3) are (111) and (531), and for spot (4) are (311) and (10,6,2). Considering, first, spots (1) and (3), the angles between (200) and (111), (200) and (531), (440) and (111), (440) and (531) are 54.7° , 32.3° , 65.9° , and 80° , respectively.

Using this value and making use of the zone equation, spots (2) and (4) should be (400) and (311), respectively. Also, using this information it is easy to index the rest of the spots. Comparison the values of the measured and the calculated angles should be used to confirm the indices, Table 3. The final indexing is shown in Fig. 9.

CHAPTER IV

THE SCANNING TUNNELING MICROSCOPE

IV. 1. OVERVIEW

The nanoscale world provides incredible opportunities where Newtonian mechanics is no longer valid and all formulas must be rewritten. In such a small scale, where classical Newtonian mechanics fails, quantum mechanics dominates the mechanism on the single molecule. In order to study the quantum world, a probe that utilizes the quantum mechanics is critically important. One of the mechanisms is the electron tunneling through a potential barrier. The scanning tunneling microscope (STM), a fundamental tool indispensable to the development of nanotechnology, was invented by Binnig and Rohrer [117]. It has many practical applications in both industrial and also fundamental research to obtain atomic-scale images of metal surfaces and to fabricate nanodevices and nanoelectronics. It provides a three-dimensional profile of the surface which is very useful for characterizing surface roughness, observing surface defects, and determining the size and conformation of molecules and aggregates on the surface. The STM can be used not only in ultra high vacuum but also in air, water, and various other liquid or gas ambient, and at temperatures ranging from near zero Kelvin to a few hundred degrees Celsius [118]. STM is based on the concept well-known quantum tunneling. When an atomically sharp tip is brought close to the electrically conducting surface but not actually physical contact, electrons can tunnel through the vacuum between tip and surface when voltage difference is applied between those two elements, shown in Fig. 10. The resulting tunneling current, generally on the order of 10^{-10} Amper, depends on the tip position, applied voltage and the local density of states (LDOS) of the

sample. Atomically sharp tip move across the surface to obtain the useful data, and this process requires extremely clean environment, stable sample surface, state-of-art electronics and excellent vibrational isolation. Detailed procedure will be given in the appendices.

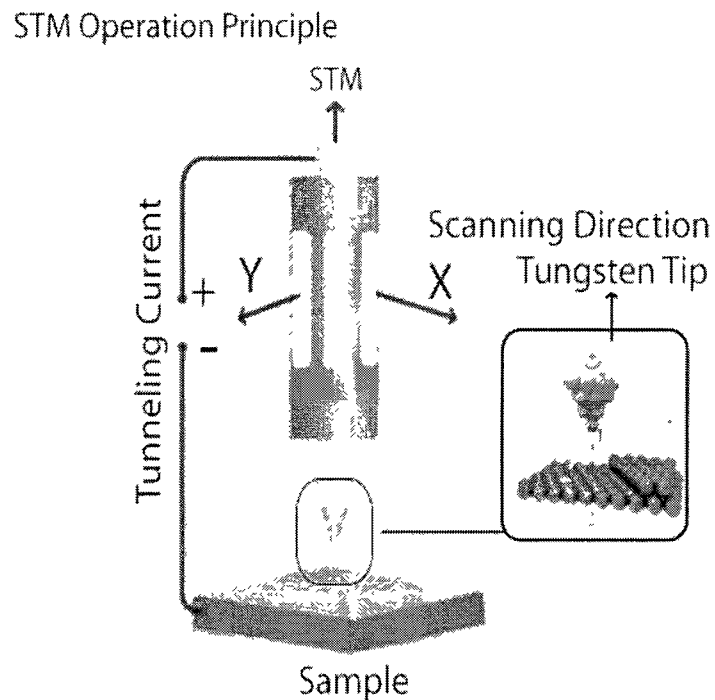


FIG. 10. Basic principles of STM.

The forefather of the STM was the topographiner, a device that utilizes field emission rather than tunneling as the surface technique with a lower resolution compared to STM [119]. In 1983, Binnig and Rohrer achieved the first atomic resolution of two unit cell of the Si(111)-7x7 reconstructed surface [120]. It was this study bringing them Nobel Prize in 1986 [121]. Following the invention of STM, the instrument has been extensively used and has impacted the surface science greatly to understand the surface

structures, defects, compositional elements as well as the surface properties of many inorganic conducting materials [122]. Other methods, such as RHEED and LEED, can give information about the surface structure for a large area; STM will provide information of the individual defects as well as critically important surface reactions. It can also be applied to investigate the crystal growth to get a better insight of nucleation mechanisms of different substrates. STM is a very versatile tool that it can be combined with other surface science techniques [33, 123-127]. It is also has been utilizing on the biological molecules on conducting substrate to get the information regarding atomic resolution images of the single molecules [122]. STM makes it possible to get the high resolution images of DNA molecules and to determine their morphology on different substrates [128-131].

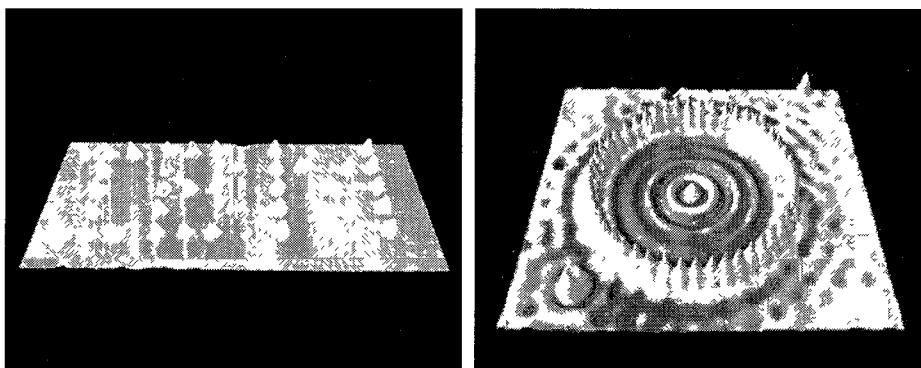


FIG. 11. Manipulating the surface by STM
(www.almaden.ibm.com/vis/stm/atomo.html).

Other microscopy techniques have been developed based upon scanning tunneling microscopy such as photon scanning tunneling microscope (PSTM), revealing variations in the evanescent field due to topographic changes, the index of refraction inhomogeneities, or modal variations within the waveguide [132]. Another variant of the

STM is the scanning tunneling potentiometer (STP), measuring the electron potential across the surface [132]. Spin polarized scanning tunneling microscope (SP-STM) is another version of the STM that can provide detailed information of magnetic phenomena on the single-atom scale additional to the atomic topology. In this case, ferromagnetic tip tunnels the spin polarized electrons into magnetic sample [133].

Manipulating the STM tips changing the topography of the sample is an innovative experimental technique of nanoscience. Examples of manipulating the surface with tip are shown in Fig. 11.

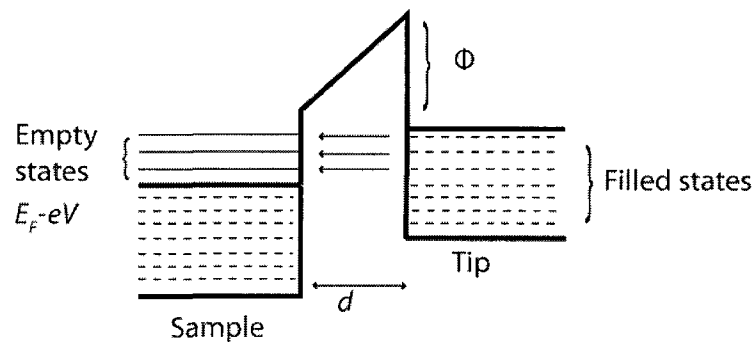


FIG. 12. Filled and empty states in tip and sample.

By using this technique as analytical tool, it is easy to engineer nano-scale structures [134].

IV. 2. THEORY

Basics of the scanning tunneling microscopy is the electron tunneling through the potential barrier, vacuum. In classical mechanics, an object cannot pass through impenetrable barrier. Electron has a very small mass and shows wavelike properties, it obeys the quantum mechanics rather than classical. Electrons in semiconductors and

metals are described in Fig. 12. The energy level of this electron in the presence of one-dimensional potential barrier is given by the Schrodinger's equation,

$$-\frac{\hbar^2}{2m} \frac{\partial^2 \psi_n(z)}{\partial z^2} + U(z)\psi_n(z) = E\psi_n(z) \quad (31)$$

where \hbar is the Planck's constant, z is the position, and m is the mass of an electron.

Solution of the Schrodinger's equation inside the potential barrier has the form:

$$\Psi_n(z) = \Psi_n(0) \exp(\pm ikz) \quad (32)$$

where

$$k = \frac{\sqrt{2m(E - U(z))}}{\hbar} \quad (33)$$

where E is the energy of electron, U is the potential barrier and k defines decay of the wave inside the barrier. One can easily calculate the probability that an electron will cross the barrier is given by the following formula,

$$I \propto \exp(-2kz) \quad (34)$$

Here, the tunnel current depends on the overlap of the tip and sample wavefunction and as it can be seen it exponentially depends on the sample-tip separation. It should be noticed that only electrons with energies between the Fermi levels of two materials can tunnel since there is a constraint that electron must exist in a filled state at the energy in the negative material and unfilled state must exist at the energy in the positive material [135]. When the sharp tip is brought close to the surface, the wavefunction of the tip and sample overlaps and gives rise to the following current

$$I = C \rho_t \rho_s \exp(zk^{1/2}) \quad (35)$$

where z is the junction width, ρ is the electronic structure and C is a constant [135]. As stated before, the tunneling current is exponentially dependent on the sample-tip

separation and it increases by one factor per Angstrom and a decrease of 2 Angstrom will cause the current to increase by two orders of magnitude as the tip moves closer to the surface. Sensitivity, as can be seen, is very high in STM measurement. In typical systems a tip-sample separation of 0.5 nm will produce currents of ~ 1 nA for biases of 1 V. STM imaging could be achieved by either by constant height mode (CHM) or constant current mode (CCM). In constant height mode, the constant height and constant applied voltage are maintained at the same time as the tip moves across the sample whereas in the constant current mode, the tip is vertically adjusted by using a feedback loop, tunneling current remains constant while a constant bias is applied to the between tip and sample as the tip is scanned over the sample. If the tip is scanned at a constant height above the surface, there will be variation in the current since topographic structure changes the junction width. The current will be the highest when the tip is just above the surface atoms while it will be the lowest when it is above the hollow sites on the surface. The resulting plot of the tunneling current as a function of lateral position will therefore show the surface structure and resulting image will be the current image and it is related to the charge density. In constant current mode, as the tip moves over the surface, the vertical position of the tip varies to maintain the distance between tip and sample constant as the tip encounters the surface properties. For example, tip is retracted as it passes over surface properties and will move slightly towards to the surface as it passes the holes. The motion of the tip in all three directions (x, y, and z) is controlled by the piezoelectric elements. Although both methods have their advantages, the normal way of imaging is the constant current mode since it allows investigating also the rough samples with high quality as well as the flat samples. The constant height mode is only appropriate for ideal

flat surfaces. Otherwise, tip crash will be inevitable for the rough surfaces. Speed of constant current mode is restricted by the usage of feedback mechanism. The average speed for this mode is about one image per second. Comparing the scanning frequency in constant current mode, this mode has a big advantage that it could be used for very high scanning frequency (up to 10 kHz) since the scanner doesn't have to move up and down and also it can be used to collect STM images in real time, thus allowing the one to observe dynamical atomistic processes such as surface diffusion [136].

There is also another mode of operation for STM, called barrier height imaging, in the case of inhomogeneous compound. Tunneling barrier is directly related to the work function of the surface and tip, quite sensitive to the chemical properties of the surface [137-139]. The work function will also be inhomogeneous which will cause changing the local barrier height. The image in this mode can be obtained by measuring the modulated current dI/dt in a constant current mode [140]. It provides information about the spatial distribution of the microscopic work function of the surface in an atomic scale and a map of barrier height between tip and STM sample [141, 142].

IV. 3. INSTRUMENTATION

STM has a lot of highly sophisticated components including coarse-approach mechanism, scanning tip, sample holder, piezoelectrics, and x, y, and z scanner, vibration isolation system, amplifiers and other electronics with suitable software to analyze the data. In normal STM operation, the tunneling current (0.01mA-50mA) is converted into a voltage by a current amplifier. To get a linear response with respect to the tunneling gap (the current is exponentially dependent on the tip-sample distance) the signal is processed by a logarithmic amplifier. The output of the logarithmic amplifier is compared with a

predetermined voltage which is used as a reference current. The error signal is passed to feedback electronics, which applies a voltage to the z piezo to keep the difference between the current set point and the tunneling current small. Care has to be taken to keep the noise signal ratio on a low level. Also the response time of the feedback has to be minimized without losing accuracy.

The vibration isolation is one of the most important problems to suppress the external mechanical perturbation down to a subatomic scale. Considering the average sample corrugation around 0.1 Angstrom, the tip-sample distance should be kept constant within 0.01 Angstrom to achieve atomic resolution by STM.

Vibration isolation is therefore extremely crucial to reduce the inner vibrations and isolate the system from external source of vibrations such as vibration of building, running people, vacuum pumps, and sound. It has to be also noted that resonant frequency must be much lower than that of external sources. In our UHV system, vibration isolation is achieved by Eddy current damping system in which circulating eddies of the current create induced magnetic field that is opposed the change of the original magnetic field.

The positioning device is required to control the motion on a coarse and fine scale in three dimensions. The fine scale is also used as scanner which is made out of a piezocrystal and piezoceramic material. The coarse position is achieved by the help of springs, microscrews, and other mechanics. In some STM designs, it is also possible to move the sample but, in our case, our sample is fixed. Instead, we are just able to move the tip in all three directions via coarse motion control box, its step motor, and fine motion piezo controllers.

There are many kinds of sample holder depending on the applications such as direct current heating, radiative heating sample holder, and other types. All of them have the molybdenum base.

The tips, their shape, and their preparation are perhaps the most critical components for STM. Depending on the applications, there are many types of STM tips. Ideally STM tips should terminate in a single atom at its apex. The macroscopic shape of the tip is important for larger scale topography however it is not important for smaller scale since the closest atom will give the major contribution to the tunneling current. For the larger scale, the smaller radius of curvature is required since it needs to penetrate into deep and narrow regions on the sample surfaces. It is important to have a very sharp and hard material tip since there is a good possibility of crashing the tip with surface. The tungsten and Pt/Ir tip has been used most widely used in STM scanning. Tungsten tip is actually useful in UHV application but not suitable for application in air since it oxidizes in air very easily resulting in reduced conductance. Pt/Ir tips, however, is very useful in air due to low oxidization in air and also since they are robust and hard, also suitable for rough surfaces. There are also other types of tips resistant against accidental crash such as titanium carbide and gold [143]. The other tip materials are required for some specific application. For example, magnetic and ferromagnetic tips have been developed for spin polarized STM to image local magnetic characteristic of the material surfaces. Some of those tips are CoCr tips by cleaving a Si wafer covered with a CoCr film, ferromagnetic CrO₂ tip on Cr(100) single crystal surface to observe alternating step heights, a single crystal Ni tips [144], bulk Cr tips, Fe [145], Co [146], Au/Co-coated W tip [147] and some of antiferromagnetic tips , MnNi [148], MnPt, Mn-coated W tip [149]. Carbon

nanotubes are also good candidate due to their nanometric diameter, chemical inertness high-aspect ratio, stability, and strength. Their high electrical conductivity and mechanical properties make them unique for many STM applications [150-152]. The most widely used method to obtain tips is the electrochemical etching by using different chemical solution such as KOH, NaOH, and KCN. But there are also other methods available such as mechanical cutting and grinding from various materials such as W, Mo, Au, and Pt/Ir. W tips are obtained by etching electrochemically whereas Pt tips can be obtained by simple mechanical cutting.

Along with electronics and mechanical parts, suitable software is required to analyze the STM data. There are some good programs in the market. We use scanning probe image processor (SPIP) by Image Metrology, Inc.

Tip and surface interaction is very complex [153]. One has to be very careful when scanning the surface. There are many possible things that can cause problem such that dirt on the tip could mediate a mechanical interaction between surface and tip or etching residue. For example, the tip may pick up a Si-cluster which forms a monoatomic apex with a p_z like dangling bond. As a result, work function may seem lower than its original value and final image will somewhat different. The native WO_3 oxide layer has to be removed in UHV to get a good tunneling current. Some *in situ* methods have been proposed during the scanning to overcome this problem such as oscillation the tip from peak to peak [154], increasing bias to 7-10 V for 2-4 line scans. By this treatment some W atoms may walk to the tip apex due to the nonuniform electric field and form a nanotip. Alternatively, there are other methods available such as operating the tip at elevated bias and current (10nA) at the same time, intentional crash of the tip to eliminate

the oxide, letting the tip scan a very large area over a long period of time, and moving the tip 4-5 times during the voltage pulse. Other post processing tip procedures have also been present such as *ex situ* HF etching, annealing at high temperatures (above 725 °C radiative heating in our system) or ion milling.

IV. 4. Si(100) SURFACE

The Si (100)-2x1 surface is probably the most important surface because all the silicon integrated circuits are made on this surface. Experiment were performed on 0.060-0.075 Ωcm *p*-type B-doped Silicon wafers that were oriented to $\langle 100 \rangle$ and 0.025-0.05 Ωcm *n*-type Sb-doped Silicon wafers with an orientation along $\langle 100 \rangle$. The similar defects were observed in both samples, indicating that they are not associated with dopant type [155].

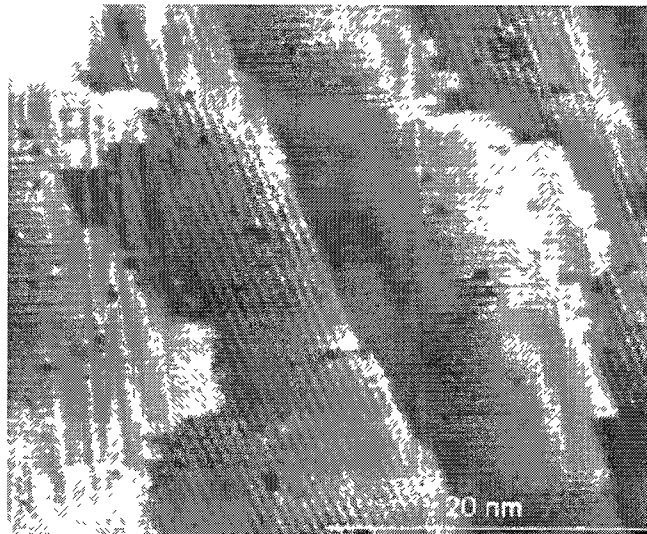


FIG. 13. Clean reconstructed Si(100) surface.

In the bulk like terminated surface, each of the top layer atoms is bonded to two atoms in the second layer, leaving two dangling bonds on each top-layer atom. Because

the bonds between the dimmer Si atoms are occupied and the dangling bonds at the top-layer Si atoms are unoccupied, the STM image at the positive bias and negative bias should be different. The image above was acquired with a sample bias of -1.25 eV and with tunneling current 650 pA at room temperature so that the STM image reflects the spatial distribution of the occupied surface states. This image shows the rows of dimmers and in some place individual dimmers can be seen. In this picture; we observed a relatively high density of defects. Several types of defects were observed and three of them which are A, B, and C-Type was labeled. At the negative bias, the defects A, B, and C appear as depressions. (C-type appears as a high protrusion next to a depression). The defects A appear to be dimmer vacancies in which two Si atoms lying along $\langle 011 \rangle$ were absent. If double dimmer vacancies were observed, this is called defect B. C-Type is another kind of defect in which one Si atom on the second layer is missing was observed as a bright spot in the unoccupied-state STM image and as a dark dot in the occupied states. Dimer buckling is fast at room temperature but defects or steps stabilize the buckling and introduce the pattern seen at the step at the top of the image. C-type defect seems be the size of two dimmers with a bright spot on one side and dark part on the other side of a dimmer row. Most of those appear to have mirror symmetry along the dimmer row with respect to a mirror plane bisecting the bright spot. In the filled state images, the bright region is composed of two subunits each of which is separated by a depression at the position of the mirror plane. On the other hand, it does not have such a separation in the empty state. The brightness of the spot in the filled-state is considerably weaker than the corresponding spots of the host. However, the counterpart in the empty state images stands out against the host image [156].

CHAPTER V
EXCITATION-INDUCED GERMANIUM QUANTUM DOT FORMATION ON
Si(100)-(2X1)

V. 1. INTRODUCTION

While most semiconductor devices are based on silicon, its indirect bandgap, and the resulting low probability of radiative transitions, limits its optoelectronics applications. Devices employing Ge/Si epitaxial layers can overcome this restriction[157]. For example; a dense array of small, narrow size distribution Ge islands embedded in Si layers can be used for light emission where electron hole pairs are captured in the Ge islands. Growth of Ge on Si is a classical model of the Stranski-Krastanov growth-mode, also known as layer-plus-island growth, where growth starts in a uniform layer-by-layer growth up to ~ 3 monolayer [1 monolayer (ML) is equivalent to 6.78×10^{14} atoms/cm² on a Si(100) surface.] The lattice mismatch (misfit) between Ge and Si ($a_{\text{Ge}} = 0.566$ nm, $a_{\text{Si}} = 0.543$ nm) causes elastic strain which increases as the Ge film grows on the Si surface. With the increase of strain energy, the competition between chemical potential of the deposited film and strain energy eventually causes the film to continue through three-dimensional (3D) island growth beyond a critical layer thickness around 3 ML. The value of the misfit is the key factor for the relief mechanism. Three dimensional island formation leads to a partial relaxation of strain. Those islands could be dislocation free or coherent and their shapes change during growth.

Pulsed laser induced electronic processes leading to surface structural modifications have been shown to occur when the laser intensity is below the melt threshold [17-19, 158]. Recent scanning tunneling microscopy (STM) studies have

demonstrated that laser pulses well below the melt and ablation thresholds induce bond rupture at individual atomic sites on several semiconductor surfaces via a process that is purely electronic [20-22]. The laser-induced electronic bond rupture causes structural changes on the surface which depend strongly on the surface studied.

Low temperature thin film growth is strongly desirable in microelectronic fabrication. In Si/Ge, it has been long recognized that one way to suppress misfit dislocations is by lowering the growth temperature [12]. To lower the epitaxial growth temperature, extrinsic assistance by energetic particles, such as ions, electrons and photons, have been used to add energy to promote the migration of adsorbed atoms at the surface [13-15].

Treatment of silicon surfaces by a Nd-doped yttrium aluminum garnet (Nd:YAG) laser was used to improve surface wettability and adhesion characteristics [16]. Also, illumination of silica substrates with a very low intensity diode laser during deposition was reported to unify the clusters' shapes and narrow the size distribution of Ga nanoparticles grown at ~ 100 °C [159]. Moreover, irradiation by a few hundred eV electron beam during deposition of CeO₂ on Si was reported to enhance surface epitaxy by reducing the required temperature for epitaxial growth from 820 °C to 710 °C [13]. In another work, a low-energy electron beam was used to modify the surface and achieve high quality GaAs film grown on an insulator on silicon [15]. Pulsed ion-beam irradiation during heteroepitaxy of Ge on Si led to modifying the average size and size distribution of Ge islands grown by molecular beam epitaxy (MBE) [160]. Post-deposition nanosecond pulsed laser treatment of Ge quantum dots (QD) grown on Si reduced the QD surface density, modified their composition, and increased their average size, making the

QD size more uniform after the treatment [161]. Nonthermal laser induced desorption has also been widely studied for different metals and semiconductors [162-164].

We have recently studied the effects of nanosecond pulsed laser-induced electronic excitations on the self-assembly of Ge QD on Si(100)-(2x1) grown by pulsed laser-deposition [165]. Electronic excitations, due to laser irradiation of the Si substrate and the Ge film during growth, were shown to decrease the roughness of films grown at a substrate temperature of ~ 120 °C. At this temperature, the grown films showed no long range order as detected by RHEED. Electronic excitation resulted in the formation of an epitaxial wetting layer and crystalline Ge QD at ~ 260 °C, a temperature at which no crystalline QD formed without excitation under the same deposition conditions. Here we expand the scope of this work by studying excitation effect on deposition at various substrate temperatures and excitation with different laser energy densities. The effect of applying the excitation laser on the growth morphology is studied. It is shown that the excitation laser affects the morphology only when applied during growth with no post-deposition annealing effects observed at the studied laser energy densities. The results are consistent with an electronically driven mechanism that increases surface diffusion of the incoming Ge flux.

V.2. EXPERIMENT

Ge quantum dots were grown in an ultrahigh vacuum (UHV) chamber ($\sim 1 \times 10^{-9}$ Torr) by pulsed laser deposition (PLD). The Ge target was mounted on a rotation stage with a variable rotation speed. Target rotation at 5 rpm was used to minimize the particulate formation during deposition. The laser beam profile on target and target rotation speed were set such that the spatial separation of the laser pulse spots on target

were ~ 0.6 of its full width at half-maximum (FWHM), resulting in ablation of the target surface by no more than two laser pulses. The Si(100) substrates (dimensions of 2.0 mm x 10 mm x 0.5 mm *p*-type boron doped, and resistivity 0.060-0.075 Ω -cm, miscut angle 0.38°) were chemically etched by using a modified Shiraki method before being loaded into the UHV chamber. The Ge target was a 2" disk, 0.5 mm thick, undoped *n*-type, with a resistivity of 45-58.7 Ω -cm. The vacuum system was then pumped down, baked more than 24 hours and, finally, cooled down to room temperature. The Si(100) sample was degassed at $\sim 700^\circ\text{C}$ for another 24 hours and then flashed to $\sim 1200^\circ\text{C}$ for ~ 60 s to obtain the (2x1) reconstruction. The substrates were heated by direct current flow. The surface temperature was initially measured using a combination of a chromel-alumel (K-type) thermocouple that was mechanically attached to the substrate surface and a Mikron MI-GA15 pyrometer. The thermocouple was used for temperature measurement up to $\sim 400^\circ\text{C}$, while the pyrometer was used for higher temperatures. The thermocouple calibration was checked, before installing it into the UHV chamber, using the boiling point temperature of water. A temperature calibration curve relating the surface temperature obtained by the K-type thermocouple and the pyrometer to the sample conductivity was obtained and used for subsequent temperature measurements. This approach was used to avoid complications due to changes in thermocouple properties by repeated flashing at high temperatures. We can measure temperature reproducibly and with an accuracy of $\pm 17^\circ\text{C}$, mainly limited by the accuracy of determining sample conductivity with temperature.

A Q-switched Nd:YAG (wavelength $\lambda = 1064$ nm, full width at half maximum (FWHM) of ~ 40 ns, 10-Hz repetition rate) was split into an ablation beam and an

excitation beam of nonequal powers by means of a half wave-plate and a thin film polarizing beam splitter. The *p*-polarized ablation beam was focused on the rotating Ge target to a spot size $\sim 400 \mu\text{m}$ (measured at $1/e$ of the peak value), resulting in a laser energy density of $\sim 5 \text{ J/cm}^2$. The *s*-polarized excitation beam was left unfocused with a beam diameter of $\sim 6.0 \text{ mm}$ (measured at $1/e$ peak value) and was used to irradiate the sample surface. Both the ablation and the excitation laser beams were incident on the Ge target and Si substrate at 45° . A 20-keV well-collimated reflection high-energy electron diffraction (RHEED) electron gun with a spot size less than $90 \mu\text{m}$ diameter was used to monitor the growth dynamics, while a partially coated phosphor screen displayed the electron diffraction pattern, which was recorded by means of charge-coupled device (CCD) camera. The electron beam had a grazing angle $\sim 3^\circ$ with the Si(100) surface. Sample-to-target distance was $\sim 8 \text{ cm}$. The final film thickness measurement was done by a spectroscopic ellipsometer (Woollam M44). Post deposition tapping-mode atomic force microscope (AFM) was used to study the morphology of the film. The Ge films were grown on Si(100)-(2x1) at different substrate temperatures and different laser excitation energies. The growth dynamics and morphology of the films grown under the laser excitation are compared to those grown at the same deposition conditions without excitation laser.

V. 3. RESULTS AND DISCUSSIONS

V. 3. 1. RESULTS

V. 3. 1.1. DEPOSITION AT 390°C

The effect of laser excitation of the substrate for Ge growth on Si(100)-(2x1) was studied for a substrate temperature of 390°C . The Ge was deposited at a rate of ~ 0.03

ML/s (~ 0.003 ML/pulse). The deposition rate was obtained from the final Ge thickness using an ellipsometer. The ablation laser energy density was ~ 5 J/cm². Fig. 14(a) shows a series of RHEED patterns taken for different Ge coverage without applying any laser substrate excitation. Before deposition, a clean reconstructed Si(100)-(2x1) is observed. The RHEED pattern consists of sharp spots aligned on Laue circles.

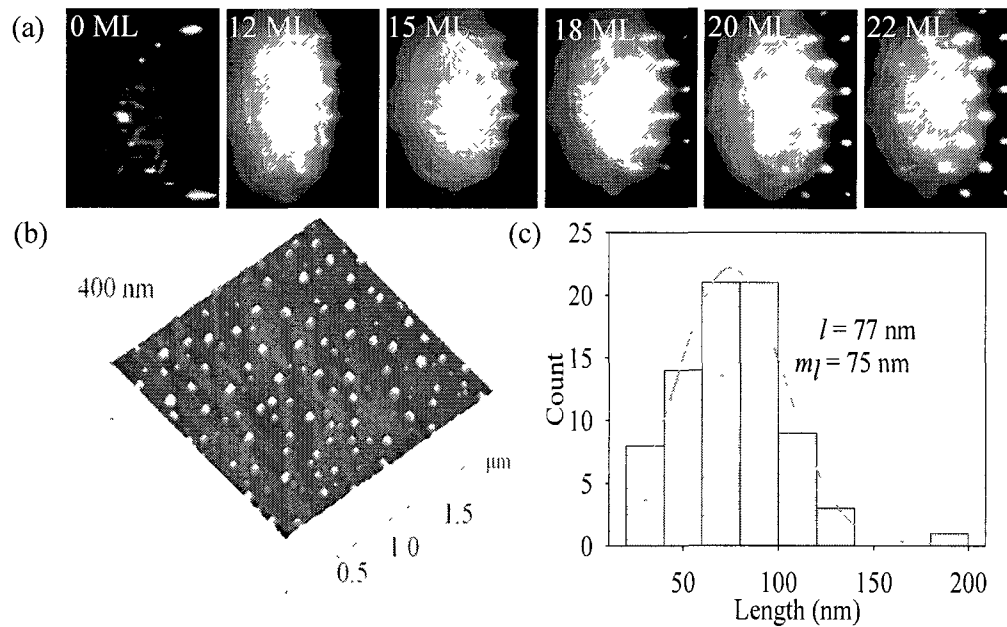


FIG. 14. (a) RHEED pattern at different deposition times for a substrate temperature of 390 °C. 20 keV electron beam energy, angle of incidence with the surface $\sim 2.5 \pm 0.4^\circ$ (b) AFM image shows well distributed islands with different sizes and shapes. (c) Size distribution shows average length $l = 77$ nm and the most expected length, $m_l = 75$ nm.

The diffraction pattern features remain unchanged during the initial stage of deposition, corresponding to the epitaxial growth of the wetting layer (~ 3 ML), and then

become elongated streaks, resulting from deposition of Ge atoms making the surface rougher. The RHEED pattern obtained at ~ 12 ML coverage shows elongated transmission patterns. After ~ 15 ML coverage, the streak intensity is reduced. As the deposition further progresses, the surface topography changes and the elongated spots become shorter. Rounded diffraction spots are observed and additional transmission spots appear in the RHEED pattern after ~ 20 ML coverage. If the deposition is further extended, a rounded, intense transmission pattern develops at ~ 22 ML coverage. Rounded spots not falling on Laue circles result from transmission of electrons through faceted islands. The AFM image in Fig. 14(b), taken after deposition of ~ 22 ML, shows well distributed islands with different sizes and shapes. The majority of those islands in this sample are rectangular-based huts and square-based pyramidal shape. The sharp RHEED spots reveal the crystalline nature of these islands. The island density is $5.0 \times 10^9 \text{ cm}^{-2}$, and the coverage ratio is 14.5%. Figure 14(c) shows that the average island length l , measured along the major axis, is 77 nm, and the most expected length m_l is 75 nm. The FWHM of the size distribution is ~ 80 nm. The average diameter and average height are 51 nm and 15 nm, respectively (height-to-base diameter ratio ~ 0.3). The variation in the aspect ratio β , defined as height/lateral size, in these islands is 20%. Examples of rectangular-based huts and square-based pyramidal islands can be seen in Fig. 14(d). The growth of Ge QDs on Si(100) was then studied while applying an excitation laser to the substrate. Figure 15(a) shows RHEED patterns obtained during growth of Ge on Si(100) while an excitation laser with an energy density of $106 \pm 10 \text{ mJ/cm}^2$ is applied to the substrate. The Si(100)-(2x1) reconstruction is visible before deposition. One may notice that the initial RHEED pattern of the (2x1) reconstructed substrate looks slightly different

when comparing Fig. 14(a) with Fig. 15(a) due to slight differences in the electron angle of incidence, how much of the electron beam is intercepted by the sample, and day-to-day variations in the electron beam incidence azimuth and beam quality. All depositions were done on (2x1) reconstructed substrates and the results were not sensitive to these variations in the initial RHEED pattern of the substrate. An elongated RHEED streak pattern is observed at Ge coverage of ~ 10 ML. As the Ge coverage increases, the intensity of the streaks increases, as shown in the RHEED pattern taken at ~ 13 ML.

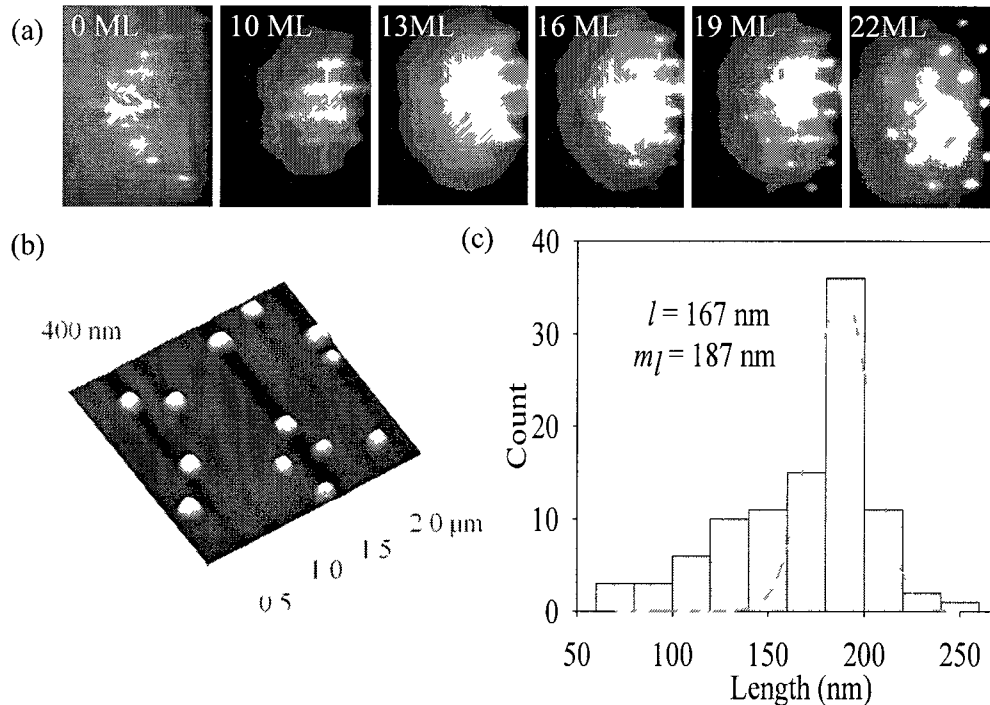


FIG. 15. (a) RHEED pattern obtained at different deposition times. Excitation laser energy density = 106 ± 10 mJ/cm². (b) AFM image. (c) Island size distribution. Average length l and most expected length m_l are 167 and 187 nm, respectively.

Round spotty RHEED patterns start to appear after ~ 16 ML coverage. At ~ 19 ML, the elongated streaks become faint and rounded in shape, indicative of the new facet formation in the grown domes. The RHEED pattern shows well defined transmission features with sharp spots after ~ 22 ML. With the use of the excitation laser at a substrate temperature of $390\text{ }^\circ\text{C}$, the Ge coverage that causes the formation of a transmission pattern becomes larger than without excitation. The corresponding AFM image in Fig. 15(b) shows that the film morphology consists of mainly multifaceted dome-shaped islands coexisting with a small fraction of square-based pyramids. Those islands have a narrow size distribution, as shown in Fig. 15(c). With laser substrate excitation, the island density reduces by a factor of 10 to $\sim 4.7 \times 10^8\text{ cm}^{-2}$, and the coverage ratio decreases to 8.0%. Average height of the islands is 35 nm but some of them can reach up to 56 nm. The mean diameter of those islands is ~ 139 nm, giving rise to a height-to-base ratio ~ 0.25 . Average island length l is ~ 167 nm, while the most expected length m_l is 187 nm, as shown in Fig. 15(c). The FWHM of the size distribution graph decreased to 45 nm compared to that without laser excitation shown in Fig. 15(c). The variation in the aspect ratio β in these square-based domes is 12%. At a substrate temperature of $390\text{ }^\circ\text{C}$, the island morphology changes when irradiating the silicon surface with the excitation laser. The rectangular-based huts and square-based pyramids transform into dome-shaped islands. Island density, coverage ratio, and variation in size, area, and height decrease, while average length, height, and area increases. Examples of dome-shaped islands and square-based pyramids are shown in Fig. 15(d).

V. 3. 1. 2. DEPOSITION AT 250 °C

The effect of the excitation laser on the Ge growth on Si(100)-(2x1) at a substrate temperature of ~ 250 °C was also studied.

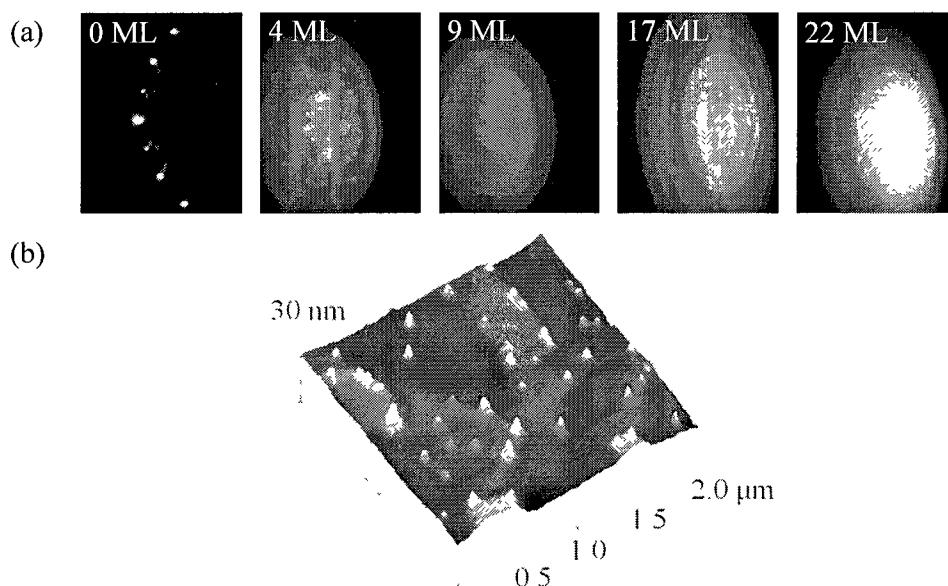


FIG. 16. (a) For deposition at 250 °C without an excitation laser, the RHEED pattern decays continuously with coverage resulting in a diffuse pattern. (b) AFM image could be described as a collection of three dimensional clusters with different shapes and sizes.

For samples grown below 390 °C, the intensity of the Si(100)-(2x1) RHEED spots decay continuously with deposition time until they disappear, resulting in a diffuse pattern. This indicates the formation of 3D structures that collectively lack long-range order, as was confirmed by RHEED and AFM measurements. The Ge growth was observed at 250 °C with an ablation laser energy density of 5 J/cm^2 without excitation laser. For RHEED patterns in Fig. 16(a), some of the diffraction patterns remained while

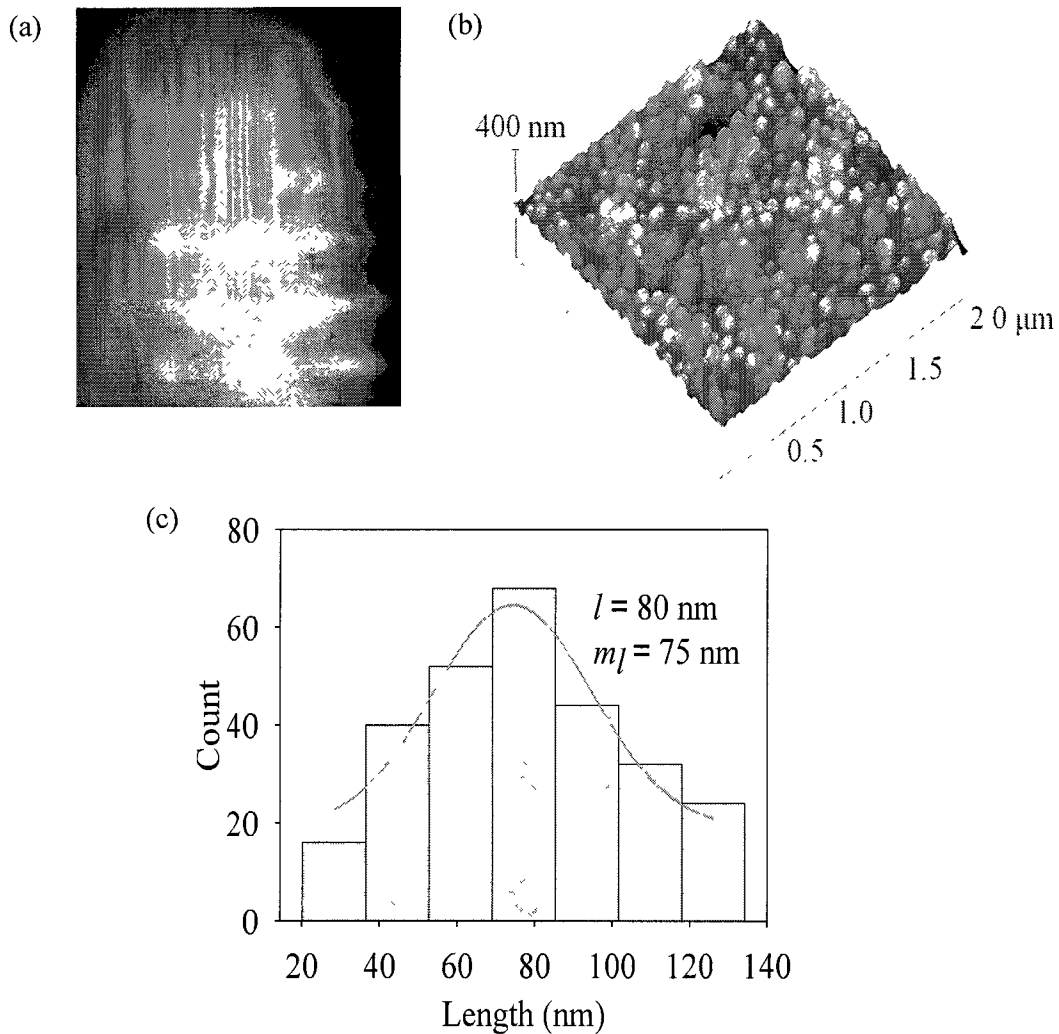


FIG. 17. (a) RHEED pattern of 22 ML Ge deposited at 250 °C with an excitation laser of $37 \pm 4 \text{ mJ/cm}^2$ shows a transmission pattern. (b) AFM image of the surface shows high density Ge islands with a majority of rectangular-based huts. (c) Size histogram from the AFM image.

others were lost after depositing at ~ 4 ML. Almost no pattern appeared after 9 ML, which indicated loss of long-range order on the surface. The AFM image obtained after 22 ML,

shown in Fig. 16(b), could be described as a collection of 3D clusters with different shapes and sizes.

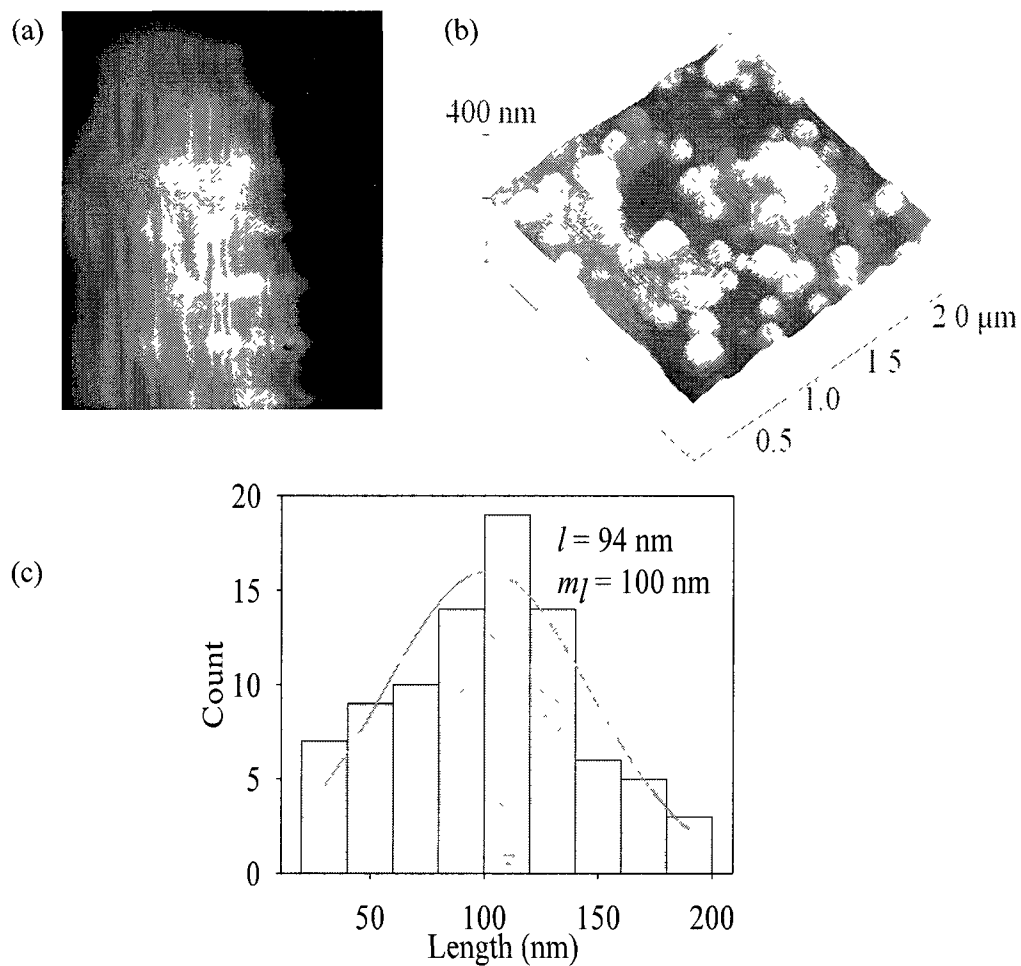


FIG. 18. (a) RHEED pattern of 22 ML Ge deposited at 250 °C with an excitation laser of 77 ± 7 mJ/cm². (b) AFM image of the surface. (c) Size histogram from the AFM image shows that the average length l and the most expected length m_l are 94 nm and 100 nm, respectively.

This type of AFM image is generally observed for heteroepitaxy at low temperatures. Three different laser energy densities were used to study the excitation laser effect at 250 °C. The ablation laser energy density was kept at 5 J/cm², while the excitation laser energy density was varied. For an excitation laser energy density of 37±4 mJ/cm², the RHEED image in Fig. 17(a), taken 22 ML Ge coverage, shows a spotty transmission pattern, indicating 3D growth. The AFM image in Fig. 17(b) shows high-density of Ge islands, most of which are rectangular-based huts. The density of islands is ~6.7 x 10⁹ cm⁻² with a coverage ratio of 24%. Average length l and the most expected length m_l are 80 and 75 nm, respectively, as shown in Fig. 17(c). The average height is ~21 nm and average base diameter is 87 nm, giving a height-to-base diameter ratio of ~0.24.

Next, the excitation laser was increased to 77±7 mJ/cm², while maintaining the ablation laser energy density at 5 J/cm² and the substrate temperature at 250 °C. The RHEED pattern after 22 ML Ge coverage, shown in Fig. 18(a), does not change significantly from that in Fig. 17(a). However, the island density and coverage ratio decreased, while the mean area and length increased, as shown by comparing the AFM image of Fig. 18(b) with that in Fig. 17(b). In Fig. 18(b), Ge islands with different shapes and sizes are visible. Those islands are mainly consisting of rectangular-based huts and some small fraction of square-based pyramids. The average island size increases at this laser energy density when compared to conditions used in Fig. 17(b). This may be due to coalescence of the small islands to larger ones. Island density decreases to 3.0x10⁹ cm⁻² and the coverage ratio also decreases to 14%. Figure 18(c) shows that the average length also increases to 94 nm, and the most expected length at this condition becomes ~100

nm. The average height is ~ 23 nm and average base diameter is ~ 91 nm giving a height-to-base diameter ratio of ~ 0.25 .

The excitation laser density was finally increased to 106 ± 10 mJ/cm² while the substrate temperature was kept at 250 °C.

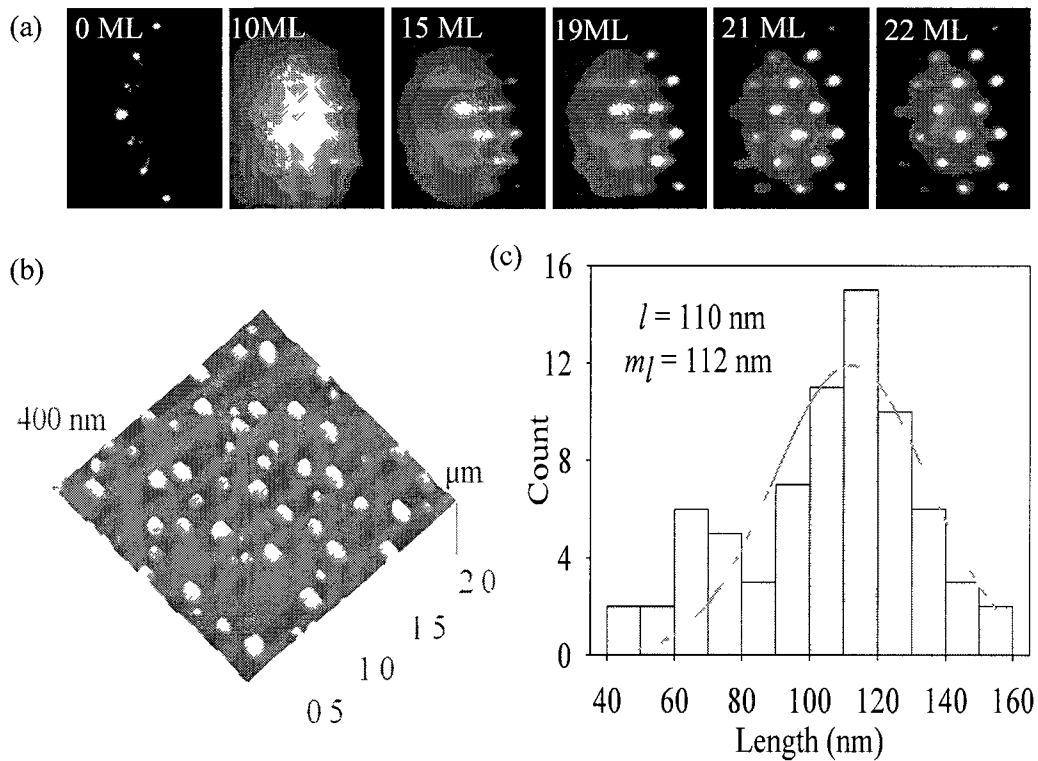


FIG. 19. (a) RHEED patterns recorded at different Ge coverage deposited at 250 °C with an ablation laser of 5 J/cm² and an excitation laser of 106 ± 10 mJ/cm². (b) AFM image of the final 22 ML Ge film shows that film is consisting of rectangular-based huts, square-based pyramids along with some multifaceted domes. (c) Size histogram of the AFM image shows that the average length l and the most expected length m_l are 110 and 112 nm, respectively.

Figure 19(a) shows RHEED patterns obtained at different Ge coverage. A clean, reconstructed Si(100)-(2x1) surface is obtained prior to Ge deposition. After ~10 ML, elongated streaks appear, while the first rounded pattern forms at ~15 ML. The intensity of the RHEED diffraction streaks decreases with coverage and those elongated streaks almost disappear at ~19 ML, while round transmission features become strong. Two more transmission features appear after depositing ~21 ML, indicative of the formation of new facets as the islands grow. AFM images and its size distribution for this sample after 22 ML coverage are shown in Figs. 19(b) and 19(c). Three distinctive island shapes are observed. These are rectangular-based huts, square-based pyramids, and some multifaceted domes, shown in Fig. 19(d).

Comparing the Ge island morphology at these conditions to that obtained at the lower excitation laser energy density shows a decrease in island density and an increase in the average area and length as the laser energy density is increased. For an excitation energy density of $106 \pm 10 \text{ mJ/cm}^2$, the island density is $\sim 1.4 \times 10^9 \text{ cm}^{-2}$, coverage ratio 11%, with average island length 110 nm and most expected length 112 nm, as shown in the island size distribution in Fig. 19(c). The average height is ~27 and average base diameter is ~113 nm, giving rise to height-to-base diameter ratio ~0.24. The variation in the aspect ratio of the clusters is 23%. The larger island sizes observed here compared to that in Ref. 20 is mainly due to the increases Ge film thickness. Also, in the present study the laser repetition rate was 50 Hz compared to the previously used 10 Hz [165]. Higher pulse repetition rate in PLD reduces surface relaxation between pulses causing agglomeration.

Increasing the excitation laser energy from 37 ± 4 mJ/cm² to 106 ± 10 mJ/cm² for a substrate temperature of 250 °C causes island density and coverage ratio to decrease, while the average area, length, and height of the islands increase and size distribution become narrower when the highest excitation laser energy density is used at this temperature. With the increase in the excitation energy density, the Ge islands become more uniform in size and shape. Their height-to-base diameter ratio remains unchanged as the excitation laser energy density is increased. The island densities obtained in the present experiments are smaller than those obtained in other growth techniques. Island densities varied from 10^9 to 10^{11} cm⁻² in molecular beam epitaxy (MBE) and chemical vapor deposition (CVD) [166, 167]. This may be due to the low deposition rate used. Diffusion length L can be expressed as $L = (Dt)^{1/2}$, where D is the coefficient of adatoms and t is the diffusion time. A higher deposition rate could lead to shorter t , due to competing interactions among the deposited atoms, giving rise to smaller diffusion length. Thus, smaller growth rates produce a smaller density of islands when compared to higher growth rates.

In all the present studies, 1064 nm laser pulses were used with the p-polarized light used for target ablation while s-polarized light used for excitation of the substrate. Both ablation and excitation beams were incident 45° on the surface of the target and substrate, respectively. It is known that s-polarized light couples less to Ge and Si than p-polarized light [168]. It was previously shown that surface vacancies were not formed when the surface was irradiated by laser pulses of 80-fs duration at 2200 nm polarized perpendicular to the Si(111)-(2x1) chain direction. This particular Si surface shows a strong surface transition around 0.45 eV [169]. We are not aware of any Si(100) or Ge

surface specific transitions that couple to 1064 nm laser pulses. Therefore, it is reasonable to expect that the laser polarization only affects energy coupling to the surface.

V. 3. 1. 3. DEPOSITION AT ROOM TEMPERATURE

The effect of the excitation laser was also studied for Ge growth on Si(100)-(2x1) at room temperature.

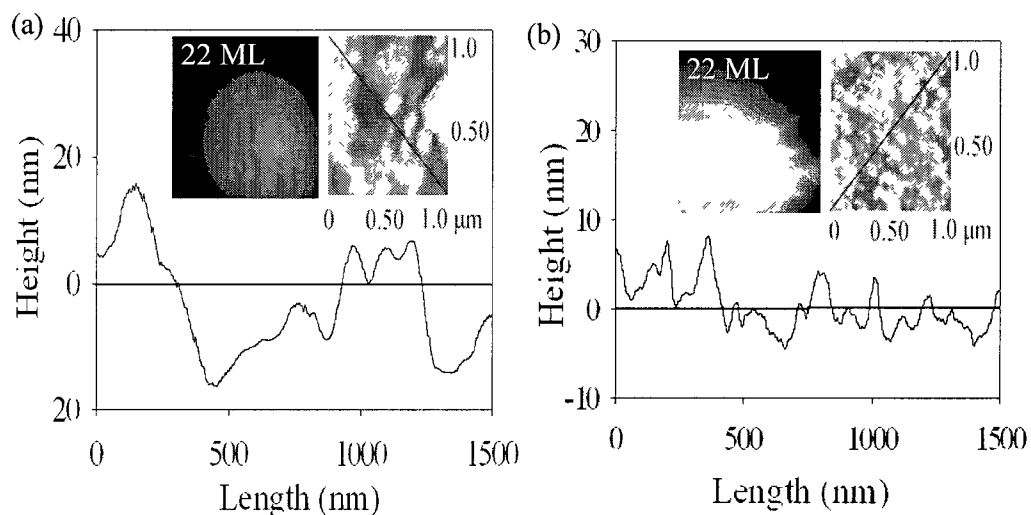


FIG. 20. (a) RHEED patterns recorded at different Ge coverage deposited at room temperature with an ablation laser energy density of 5 J/cm^2 and corresponding AFM image of the final 22 ML Ge film. The line scan across the AFM image shows surface roughness is 8.6 nm without excitation laser. (b) RHEED patterns and AFM image for the same conditions as in (a) but with an excitation laser energy density of $106 \pm 10 \text{ mJ/cm}^2$ showing decrease in surface roughness when the excitation laser is used.

Figure 20(a) shows RHEED patterns taken during growth without laser excitation, while in Fig. 20(b) an excitation laser energy density of $106 \pm 10 \text{ mJ/cm}^2$ was applied.

Without laser excitation the RHEED pattern almost disappeared at Ge coverage of ~ 9 ML, while with laser excitation some diffraction spots are visible even after 22 ML coverage.

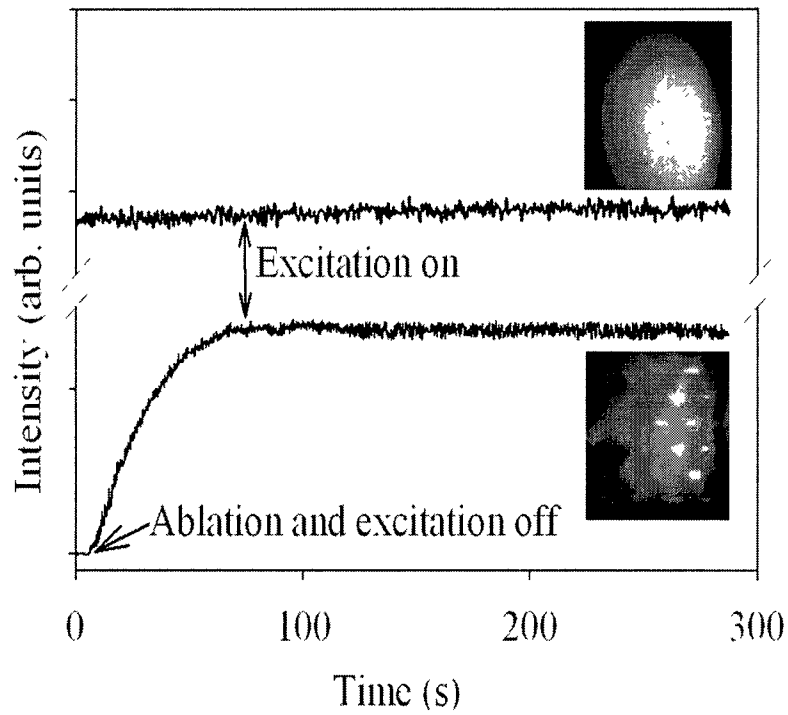


FIG. 21. Intensity of the specular spot after termination of Ge deposition with the substrate maintained at $250\text{ }^{\circ}\text{C}$ for a Ge coverage of ~ 22 ML.

In Fig. 20, an ablation laser energy density of 5 J/cm^2 was used without and with laser excitation. All other experimental conditions, such as laser repetition rate, target rotation speed, and target-to-substrate distance, remained the same for Figs. 20(a) and (b). Hegazy and Elsayed-Ali previously observed that the deposition time required for the RHEED pattern to disappear when the excitation laser was used was 9 times longer than

without excitation laser when the substrate was kept at 120 °C [165]. The decay in the RHEED elastic diffraction intensity (Bragg peaks) and the increase in the inelastic background are associated with increased film roughness with deposition. For the substrate kept at room temperature, applying the excitation laser to the substrate during growth decreases the surface roughness, although epitaxial growth was not achieved. AFM images and single-line scans of surface topography can be seen in Fig. 20(a) for the sample grown without excitation laser and in Fig. 20(b) for the sample irradiated with laser. Mean surface roughness of the sample grown at room temperature without excitation laser was found to be 8.6 nm, whereas, with laser excitation the mean surface roughness was 2.1 nm.

The possibility of altering the surface properties by post-deposition laser irradiation was tested. Figure 21 shows the intensity of the RHEED specular spot after termination of Ge deposition with the substrate maintained at 250 °C for Ge coverage of ~22 ML.

In the bottom scan, both the ablation laser (fluence 5 J/cm²) and the excitation laser (106±10 mJ/cm²) were turned off at time $t = 0$. In this case, the film had grown epitaxially due to the presence of the excitation laser. Upon growth termination, the RHEED intensity showed the usual recovery in a time that depends on surface diffusion. We then only turned on the excitation laser at $t = 75$ s. The intensity of the specular beam did not change, thus showing no surface annealing by post-deposition application of the excitation laser. In the top scan, we only used the same ablation laser fluence also at a substrate temperature of 250 °C to deposit ~22 ML Ge. No excitation laser was used in this case. The ablation laser was turned off at $t = 0$ s. In this case, the Ge film grew as a rough, disordered surface that only showed a RHEED background with no visible

diffraction orders. The intensity reported in Fig. 21 was that of the background that developed in the same location of the specular spot. We did not observe any changes in this intensity, which shows that the post-deposition surface excitation does not result in surface annealing.

V. 3. 2. DISCUSSIONS

The results show that irradiation of the substrate by the excitation laser has an effect on Ge growth similar to that observed when the substrate temperature is raised. Basically, there appears to be a mechanism driven by the excitation laser that results in enhanced Ge adatom surface diffusion. The thickness measurement was performed using an ellipsometer. For samples without laser excitation, the Ge thickness measured after 8000 pulses was $32.5 \pm 1.5 \text{ \AA}$, while with excitation the Ge thickness was $33.7 \pm 1.0 \text{ \AA}$. Therefore, within the experimental error, there appears to be no effect on Ge film thickness due to the excitation laser, and any atom desorption by electronic excitation is too small to affect the grown film.

When the sample is irradiated by the pulsed laser, the initial effect is to generate electron-hole pairs. The bulk silicon is known to have an indirect bandgap of 1.12 eV. Optical measurements show that the Si(100) surface has also an indirect bandgap of 0.44-0.64 eV [170, 171]. Although the Si(100)-(2x1) surface has surface specific optical transitions, their contribution is small for excitation with 1064 nm wavelength [21]. Due to the low surface absorption coefficient ($\alpha = 11 \text{ cm}^{-1}$) of the 1064 nm radiation in Si, photoexcitation takes place mainly in the bulk. Therefore, the primary effect of the 1064 nm nanosecond laser light on the Si substrate is bulk-valence excitation to generate holes and electrons with small excess energies [172]. The energy density of the ns laser pulses

used are well below the melt threshold of Si [173]. We next discuss thermal and nonthermal (electronic) effects of the excitation laser on Ge QD growth.

V. 3. 2. 1. THERMAL EFFECTS

The surface temperature rise due to laser heating is calculated using a one-dimensional, heat-diffusion model. According to this model, the maximum temperature rise due to absorption of the 1064 nm excitation laser in the skin depth of Si ($\sim 60 \mu\text{m}$) is $\sim 23 \text{ }^\circ\text{C}$. The surface temperature drops to the substrate temperature by heat diffusion in $\sim 0.1 \mu\text{s}$. For Ge, the skin depth for 1064 nm is 200 nm, and the maximum temperature rise in this case is $\sim 200 \text{ }^\circ\text{C}$ if irradiated with $106 \pm 10 \text{ mJ/cm}^2$, which is the maximum laser energy density used during the present work. Heat diffusion to the Si substrate limits the temperature excursion time to $< 0.1 \mu\text{s}$. The macroscopic diffusion of Ge atoms adsorbed on the Si(100)-(2x1) surface has been shown to follow the Arrhenius behavior [174]:

$$D = D_0 \exp[-E_T/kT] \quad (36)$$

where $D_0 = 11 \times 10^{-4} \text{ cm}^2/\text{s}$ is a pre-exponential constant, $E_T = 1.17 \text{ eV}$ is the activation energy, and k and T are the Boltzmann's constant and temperature, respectively. The Ge atoms move just $\sim 1.6 \times 10^{-11} \text{ cm}$ in 100 ns at $250 \text{ }^\circ\text{C}$, which is clearly too small to affect the nucleation and growth mechanism. Therefore, we can exclude laser heating as a possible mechanism affecting Ge growth morphology due to the short temperature excursion time and small temperature rise.

V. 3. 2. 2. NONTHERMAL EFFECTS

Energy transfer from laser generated hot electrons to surface adatoms has been reported to improve the crystalline quality [13]. The important role of hot electrons has been demonstrated in the study of molecular desorption from metal surfaces under fs-

laser excitation that can result in high effective electron temperature [175]. However, the photon energy of 1064 nm light is ~ 0.05 eV above the silicon band gap energy, resulting in low free-carrier energy [176]. Thus, for single-photon absorption by bound carriers in Si, the role of hot carriers in increasing surface vibrations is expected to be negligible. Moreover, because of the low intensity of the excitation laser and relatively low substrate temperature, free carrier and two-photon absorption are negligible for conditions considered in the present work [176, 177]. The bandgap of Ge is 0.66 eV; thus, the excitation photon energy is ~ 0.5 eV above the Ge bandgap and, therefore, has enough energy to cause surface modification by electronic excitation.

It is well known that an electron or a photon interacting with the surface can induce an electronic excitation. Emission of ions or neutral particles due to this excitation can occur. Such processes are called desorption induced by electronic transitions (DIET) [178]. Two established DIET mechanisms are the Knotek-Feibelman (KF) model and the Menzel Gomer and Redhead (MGR) model.

Knotek and Feibelman studied the mechanism of electron stimulated desorption of positive ions from certain d-band metal oxides [179]. This mechanism requires initial core-hole creation, followed by the production of two holes via Auger decay and, finally, coulomb repulsion between this positive ion and the cation leads to the emission of a positive ion from the surface. The KF mechanism requires electrons or photons with energies of tens of eV and, therefore, this mechanism can be ruled out in the present study based on the relatively low photon energy used [164].

A more general model of DIET is the Menzel, Gomer, and Redhead (MGR) model that explains the electron desorption due to energy excitation from a bonding to an

antibonding electronic state [180, 181]. In this model, an excitation causes a Franck-Condon transition where the electronic transition occurs without changes in the positions and momentum of the nuclei. It is assumed that the initial excitation occurs by absorption of a photon or electron to a repulsive excited state. This excitation accelerates the adsorbate away from the surface, converting potential energy into kinetic energy of the adsorbate before quenching to the ground state. Depending on how long the adsorbate was accelerated on the repulsive state, this may cause it to overcome the desorption barriers for neutral or atomic species. Because the photon energy in the present study is only ~ 0.05 eV above the Si bandgap, the electronic transition probability for DIET, as described by the MGR model, will be too small to cause any desorption or significant vibrational excitation at the Si surface [180]. Even for Ge, the 0.5 eV excess energy is relatively low compared to surface atom binding energies [182]. Also, the MGR model treats the interaction between light and matter as an isolated event. Since excitons on silicon and also germanium surfaces are not self trapped and the applied photon energy is relatively low, the MGR model for desorption does not appear to be likely for the conditions used in our experiment [183].

In another model, Sumi proposed two-hole localization (THL) and applied his model successfully to explain electronically induced bond rupture at Si and other surfaces [20, 184-186]. The primary assumption in THL is that surface bond rupture leading to neutral-atomic desorption can be induced by strong lattice relaxations associated with localization of two valence holes on the same surface bond. This assumption is based on the Anderson negative U concept suggesting that THL can occur if the Coulomb repulsion energy $E_{Coulomb}$, due to on-site localization of carriers with same charge, is

smaller than the lattice relaxation energy E_{LR} which comes from the lattice distortion and polarization on the localizing particle [187].

THL on surface sites of non-equilibrated valence holes was concluded to be the mechanism responsible for bond breaking when a Si(111)-(2x1) surface was excited by 1064 nm, 8 ns laser pulses [184]. Surface bond rupture rate was studied for Si(111) [21, 158, 169, 184], Si(100) [186, 188, 189], and other materials [158]. The rate of bond rupture varies between 3×10^{-5} and 8×10^{-10} ML/pulse depending on the laser wavelength and fluence. The minimum desorption rate in those studies is $\sim 10^{-5}$ ML/pulse, although the wavelength 1064 nm was found to be inefficient to induce desorption from the Si(100)-(2x1) surface [186].

THL at a surface site affects the surface atom bonding weakening the bond and inducing a strong atom vibration. The localization of the second hole causes strong vibrations of the surface atom, which could lead to bond breaking. These atoms could be ejected due to this transient strong lattice vibration (phonon kick) with a distribution of translational energies that starts from a given onset [19]. Vibrational relaxation after electronic excitation would lead to many phonons being emitted. The lattice forms a continuum of motions that can absorb the energy of the vibrational relaxation. As the energy of the surface atoms increases, the bonded atoms vibrate more strongly. If the phonon kick perpendicular to the surface imparted to a surface atom is not sufficient to cause desorption, the enhanced vibrational motion could lead to increased surface diffusion.

The removal of adatoms when the surface is irradiated by laser pulses below the melting threshold was found to be site selective, depended strongly on wavelength, and

was highly superlinear with respect to excitation laser fluence [158, 190]. It was shown that center atoms on Si(111)-(7×7) have higher probability for desorption than corner atoms [190]. Also, surface atoms neighboring an adatom-vacancy pair are more likely to be removed. Preferential bond rupture nearest to pre-existing vacancies was also observed on the Si(111) surface [20, 21]. Selective removal of the topmost layer was also shown for Si(100)-(2x1) [56]. In this case, localized electronic states at defects, such as vacancies, on the reconstructed surface are believed to be responsible for this selective layer removal.

The process that causes the observed effect of laser irradiation of the substrate must be electronic in nature. A possible scenario involves electron-hole generation in the substrate followed by hole diffusion to the surface and two-hole localization [185]. Yu and Tanimura investigated the laser induced desorption of Si adatoms on Si(100)-(2x1) when the surface is excited by 2.48 eV laser pulses [188]. Their results show that electronic excitation causes desorption of Si atoms from a certain adatom configuration. The desorption yield was super-linearly dependent on the laser fluence and, therefore, was consistent with the two-hole localization model. More importantly, desorption yields with successive laser pulses indicated that the adatom configuration that was reactive to desorption transformed by laser excitation into a different form that is less susceptible to desorption. That work led to the conclusion that surface electronic excitation can be a possible method to reduce surface defects [191, 192]. Bulk valance excitation of Si(111)-(2x1) using 1064 nm laser pulses was shown to result in a surface vacancy formation at preferential sites near existing surface vacancies [21]. The fluence dependence of the rate of surface vacancy generation and the more effective vacancy site generation for n-doped

surfaces were consistent with the two-hole localization model. An important point is that the results indicate that free holes are more effectively trapped at surface-defect sites. This suggests that substrate excitation during deposition causes hole localization preferentially at adatom sites.

For 1064 nm photons, Si has an absorption coefficient of $\sim 11 \text{ cm}^{-1}$ and, therefore, the optical excitation is almost uniform near the surface, resulting in negligible carrier diffusion due to the negligible gradient in carrier density generated near the surface. However, it was suggested that the fast surface recombination can lead to a valence hole density gradient near the surface resulting in hole transport from the bulk to the surface [176]. A laser fluence of 106 mJ/cm^2 results in the generation of a carrier density of $\sim 10^{19} \text{ cm}^{-3}$. Because of the slow carrier decay, the density of holes at the surface can reach $\sim 10^{19} \text{ cm}^{-3}$ at the end of the laser pulse. However, Yu *et al.* found that electronic bond breaking on Si(100)-(2x1) is effectively inactive below a photon energy of 1.9 eV, which is explained to be a result of the indirect band-gap of Si for which the desorption yield was shown to be extremely low for photon energies up to $\sim 1 \text{ eV}$ above the bandgap [193]. An exception to this observation was on Si(111)-(2x1) which has a surface with strong bond ionicity and differs significantly from the Si(100)-(2x1) surface [21]. Therefore, electronic excitation of the Si(100)-(2x1) substrate and two-hole localization at its surface is unlikely to be the mechanism driving epitaxial growth of Ge.

Eaglesham *et al.* showed the existence of a limiting thickness h_{epi} , which depends on the growth rate and temperature, beyond which epitaxy becomes amorphous [194]. The possibility of epitaxial growth of Ge on Si by molecular beam epitaxy was shown to occur at a temperature between 50 and 150 °C for h_{epi} of 30 and 200 Å, respectively, for a

growth rate of 0.2 \AA s^{-1} [195]. The rate of deposition affects h_{epi} , which was shown to be reduced to 50 \AA at $150 \text{ }^\circ\text{C}$ when the rate of deposition was increased to 1.7 \AA s^{-1} . In the present experiment, each laser pulse with energy density of 5 J/cm^2 deposits $\sim 0.003 \text{ ML/pulse}$ ($\sim 1.7 \times 10^{12} \text{ atoms/cm}^2$ per pulse, $1 \text{ ML Ge(100)} \sim 6.23 \times 10^{14} \text{ atoms/cm}^2$). It was shown that the laser plasma plume expands very rapidly ($\sim 10^6 \text{ cm/s}$) perpendicular to the ablated surface [47]. The plume expansion results in a plume width of around several microseconds at a 10 Hz repetition rate [43, 48-50]. This results in an instantaneous deposition rate in the 100s of \AA s^{-1} . Nikiforov *et al.* investigated the limiting thickness for Ge growth on Si(100) by using RHEED [196]. In their work, they assumed that the maximum spot intensity corresponds to the maximum epitaxial layer thickness. In Fig. 16, the maximum RHEED spot intensity during Ge growth was reached at $\sim 4 \text{ ML}$, and beyond that thickness, the intensity started to decrease until it completely disappeared. Therefore, although the process of two-hole localization on the Si(100)-(2x1) surface is suppressed at the 1064 nm excitation wavelength, for our experiment at $250 \text{ }^\circ\text{C}$, epitaxial formation of the wetting layer still occurs up to $\sim 4 \text{ ML}$.

Once the Ge wetting layer is formed, two-hole localization can occur on the Ge surface. At $250 \text{ }^\circ\text{C}$, the indirect Ge energy band gap is 0.57 eV and Ge has a direct band gap at 0.7 eV . The absorption coefficient of 1064 nm in Ge is $1.6 \times 10^4 \text{ cm}^{-1}$, leading to significantly higher electron-hole generation in the Ge wetting layer than the Si substrate. The hole density of germanium due to absorption of the laser pulse is $\sim 10^{23} \text{ cm}^{-3}$. The surface hole density depends on many parameters that include surface recombination and diffusion across the Si/Ge interface. We are not aware of any studies done on electronic bond breaking of electronically excited Ge surfaces. However, the two-hole localization

mechanism, followed by the phonon-kick, is applicable to semiconductors in general. Energetically, this mechanism could be effective on Ge surfaces. For surface bond breaking, the phonon-kick has to transfer enough energy to the top atom along the bond direction to break that bond. If that energy transfer is not sufficient for bond breaking, then, the atom will have a vibrational excitation that can lead to surface hopping. Within the experimental error, we have observed no change in the monolayer coverage for Ge on Si with laser excitation.

Therefore, two-hole localization on the Ge surface can lead to selective energy transfer to the Ge atoms that landed on the surface from the PLD plume since these atoms constitute a defect site. The energy that is preferentially given to these adsorbed atoms can result in their hopping to settle epitaxially on the surface.

Previous picosecond time-resolved RHEED studies of excitation of the three low-index surfaces of Ge with 1064 nm, 100 ps laser pulses have conclusively shown that the surface temperature behaves as expected from a simple heat diffusion model [80, 105, 197, 198]. This rule out an electronic mechanism that transfers energy to surface atoms causing heating above that expected from simple laser absorption in the skin depth followed by heat diffusion. However, we point out that RHEED probes surface atoms over a very large area. The mechanism we are proposing for enhanced surface hopping of the adsorbed Ge atoms is preferential to the adsorbed atoms which is only a very small coverage. Therefore, such preferential enhancement of surface hopping of the adsorbed atoms would not be sufficient to allow it to be detected through RHEED observation of the transient Debye-Waller factor.

Charge transfer from the substrate to the adsorbate or vice versa during thin film growth has been reported to affect the film quality and that atoms may gain vibrational energy because of a charge transfer process [199-201]. Charge transfer interactions are believed to be important and can occur at the interface of a Si substrate [202]. Photoinduced charge transfer between the Ge atoms and Si substrate or the Ge wetting layer may affect the nucleation by increasing the vibrational energy of surface atoms, causing an increase in the surface diffusion. The low photon energy used in the present study, with only ~ 0.05 eV excess energy above the Si bandgap at 300 K and, makes this process ineffective for a Si surface. A possible role of charge transfer between the Ge surface and the Ge adatoms cannot be ruled out at the present time.

V. 3. 2. 3. ENHANCED EFFECTIVE SURFACE DIFFUSION

Direct laser heating can be ruled out as the mechanism causing the modification of Ge QD growth on Si(100)-(2x1). However, the exact mechanism responsible is not clear. Enhancement of the effective surface diffusion of adatoms by the excitation laser could be involved. The rate of surface diffusion of atoms D follows an Arrhenius form with temperature and is proportional to the vibrational energy in the reaction coordinate. There are two possible scenarios as stated in Itoh and Stoneham [17]. If surface energy changes due to the electronic excitation, one expects an Arrhenius behavior with a reduced barrier, which can be seen in the form of $\exp[-(E_T - X)/kT]$. However, if this vibrational energy is increased by a fraction of the recombination energy, then one expects an extra term in the denominator as a result of temperature dependence in the form of $\exp[-E_T/(kT + X)]$. In both cases, the surface diffusion coefficient increases.

V. 4. CONCLUSION

We have studied Ge QD formation on Si(100)-(2x1) with different substrate temperatures and excitation laser energy densities. The excitation laser reduces the epitaxial growth temperature to 250 °C for a 22 ML film. In addition, applying the excitation laser to the substrate during the growth changes the QD morphology and density and improves the uniformity of quantum dots fabricated at 390 °C. At room temperature, applying the excitation laser during growth decreases the surface roughness although epitaxial growth could not be achieved. We have ruled out thermal effects and some of the desorption models. Although further studies are needed to elucidate the mechanism involved, a purely electronic mechanism of enhanced surface diffusion of Ge atoms is proposed. Further investigation of this electronic modification of thin film growth would benefit from surface diffusion measurement during growth and the use of *in situ* atomic probe microscopy to observe the development of the wetting layer and the quantum dots and how this is affected by electronic excitation.

Although the effects of electronic excitation on shown for Ge growth on Si(100), the basic principle involved is expected to apply to other semiconductor heteroepitaxy. Achieving low temperature epitaxial growth is an important step for high level integration. Low temperature epitaxy also limits the redistribution of impurities, reduces intermixing in heteroepitaxy, and restricts the generation of defects by thermal stress. The ability to prepare self-assembled quantum dots with reduced size distribution by electronic excitation is also important for many applications because both the optical and electronic properties of a quantum dot depend on its size. The use of electronic excitation

to provide some control on thin film and quantum dot growth could be an important tool in fabricating devices based on self-assembly.

CHAPTER VI
ELECTRONICALLY ENHANCED SURFACE DIFFUSION DURING Ge
GROWTH ON Si(100)

VI. 1. INTRODUCTION

Recent experiments have shown that electronic excitation of the substrate during growth can assist epitaxial growth [13, 33, 41], modify surface morphology, and reduce size distribution of grown quantum dots (QDs), making them more uniform [33, 160, 161]. Enhancement of the effective surface diffusion of adatoms by the excitation laser was proposed as a possible mechanism responsible for the observed effects [17, 33].

Surface diffusion is a critical parameter for epitaxial thin film growth since diffusion allows the adatoms to hop to appropriate, active lattice sites. For surface diffusion to occur, a certain amount of energy must be available to the adatoms. This energy can originate from kinetic or potential energy of the adsorbate or can be supplied thermally by substrate heating. The rate of surface diffusion depends on a variety of factors, including the energy of the incoming adsorbate, the strength of the surface-adatom bond, orientation of the surface lattice, densities of atomic steps, surface reconstruction, attraction and repulsion between surface species, and externally supplied energy [53]. The surface diffusion coefficient D_s is known to follow an Arrhenius form with temperature and is proportional to the vibrational energy in the reaction coordinate [53]. Several external energy sources applied to surfaces have been shown to increase surface diffusion. These include low energy ion bombardment and the resulting momentum transfer to the surface species [203, 204], charge carrier injection [205], and light-induced migration of Ag atoms originating from electronic excitation [206]. The

diffusion of Ge adatoms on Si(100)-(2x1) is highly anisotropic in nature with diffusion favored in a direction parallel to the dimer rows [174]. Surface migration is at least 1000 times faster along the dimer rows than perpendicular to them [207]. The surface diffusion coefficient of Ge atoms depends on the surface orientation. For example, Ge atoms have almost two times greater diffusion coefficient on Si(100) than Si(111) [208]. The diffusion coefficient of Ge adatoms on Si(001) was found to be $D_{Ge} \sim 2.53 \times 10^{-7} \exp(-0.676 \pm 0.03 \text{ eV}/kT) \text{ cm}^2/\text{s}$ in the temperature range between 650 and 725 °C [209]. We report on the effect of laser substrate excitation on surface diffusion during growth of Ge on Si(100)-(2x1) by pulsed laser deposition (PLD). Results show that applying the excitation laser during the growth increases the surface diffusion coefficient in a way that is exponentially dependent on laser intensity.

The surface diffusion coefficient was measured using reflection high-energy electron diffraction (RHEED) intensity recovery after the growth interruption. The intensity of the RHEED diffraction spots depends on the surface structure and morphology. Increased surface roughness reduces the diffraction spot intensities. Therefore, immediately after starting the Ge growth by ablating the Ge target, the intensity of RHEED diffraction orders decreases. For epitaxial growth, the RHEED intensity can recover when the growth is interrupted. This intensity recovery time depends on the amount of time it takes the surface species to rearrange to their final locations. RHEED recovery upon deposition termination can generally be described by a two-exponential decay [210], $I = A_0 - A_1 \exp(-t/\tau_1) - A_2 \exp(-t/\tau_2)$, where A_1 and A_2 are usually positive constants and τ_1 and τ_2 are temperature-dependent time constants of the fast and slow stages, respectively. Those time constants could be explained as diffusion

along a step edge and diffusion across the terrace for fast and slow recoveries, respectively. The fast processes are generally attributed to smoothing of the front growth profile, while slow processes are attributed to long-range order reactions such as rearrangement of terraces and/or the reduction of one-dimensional disorder [210, 211]. It is often, as observed in the present study, that the RHEED recovery curve can be well described by a one exponential with time constant τ [210]. For a vicinal surface, the surface diffusion coefficient D_s is related to the average terrace width L by $D_s \sim L^2/\tau$, where D_s is the diffusion coefficient and τ is the relaxation time constant which depends on the density of nucleation sites and diffusion velocity [210,212].

VI. 2. EXPERIMENT

The Si(100) substrates (*p*-type boron doped, resistivity 0.060-0.075 Ω -cm, miscut angle 0.38°) were chemically etched by using a modified Shiraki method before being loaded into the UHV chamber (base pressure $\sim 7.0 \times 10^{-10}$ Torr). The Ge target was undoped *n*-type with a resistivity of 45–58.7 Ω -cm. The Si(100) sample was degassed at ~ 700 °C in UHV for 24 hours and then flashed to ~ 1200 °C for ~ 60 s to obtain the (2x1) reconstruction. The substrates were heated by direct current flow. The surface temperature was measured using a combination of a chromel-alumel (K-type) thermocouple that was mechanically attached to the substrate surface and a pyrometer. A Q-switched Nd:YAG (wavelength $\lambda = 1064$ nm, full width at half maximum (FWHM) of ~ 40 ns, 10-Hz repetition rate) was split into an ablation beam and an excitation beam of nonequal powers by means of a half wave-plate and a thin film polarizing beam splitter. The *p*-polarized ablation beam was focused on the rotating Ge target to a spot size ~ 400 μ m (measured at 1/e of the peak value), resulting in a laser energy density of ~ 5 J/cm².

The *s*-polarized excitation beam was left unfocused with a beam diameter of ~ 6.0 mm (measured at $1/e$ peak value) and was used to irradiate the sample surface. Both the ablation and the excitation laser beams were incident on the Ge target and Si substrate at 45° . Sample-to-target distance was ~ 8 cm. A 20-keV well-collimated RHEED electron gun with a spot size less than $90 \mu\text{m}$ diameter was used to monitor the growth, while a partially coated phosphor screen displayed the electron diffraction pattern, which was recorded by means of charge-coupled device (CCD) camera. The electron beam had a grazing angle $\sim 2.5 \pm 0.5^\circ$ with the Si(100) surface. The final film thickness measurement was done by a spectroscopic ellipsometer with an accuracy of ± 1 ML. Post deposition tapping-mode atomic force microscope (AFM) was used to study the morphology of the film.

VI. 3. RESULTS AND DISCUSSIONS

We have previously studied the effect of the excitation laser on the Ge growth on Si(100)-(2x1) at a substrate temperature of ~ 250 °C [33]. For samples grown below 390 °C, the intensity of the Si(100)-(2x1) RHEED spots was observed to decay continuously with deposition time until they disappear, resulting in a diffused pattern [33, 165]. This indicates the formation of three-dimensional (3D) structures that collectively lack long-range order, as was confirmed by RHEED and AFM measurements. The AFM image obtained at 250 °C showed a collection of 3D clusters with different shapes and sizes [33].

In the present study, the substrate temperature was ~ 250 °C and the ablation laser energy density was 5 J/cm^2 , while the excitation laser energy density was varied. Figure 22 shows a set of RHEED patterns of Ge QDs grown on Si(100)-(2x1) with different

excitation laser energy densities applied to the substrate. For Figs 22(a) through (f), the RHEED patterns were obtained after 8000 laser pulses. Post-deposition analysis of the Ge film thickness using an ellipsometer confirmed that the films had a thickness of 22 ML. The corresponding AFM images of these films are shown in Figs 23(a) through (f).

VI. 3. 1. RESULTS

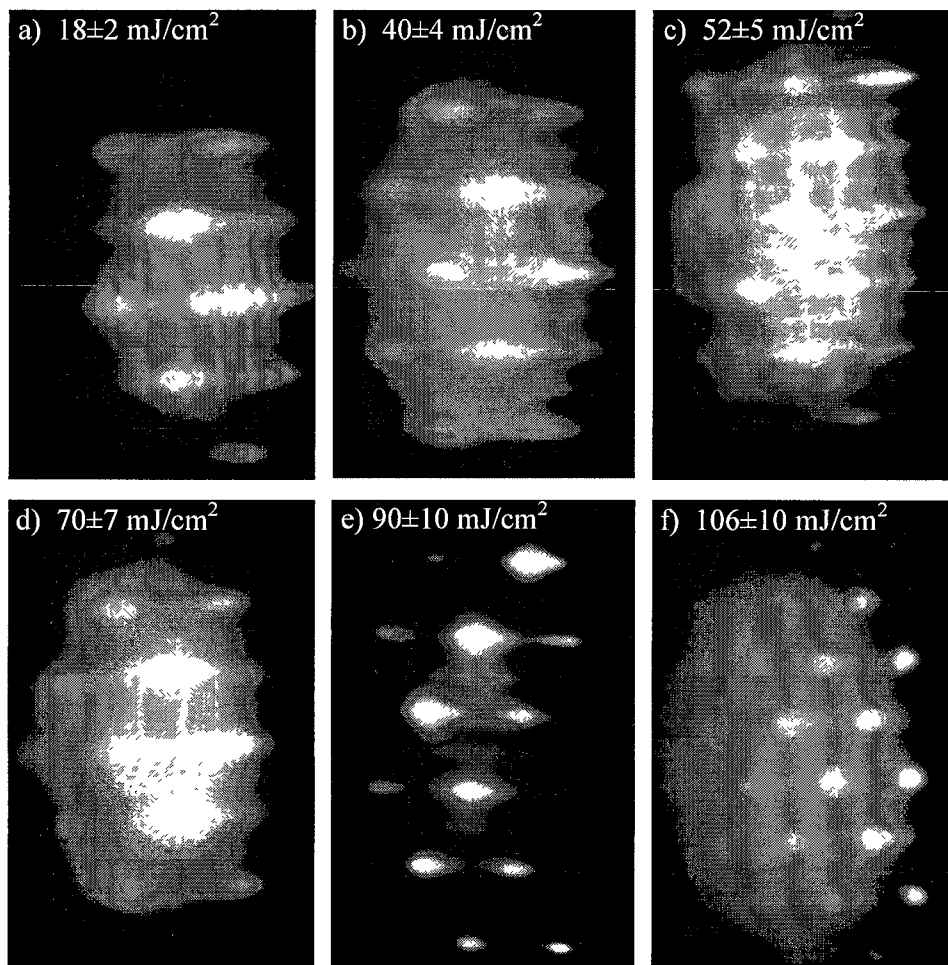


FIG. 22. The excitation laser energy density is (a) $18 \pm 2 \text{ mJ/cm}^2$, (b) $40 \pm 4 \text{ mJ/cm}^2$, (c) $52 \pm 5 \text{ mJ/cm}^2$, (d) $70 \pm 7 \text{ mJ/cm}^2$, (e) $90 \pm 10 \text{ mJ/cm}^2$, (f) $106 \pm 10 \text{ mJ/cm}^2$.

For an excitation laser energy density of $18 \pm 2 \text{ mJ/cm}^2$, the RHEED image in Fig. 22(a) shows a spotty transmission pattern, indicating 3D growth. The AFM image consists of high-density Ge islands, most of which are rectangular-based or square-based islands with some small fraction of domes. An individual island is shown in the inset of Fig. 23(a). The density of islands is $\sim 7.5 \pm 1.5 \times 10^9 \text{ cm}^{-2}$. Mean length, l , is $57 \pm 28 \text{ nm}$. The mean height is $\sim 9 \pm 4 \text{ nm}$.

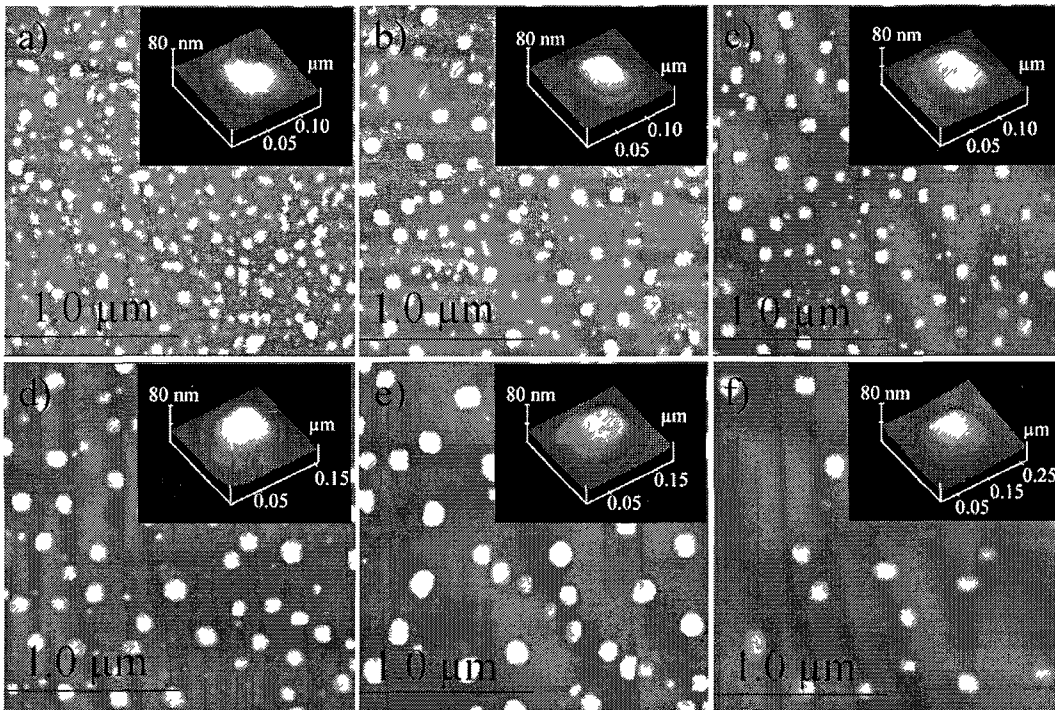


FIG. 23. The AFM images of the individual islands with excitation energy density of (a) $18 \pm 2 \text{ mJ/cm}^2$, (b) $40 \pm 4 \text{ mJ/cm}^2$, (c) $52 \pm 5 \text{ mJ/cm}^2$, (d) $70 \pm 7 \text{ mJ/cm}^2$, (e) $90 \pm 10 \text{ mJ/cm}^2$, (f) $106 \pm 10 \text{ mJ/cm}^2$.

We next increased the excitation laser to $40 \pm 4 \text{ mJ/cm}^2$ while all other conditions remained as in Fig. 22(a). The observed RHEED pattern, shown in Fig. 22(b), does not

change significantly from that in Fig. 22(a). However, the island density and coverage ratio decreased, while the mean area and length increased, as observed by analysis of the AFM images. In Fig. 23(b), Ge islands with different shapes and sizes are visible. A single island at this condition could be seen in the inset of Fig. 23(b). Those islands mainly consist of rectangular-based and square-based pyramid-shape islands while fraction of domes was increased. The shape of the islands becomes more uniform. The average island size increased when compared to conditions used in Fig. 23(a). This is consistent with coalescence of the small islands to larger ones. The island density decreased to $5.0 \pm 1.0 \times 10^9 \text{ cm}^{-2}$. The mean length also increased to $60 \pm 30 \text{ nm}$ with an average height of $\sim 13 \pm 5 \text{ nm}$.

When the laser energy density was increased to $52 \pm 5 \text{ mJ/cm}^2$, the RHEED streaks upon growth termination, shown in Fig. 22(c), are less elongated and become slightly more intense than in Figs 22(a) and (b). The corresponding AFM image shows an increase in the size of islands while their lateral aspect ratio becomes smaller. The island density is $\sim 9 \pm 0.8 \times 10^9 \text{ cm}^{-2}$ while the mean length and height are $\sim 75 \pm 27 \text{ nm}$ and $\sim 16 \pm 4 \text{ nm}$, respectively. One of the individual islands is shown in the inset of Fig. 23(c).

This trend continued as the excitation energy density was increased to $70 \pm 7 \text{ mJ/cm}^2$. In Fig. 22(d) the elongated RHEED transmission pattern becomes more rounded showing a spotty transmission pattern not falling on Laue zones, indicating the growth of 3D islands. A single island is visible in the AFM image in inset of Fig. 23(d). It is seen that the lateral aspect ratios for those islands are getting smaller with the increase of the excitation laser energy density while the mean length and height increase. In Fig. 23(d),

the island density is $\sim 2.5 \pm 0.5 \times 10^9 \text{ cm}^{-2}$; the mean length for those islands is $\sim 90 \pm 40 \text{ nm}$; and the mean height is $\sim 21 \pm 7 \text{ nm}$.

For an excitation laser energy density of $90 \pm 10 \text{ mJ/cm}^2$, the final RHEED pattern, shown in Fig. 22(e), develops additional transmission pattern compared to Fig. 22(d), indicative of better QD crystalline structure. The islands mainly consist of dome-shaped and rectangular based islands. The corresponding AFM image shows that the island density is $1.5 \pm 0.5 \times 10^9 \text{ cm}^{-2}$, mean length is $110 \pm 40 \text{ nm}$, and mean height is $29 \pm 9 \text{ nm}$. Some individual islands, mainly consisting of dome-shaped islands, are seen in Fig. 23(e).

Finally, the excitation laser energy density was increased to $106 \pm 10 \text{ mJ/cm}^2$. In this case, the final RHEED image becomes much brighter with well-defined spotty pattern and shows more transmission pattern, indicating new facet formation and increased crystalline quality, as shown in Fig. 22(f). The resulting AFM image, in Fig. 23(f), shows that the island density is further reduced to $0.8 \pm 0.3 \times 10^9 \text{ cm}^{-2}$, mean length increased to $131 \pm 33 \text{ nm}$, and mean height became $\sim 33 \pm 7 \text{ nm}$. The islands became more uniform in size and shape and developed mainly dome shapes. These results show that increasing the excitation laser energy from $18 \pm 2 \text{ mJ/cm}^2$ to $106 \pm 10 \text{ mJ/cm}^2$ at a substrate temperature of $250 \text{ }^\circ\text{C}$ causes Ge island density, lateral aspect ratio, and coverage ratio to decrease, while the average area, length, and height of the islands increase and become more uniform in size and shape. The development of the RHEED patterns and associated Ge quantum dot morphology with the increase in the laser excitation energy density is analogous to what is observed when the substrate temperature is raised during deposition [33]. Raising the substrate temperature is known to increase surface diffusion.

To investigate the effect of electronic excitation on surface diffusion, we observed the RHEED intensity recovery of the specular spot upon growth termination. The characteristic relaxation time constant is obtained from the RHEED intensity recovery curve [211-213]. The surface diffusion coefficients D_s is estimated from $D_s \sim L^2 / \tau$, where τ is the experimentally measured RHEED relaxation time upon growth termination and L is the average terrace length of the vicinal surface.

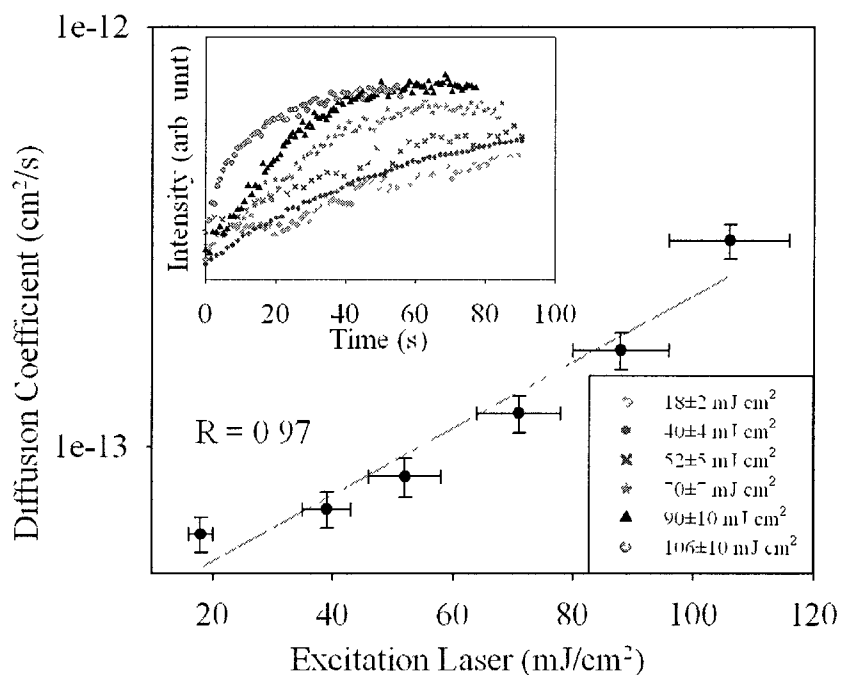


FIG. 24. The surface diffusion coefficient versus excitation laser energy density after 8000 deposition pulses (22 ML). The inset shows the RHEED recovery curves obtained following the growth interruption at different excitation laser energy densities. The surface diffusion coefficient increases with increasing the excitation laser energy density.

Figure 24 shows the specular spot RHEED intensity recovery curves obtained after growth interruption subsequent to 8000 laser deposition pulses. The recovery curves follow a simple exponential growth with a time constant $\tau = 65 \pm 7$ for an excitation laser of 18 ± 2 mJ/cm². Taking the average terrace width $L = 20$ nm, based on the vicinal angle of the Si(100) substrate, a diffusion coefficient $D_s \sim 6 \times 10^{-14}$ cm²/s is obtained. It was previously found that temperature dependence of Ge adatom diffusion coefficient on Si(100) could be approximated by $D_{\text{Si}(100)} = 6 \times 10^{-2} \exp(-1.2\text{eV}/kT)$ cm²/s [208]. At a substrate temperature of 250 °C without any excitation, this approximation gives $D_s \sim 9 \times 10^{-14}$ cm²/s. We were not able to measure D_s at 250 °C without applying the excitation laser, since there is no specular spot at the end of the deposition.

VI. 3. 2. DISCUSSIONS

Applying excitation laser results in epitaxial film growth, allowing the measurement of D_s . We should note that we are measuring the diffusion of Ge on the Ge wetting layer. It was shown that Ge atoms move faster than Si atoms on Ge(111) and the diffusion length increased by a factor of almost 10 when the substrate was changed from Si to Ge [214]. Unlike Ge on Si(100), diffusion of Ge on Si(001) covered by 1 ML of Ge shows nearly isotropic behavior and it has a lower diffusion coefficient [215]. With the increase in the excitation laser energy density, the RHEED intensity recovery time τ was observed to decrease and, therefore, the measured value of D_s was increased, as shown in the inset of Fig. 24. Applying the excitation laser during the growth noticeably increases D_s . A fit of the recovery curve in Fig. 24 gives the dependence of the surface diffusion coefficient on the excitation laser energy density I in mJ/cm² such that $D_s = 5.8 + 0.28 \cdot \exp(0.04I)$, where D_s is in 10^{-14} cm²/s. The correlation coefficient R was found

to be 0.97 from linear regression. For a substrate temperature of 250 °C and laser excitation energy density of 106 ± 10 mJ/cm², τ was 13 ± 2 s corresponding to $D_s = 3.1 \pm 0.3 \times 10^{-13}$ cm²/s.

The value of D_s obtained from the exponential increase of the specular RHEED intensity upon growth termination does not distinguish the diffusion of adatoms, small islands and clusters, and migration of atoms from formed islands. Since we observe a one exponential for RHEED intensity recovery, the recovery time τ does not distinguish between the various surface processes involved. Diffusion of islands and clusters strongly depends on their size and density [216]. Motion of clusters may occur via displacement of individual atoms, sections of the clusters, or clusters moving as a whole [217]. It was also shown that mobility of small clusters decreases with increasing size [218] and the diffusion coefficient of the islands has a power-law dependence on the island size [219]. As the excitation laser energy density was increased, the island nucleation density was observed to decrease. This is consistent with an increase in D_s with excitation.

The surface temperature rise, due to the laser pulse, was calculated using a one-dimensional heat-diffusion model. According to this model, the maximum temperature rise due to absorption of the 1064 nm excitation laser in the skin depth of Si (~ 60 μ m) is ~ 23 °C. The surface temperature drops to the substrate temperature by heat diffusion in ~ 0.1 μ s. For Ge, the skin depth for 1064 nm is 200 nm, and the maximum temperature rise in this case is ~ 200 °C if irradiated with 106 ± 10 mJ/cm², which is the maximum laser energy density used during this work. Heat diffusion to the Si substrate limits the surface temperature excursion time to < 0.1 μ s. The Ge atoms move just $\sim 1.6 \times 10^{-11}$ cm in 0.1 μ s at 250 °C, which is clearly too small to affect the nucleation and growth mechanism.

Therefore, thermal effects can be excluded and the observed increase in surface diffusion is electronic in nature.

It is well known that an electron or a photon interacting with the surface can induce an electronic excitation causing emission of ions or neutral particles. We can rule out the Knotek-Feibelman (KF) mechanism since KF requires photons with energies of tens of eV [164]. The Menzel-Gomer and Redhead (MGR) model can also be ruled out since excitons on Si and Ge surfaces are not self-trapped and the applied photon energy is relatively low [183].

Sumi proposed a two-hole localization (THL) model and applied it successfully to explain electronically induced bond rupture at Si and other surfaces [185]. The primary assumption in THL is that surface bond rupture leading to neutral-atomic desorption can be induced by strong lattice relaxations associated with localization of two valence holes on the same surface bond. The localization of the second hole causes strong vibrations of the surface atom, which could lead to bond breaking. These atoms could be ejected due to this transient strong lattice vibration (phonon kick) with a distribution of translational energies that starts from a given onset [19]. Vibrational relaxation after electronic excitation would lead to many phonons being emitted. The lattice forms a continuum of motions that can absorb the energy of the vibrational relaxation. As the energy of the surface atoms increases, the bonded atoms vibrate more strongly. If the phonon kick perpendicular to the surface imparted to a surface atom is not sufficient to cause desorption, the enhanced vibrational motion could lead to increased surface diffusions.

A possible scenario involves electron-hole generation in the substrate followed by hole diffusion to the surface and two-hole localization [185]. Yu and Tanimura

investigated the laser-induced desorption of Si adatoms on Si(100)-(2x1) when the surface is excited by 2.48 eV laser pulses [188]. Their results show that electronic excitation causes desorption of Si atoms from a certain adatom configuration. The desorption yield was super-linearly dependent on the laser fluence and, therefore, was consistent with the two-hole localization model. Desorption yields with successive laser pulses indicated that the adatom configuration that was reactive to desorption transformed by laser excitation into a different form that is less susceptible to desorption. The results show that free holes are more effectively trapped at surface-defect sites. This suggests that substrate excitation during deposition causes hole localization preferentially at adatom sites.

Once the Ge wetting layer is formed, two-hole localization can occur on the Ge surface. At 250 °C, the indirect Ge energy band gap is 0.57 eV and Ge has a direct band gap at 0.7 eV. The absorption coefficient of 1064 nm in Ge is $1.6 \times 10^4 \text{ cm}^{-1}$, leading to significantly higher electron-hole generation in the Ge wetting layer than the Si substrate. The hole density in Ge due to absorption of the laser pulse is $\sim 10^{23} \text{ cm}^{-3}$. The surface hole density depends on many parameters that include surface recombination and diffusion across the Si/Ge interface. We are not aware of any study done on electronic bond breaking on electronically excited Ge surfaces. However, the two-hole localization mechanism, followed by the phonon-kick, is applicable to semiconductors in general. Energetically, this mechanism could be effective on Ge surfaces. For surface bond breaking, the phonon-kick has to transfer enough energy to the top atom along the bond direction to break that bond. If that energy transfer is not sufficient for bond breaking, then the atom will have a vibrational excitation that can lead to surface hopping.

Therefore, THL on the Ge surface can lead to selective energy transfer to the Ge adatoms since these atoms constitute a defect site. The energy that is preferentially given to these adsorbed atoms can result in their hopping to settle epitaxially on the surface. Measurement of Ge film thickness for different excitation laser energy densities showed the Ge coverage is not affected by the excitation laser; thus, we conclude that atom desorption by electronic excitation is too small for the studied conditions.

In our previous picoseconds time-resolved RHEED studies of excitation of the three low-index surfaces of Ge with 1064 nm, 100 ps laser pulses have conclusively shown that the surface temperature behaves as expected from a simple heat diffusion model [80, 105, 197]. This observation rules out an electronic mechanism that transfers energy to surface atoms causing heating above that expected from simple laser absorption in the skin depth followed by heat diffusion. However, we point out that RHEED probes surface atoms over a very large area. The mechanism we are proposing for enhanced surface diffusion of the adsorbed Ge atoms is preferential to the adatoms, which has only a very small coverage. Therefore, such preferential enhancement of surface hopping of the adatoms would not be sufficient to allow it to be detected through RHEED observation of the transient Debye-Waller factor. Time-resolved RHEED experiments with shorter time resolution, performed by Zewail *et al.*, have shown that electronic excitation of semiconductor surfaces results in surface contraction followed by expansion [220]. The initial structural changes (tens of ps) are due to nonthermal distortion of the binding forces due to electron-hole generation. These effects are dissipated in few tens of ps and the surface then shows expansion as expected [220]. Since the surface growth processes is too slow compared to the detected bond softening time, we do not anticipate

that such bond softening is directly involved in the observed nonthermal effects on QD growth. Dynamic transmission electron microscopy (TEM) has been recently developed and used to image transient structures in thin films with 15-ns temporal resolution [221-223]. An extension of this technique to develop a dynamic reflection electron microscope (REM) [94] could allow the real-time observation of the growth of the quantum dots and resolve how growth dynamics is affected by electronic excitation.

VI. 4. CONCLUSION

We have studied the surface diffusion coefficient of Ge during pulsed laser deposition of Ge on Si(100)-(2x1) with different excitation laser energy densities. Applying the excitation laser to the substrate during the growth increases the surface diffusion coefficient, changes the QD morphology and density, and improves the size uniformity of the grown quantum dots. We have ruled out thermal effects. A purely electronic mechanism of enhanced surface diffusion of Ge is proposed. The nature of this nonthermal mechanism could be due to two-hole localization followed by a phonon kick of the adsorbate. In order to determine the range of conditions for which electronic excitation is effective in low-temperature growth of epitaxial thin films and enhancing surface diffusion and understand the mechanism involved, future work will need to investigate the effect of the excitation wavelength and that of doping. The excitation wavelength is known to strongly affect bond rupture at surfaces. For Si, bond rupture rate by 460 nm was found to be ~ 100 times more than that for 1064 nm at the same fluence [184]. The bond rupture was resonantly enhanced at excitation photon energy of 2 eV [20]. However, the morphology of vacancy formation was the same regardless of the

laser wavelength, which suggested that a similar mechanism of bond rupture was involved.

While the growth of total number density is about the same for n-type and p-type surfaces, the total vacancy-site densities produced on n-type surfaces were significantly more than for p-type surfaces. The bond rupture at sites nearest pre-existing vacancies was significantly enhanced for n-type surfaces [184]. Excited species generated in the bulk must localize at the surface to affect thin film growth. The transport process of carriers and its surface localization is strongly dependent on band bending. By performing experiments to compare excitation effects on n-type and p-type materials, band bending effects can be clarified.

Observation of surface diffusion at submonolayer coverage by atom tracking in a scanning tunneling microscope (STM) can be particularly important because this can provide an atomic view of how adsorbate motion is affected by electronic excitation [224, 225]. STM during growth can provide series of images at regular scanning speed that are generally enough to get information about atom hopping and morphology evolution. The STM studies can also allow to observe any surface defect generation and any changes in adsorption sites due to electronic excitation. These studies can be used to develop a better picture of the mechanism involved in electronically enhanced surface diffusion.

CHAPTER VII
LOW TEMPERATURE EPITAXIAL GROWTH OF Ge QUANTUM DOT ON
Si(100)-(2X1) BY FEMTOSECOND LASER EXCITATION

VII. 1. INTRODUCTION

Growth of Ge on Si is a classical model of the Stranski-Krastanov growth-mode, also known as layer-plus island, where growth starts in a uniform layer-by-layer up to ~ 3 monolayers (ML). In Ge on Si growth, one way to suppress misfit dislocations is by lowering the substrate temperature [12]. To lower the epitaxial growth temperature, extrinsic assistance by energetic particles, such as ions, electrons and photons, have been used to promote the migration of adsorbed atoms at the surface [33]. Pulsed laser induced electronic processes leading to surface structural modifications have been shown to occur when the laser intensity is significantly below the melt threshold [17, 19, 158]. We have recently studied the effects of nanosecond pulsed laser-induced electronic excitations on the self-assembly of Ge QD on vicinal Si(100)-(2x1) grown by pulsed laser deposition [33, 165]. Electronic excitations, due to laser irradiation of the Si substrate and the Ge film during growth, were shown to decrease the roughness of films grown at room temperature and ~ 120 °C. At this temperature, the grown films were nonepitaxial. Electronic excitation resulted in the formation of an epitaxial wetting layer and crystalline Ge QD at ~ 260 °C, a temperature at which no crystalline QD formed without excitation under the same deposition conditions [33, 165].

VII. 2. EXPERIMENT

Ge quantum dots on Si(100) were grown in an ultrahigh vacuum (UHV) chamber (base pressure $\sim 7.0 \times 10^{-10}$ Torr) by femtosecond pulsed laser deposition. The Si(100)

substrates (dimensions of 2.0 mm x 10 mm x 0.5 mm *p*-type boron doped, and resistivity 0.060-0.075 Ω -cm, miscut angle 0.38°) were chemically etched by using a modified Shiraki method before being loaded into the UHV chamber [33]. The Ge target was a 2" disk, 0.5 mm thick, undoped *n*-type, with a resistivity of 45-58.7 Ω -cm. The vacuum system was then pumped down, baked at 150 °C for at least 24 h, and sample was degassed overnight at ~650 °C and then flashed to 1200 °C for ~60 s by direct heating to remove native oxides and carbon and to form (2x1) reconstructed surface. The target was rotated at 5 revolutions per minute to reduce the particulates formation. The surface temperature was initially measured using a combination of a Type K (chromel-alumel) thermocouple mechanically attached to the substrate surface and a pyrometer. The deposition was carried out with a chirped pulse amplified Ti:sapphire laser. Output pulse has ~60 femtosecond pulse width with center wavelength ~800 nm operating at 1 kHz repetition rate. The femtosecond laser was split into ablation and excitation beams of nonequal powers by means of half-wave plate and a thin film polarization beam splitter. The p-polarized ablation beam was focused on the rotating Ge target, resulting in a laser energy density of ~0.2 J/cm². The s-polarized excitation passed through another half-wave plate, used to change its polarization, and then was directed onto substrate. This laser was used to excite the substrate during deposition with an energy density of ~30 mJ/cm². A well-collimated 20-keV electron beam with a spot size <90 μ m diameter was used to probe the growth dynamics. A phosphor screen displayed the electron diffraction pattern which was recorded by a charge-coupled device (CCD) camera. Sample-to-target distance was ~10 cm. The final film thickness measurement was done by a spectroscopic ellipsometer.

VII. 3. RESULTS

To study the effect of using excitation laser, a series of Ge samples was prepared at different substrate temperatures. The film growth was accomplished with and without the excitation laser, but otherwise, under the same conditions.

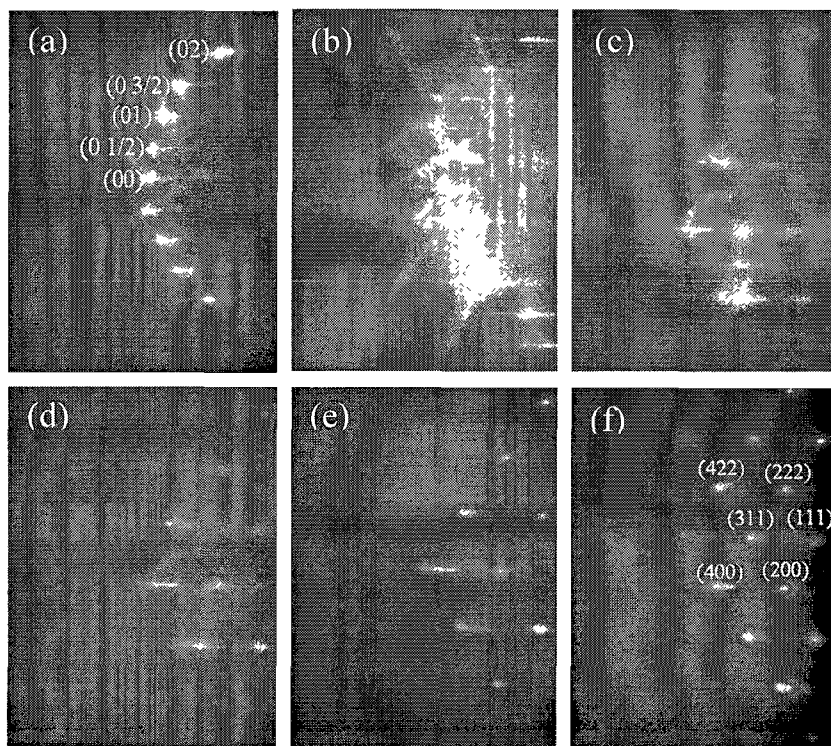


FIG. 25. RHEED patterns during Ge deposition on Si(100)-(2x1) at ~ 70 °C with excitation laser of ~ 30 mJ/cm².

We have first deposited Ge on Si(100)-(2x1) with the excitation laser and constantly decreased the substrate temperature until the point where the RHEED diffraction spots decayed completely with coverage.

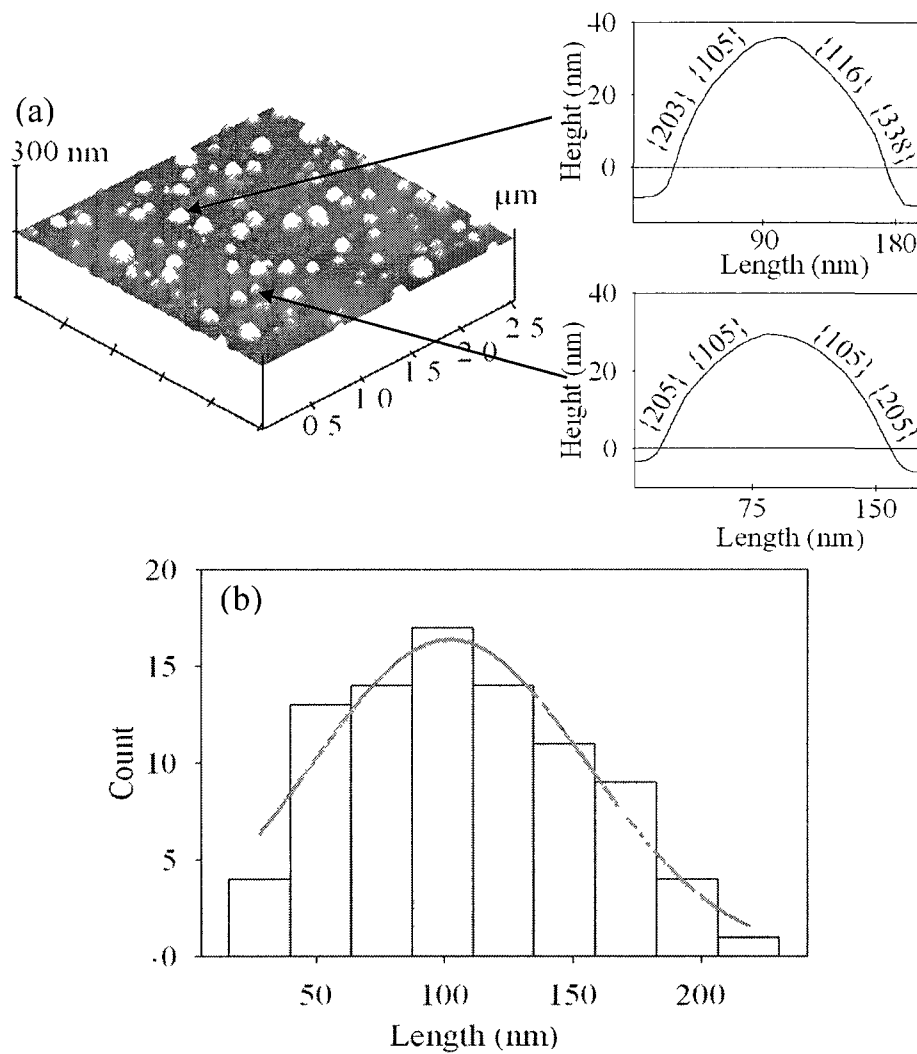


FIG. 26. (a) AFM image and line scans of two islands, and (b) its corresponding Ge quantum dot size distribution for film grown at 70 °C with excitation.

Figure 25(a) shows the reconstructed Si(100)-(2x1) surface, consisting of spots aligned on Laue circles. Upon initiating growth with the substrate temperature at 70 °C, the intensity of the RHEED spots drops immediately due to formation of many small two-dimensional islands and the pattern indicates that the growth starts epitaxially, as shown in Fig. 25(b). At ~4 ML coverage, the intensity of the diffraction spots starts to

decrease and an elongated transmission pattern evolves with further Ge growth, corresponding to formation of hut clusters, as shown in Fig. 25(c).

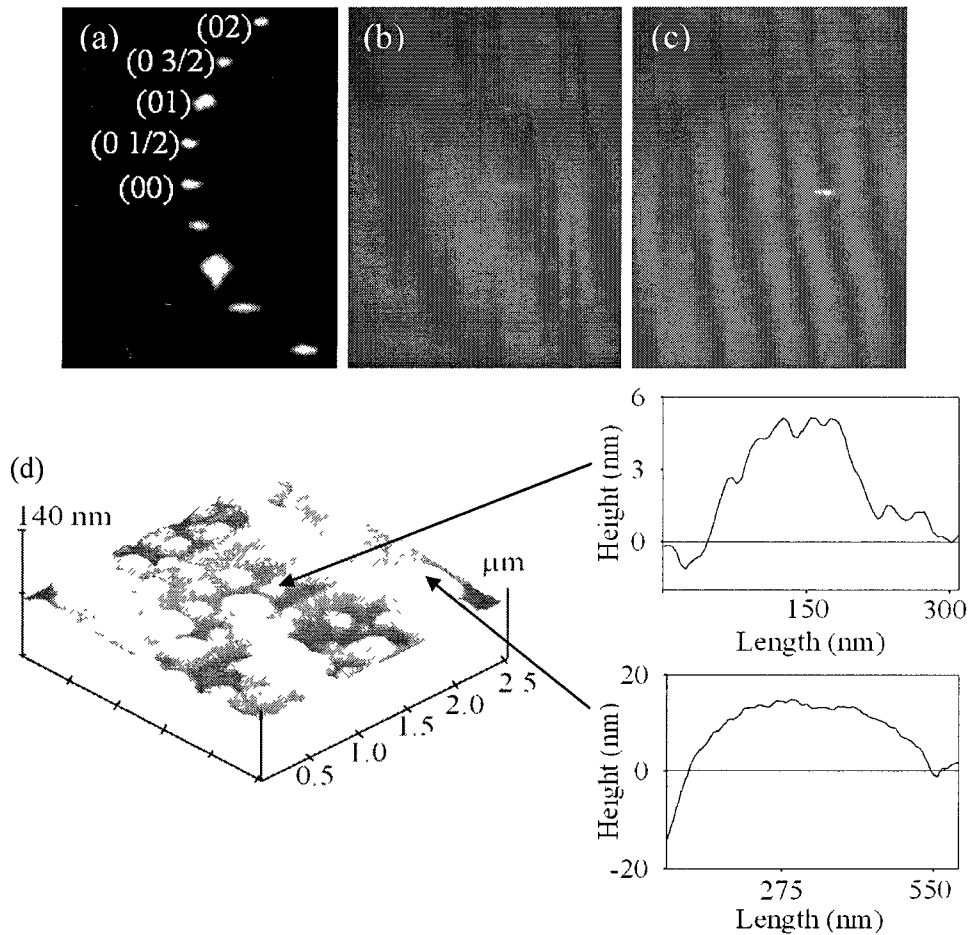


FIG. 27. RHEED pattern and AFM image of Ge quantum dots on Si(100)-(2x1) grown at 70 °C without the excitation laser. (a) Clean Si(100)-2x1 surface (b) after ~7 ML, (c) after ~12 ML, and (d) topographic AFM image and line scans of two clusters.

With further coverage, the elongation decreases and round transmission spots start to form at ~6 ML coverage, shown in Fig. 25(d). Those elongated streaks became shorter,

shown in Fig. 25(e), due to transformation of huts into domes at ~ 8 ML coverage. The deposition was stopped at ~ 12 ML coverage. The RHEED pattern at that coverage, shown in Fig. 25(f), obtained ~ 12 ML, shows well-defined spotty transmission pattern indicative epitaxial QD growth.

These spots are not falling on Laue circles and result from transmission of electrons through faceted islands. The AFM image in Fig. 26(a) shows islands with different sizes. Most of the islands are dome shaped with well-defined facets. Line scans of two islands, taken along their major axes, are shown in Fig. 26(a).

The facets were identified by the angle they make with $\{100\}$ plane. The average height for this AFM image is ~ 30 nm and island density is $\sim 1.5 \times 10^9$ cm $^{-2}$. Size distribution graph, shown in Fig. 26(b), indicated that the average QD length is ~ 110 nm while the most expected size is ~ 100 nm. For fs-PLD of Ge on Si(100)-(2x1) at 70 °C without laser excitation, some of the diffraction spots became dim after ~ 7 ML coverage, and almost no pattern appeared after 12 ML, indicating loss of long-range order on the surface as shown in Fig. 27. At this low temperature, formation of a rough disordered surface is expected due low surface diffusion coefficient. The AFM image in Fig 27(d) shows a collection of nonuniform clusters as generally expected for low temperature heteroepitaxial growth. Line scans of two clusters show irregular shape with no defined facets. For deposition at a substrate temperature of 150 °C, while applying the same excitation laser energy density, AFM observations showed decrease in island density and increase in average QD size and height compared to that at 70 °C. The same trend was observed as the substrate temperature is further increased to 280 °C.

VII. 4. DISCUSSION

When the Si sample is irradiated by the 800 nm (1.55 eV) femtosecond laser, the initial effect is to generate electron-hole pairs with excess energies of no more than 0.43 eV. The energy density of the fs laser pulses used in the present work is well below the damage threshold of Si, which is ~ 200 mJ/cm² [226]. Thermal effects can be readily ruled out by the fact that the used energy densities are almost an order of magnitude lower than that for ablation and, more importantly, is that the temperature excursion occurs only in a subnanosecond time scale due to heat diffusion to the bulk. Since the surface processes affecting growth occur at a much slower time scale, thermal effects of the laser irradiating the substrate are negligible. Also, the temperature build-up on the surface due to the repetitive nature of excitation is too small to cause any measurable effect on Si growth. We have used a spectroscopic ellipsometer to measure Ge film coverage with and without laser excitation for all other deposition conditions kept the same. For samples, without laser excitation at 70 °C, the Ge thickness was 16.7 ± 1.0 Å, while with excitation the Ge thickness it was 17.4 ± 0.5 Å. Therefore, within the experimental error, there appears to be no effect on Ge film thickness due to the excitation laser, and any atom desorption by electronic excitation is too small to affect the grown film.

The interaction of electrons or photons with semiconductor surfaces can cause emission of ions or neutrals due to electronic excitation leading to surface bond breaking [21]. A two-hole localization (THL) model was proposed for this mechanism [185]. The primary assumption in the THL model is that surface bond rupture leading to neutral-atom desorption can be induced by strong lattice relaxations associated with localization

of two valence holes on the same surface bond [187]. The localization of the second hole causes strong vibrations of the surface atom, which could lead to bond breaking. Due to this transient strong lattice vibration (phonon kick), these atoms could be ejected with a distribution of translational energies that starts from a given threshold [19]. Vibrational relaxation after electronic excitation would lead to emission of many phonons. As the energy of the surface atoms increases, the bonded atoms vibrate more strongly. If the phonon kick perpendicular to the surface imparted to a surface atom is not sufficient to cause desorption, the enhanced vibrational motion could lead to increased surface diffusion. In fs PLD, plume pulse width is on the order of microseconds, similar to ns PLD [227]. The longest lifetime of holes in n-type germanium at 300 K is longer than 1 ms. Therefore the holes generated by the excitation pulse are present during the nucleation and growth processes.

The THL mechanism followed by the phonon-kick could occur on semiconductor surfaces, in general. For surface bond breaking, the phonon-kick has to transfer enough energy to the top atom along the bond direction to break that bond. If that energy transfer is not sufficient for bond breaking, then, the atom will have a vibrational excitation that can lead to increased surface diffusion. The process of THL was found to preferentially occur on surface defect sites [188]. THL on the Ge surface can lead to selective energy transfer to the Ge atoms that landed on the surface from the ablation plume since these atoms constitute a surface defect site. The energy that is preferentially given to these adsorbed atoms can result in their hopping to settle epitaxially on the surface.

VII. 5. CONCLUSION

In summary, epitaxial Ge QDs was grown on Si(100)-(2x1) by fs pulsed laser excitation during growth. The growth was studied by *in-situ* RHEED and *ex-situ* AFM. The results show that excitation laser reduces the epitaxial growth temperature to ~ 70 °C. This result could lead to nonthermal method to achieve low temperature epitaxy which limits the redistribution of impurities, reduces intermixing in heteroepitaxy, and restricts the generation of defects by thermal stress.

CHAPTER VIII

THE PULSED LASER ASSISTED GROWTH OF Ge QUANTUM DOT ON Si(100)-2X1: A STM STUDY

VIII.1 INTRODUCTION

Self-assembled Ge quantum dots (QDs) grown on Si are suitable for applications in nanoelectronics and optoelectronic devices [2, 33, 157]. In order to fully use their potential in various applications, the size distribution of QDs must be well controlled.

The growth of Ge on Si follows the Stranski-Krastanov mode, also known as layer-plus-islands growth, which is observed when lattice mismatch is between 3-7% [217]. The initial several monolayers (1 ML $\sim 6.2 \times 10^{14}$ atoms/cm²) grow in a layer-by-layer fashion on the substrate. Upon completion of the wetting layer, the film undergoes three-dimensional islands growth to relieve lattice strain. Those islands could be dislocation free, while some larger ones develop misfit dislocations to reduce their strain energy [228]. The first faceted islands, in the shape of square-based pyramids or rectangular-based hut clusters with four facets, appear following completion of the wetting layer. Those huts are rectangular-shaped $\{105\}$ -faceted clusters with a contact angle $\sim 11^\circ$ with $\{100\}$ planes, whereas at higher temperatures another kind of multifaceted, larger dome-shape islands coexist with huts [4, 5]. While hut clusters are $\{105\}$ -faceted and have a 15-20 nm average size, the dome islands are mainly bound by steeper facets such as $\{113\}$, $\{102\}$ making $\sim 25^\circ$ and 26° , respectively, with the substrate, and have an average size of 50-100 nm [6, 7]. The evolution of the $\{105\}$ -faceted hut clusters to $\{105\}$ -, $\{113\}$ -, and $\{15\ 3\ 23\}$ -faceted domes is well documented along with the final, larger $\{111\}$ -faceted superdomes containing dislocations [7]. It was shown that the $\{105\}$ facet

is energetically favorable on smaller islands, while the $\{113\}$ facet is favorable on larger islands [8]. The shape of the initial islands was found to depend on the deposition technique. For example, if Sb is used as a surfactant in the molecular beam epitaxy (MBE) of Ge/Si(100), the initial island shape changes from $\{105\}$ -faceted to $\{117\}$ -faceted [9]. If Ge is grown by liquid phase epitaxy (LPE), $\{115\}$ -faceted islands are first observed instead of the $\{105\}$ -faceted ones, and as the coverage increases, $\{111\}$ -faceted pyramids are formed [10, 11].

The morphological evolution of islands is also dependent on growth conditions. For example, as the substrate temperature is increased, the Ge adatoms diffuse more over the surface which increases the probability of these adatoms finding energetically suitable sites for epitaxial growth. Generally, increasing the substrate temperature above that needed for epitaxial growth causes an increase in island size and height, a decrease in the number of islands, and their shape transition from hut to dome [33, 165, 229].

Pulsed laser induced electronic processes leading to surface structural modifications have been shown to occur when the laser intensity is below the melt threshold [17-19, 158]. Recent scanning tunneling microscopy (STM) studies have demonstrated that laser pulses well below the melt and ablation thresholds induce bond rupture at individual atomic sites on several semiconductor surfaces via a process that is purely electronic [20-22]. The laser-induced electronic bond rupture causes structural changes on the surface which depend strongly on the surface studied.

Low temperature thin film growth is strongly desirable in microelectronic fabrication. In Si/Ge, it has been long recognized that one way to suppress misfit dislocations is by lowering the growth temperature [12]. To lower the epitaxial growth

temperature, extrinsic assistance by energetic particles, such as ions, electrons and photons, have been used to add energy to promote the migration of adsorbed atoms at the surface [13-15].

Treatment of silicon surfaces by a Nd-doped yttrium aluminum garnet (Nd:YAG) laser was used to improve surface wettability and adhesion characteristics [16]. Also, illumination of silica substrates with a very low intensity diode laser during deposition was reported to unify the clusters' shapes and narrow the size distribution of Ga nanoparticles grown at ~ 100 °C [159]. Moreover, irradiation by a few hundred eV electron beam during deposition of CeO₂ on Si was reported to enhance surface epitaxy by reducing the required temperature for epitaxial growth from 820 °C to 710 °C [13]. In another work, a low-energy electron beam was used to modify the surface and achieve high quality GaAs film grown on an insulator on silicon [15]. Pulsed ion-beam irradiation during heteroepitaxy of Ge on Si led to modifying the average size and size distribution of Ge islands grown by molecular beam epitaxy (MBE) [160]. Post-deposition nanosecond pulsed laser treatment of Ge quantum dots (QD) grown on Si reduced the QD surface density, modified their composition, and increased their average size, making the QD size more uniform after the treatment [161]. Nonthermal laser induced desorption has also been widely studied for different metals and semiconductors [162-164].

We have recently studied the effects of nanosecond pulsed laser-induced electronic excitations on the self-assembly of Ge QD on Si(100)-(2x1) grown by pulsed laser-deposition [165]. Electronic excitations, due to laser irradiation of the Si substrate and the Ge film during growth, were shown to decrease the roughness of films grown at a substrate temperature of ~ 120 °C. At this temperature, the grown films showed no long

range order as detected by RHEED. Electronic excitation resulted in the formation of an epitaxial wetting layer and crystalline Ge QD at ~ 260 °C, a temperature at which no crystalline QD formed without excitation under the same deposition conditions. Here we expand the scope of this work by studying excitation effect on deposition at various substrate temperatures and excitation with different laser energy densities. The effect of applying the excitation laser on the growth morphology is studied. It is shown that the excitation laser affects the morphology only when applied during growth. The results are consistent with an electronically driven mechanism that increases surface diffusion of the incoming Ge flux.

VIII.2. EXPERIMENT

Ge quantum dots were grown in an ultrahigh vacuum (UHV) chamber ($\sim 7 \times 10^{-11}$ Torr) by pulsed laser deposition (PLD) equipped with STM. The Ge target was mounted on a rotation stage with a variable rotation speed. Target rotation at 5 rpm was used to minimize the particulate formation during deposition. The laser beam profile on target and target rotation speed were set such that the spatial separation of the laser pulse spots on target were ~ 0.6 of its full width at half-maximum (FWHM), resulting in ablation of the target surface by no more than two laser pulses. The Si(100) substrates (dimensions of 1.0 mm x 10 mm x 0.5 mm *p*-type boron doped, and resistivity 0.060-0.075 Ω -cm, miscut angle 0.38°) were chemically etched by using a modified Shiraki method before being loaded into the UHV chamber. The Ge target was a 2" disk, 0.5 mm thick, undoped *n*-type, with a resistivity of 45-58.7 Ω -cm. The vacuum system was then pumped down, baked more than 24 hours and, finally, cooled down to room temperature. The Si(100) sample was degassed at ~ 700 °C for another 24 hours and then flashed to ~ 1200 °C for

~60 s to obtain the (2x1) reconstruction. The substrates were heated by direct current flow. The surface temperature was measured using a Mikron MI-GA15 pyrometer.

A Q-switched Nd:YAG (wavelength $\lambda = 1064$ nm, full width at half maximum (FWHM) of ~40 ns, 10-Hz repetition rate) was split into an ablation beam and an excitation beam of nonequal powers by means of a half wave-plate and a thin film polarizing beam splitter. The *p*-polarized ablation beam was focused on the rotating Ge target to a spot size ~400 μm (measured at 1/e of the peak value), resulting in a laser energy density of ~8 J/cm². The *s*-polarized excitation beam was left unfocused with a beam diameter of ~6.0 mm (measured at 1/e peak value) and was used to irradiate the sample surface. Both the ablation and the excitation laser beams were incident on the Ge target and Si substrate at 45°.

VIII.3. RESULTS AND DISCUSSIONS

VIII.3.1. RESULTS

We have started deposition on a clean Si(100)-2x1. Figure 28 shows clean reconstructed Si(100)-2x1 surface with 40x40 nm² area.

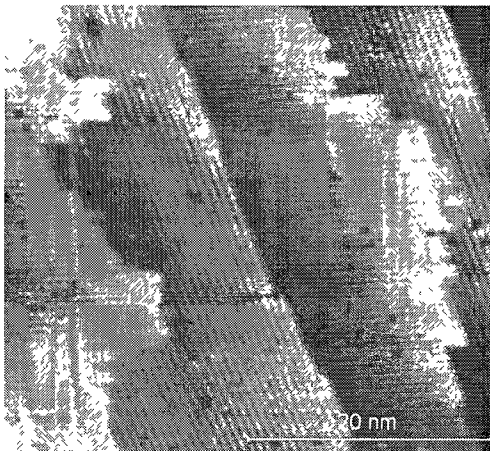


FIG. 28. Clean Si(100)-2x1 surface with 40x40 nm² area.

This large-scale STM image of the Si (100) reveals a rich plethora of defects and fine structures: two kinds of steps and various kinds of defects. These local structures play an important role in semiconductor processing. Clean Si (100)-2x1 showing a step that has a mixed S_A (smooth) and S_B (ragged) character showing the dimmer rows of upper and lower terrace and has dimers rotated 90° at steps.

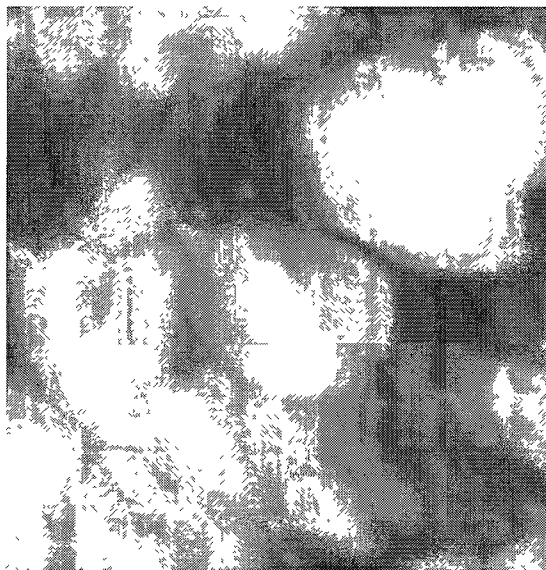


FIG. 29. Two-dimensional STM image with $500 \times 500 \text{ nm}^2$ area obtained at 250°C .

From our previous results, we know that epitaxial growth is not possible at $\sim 250^\circ \text{C}$ if there is no external assistance. Figure 29 shows two-dimensional STM picture ($500 \times 500 \text{ nm}^2$) of Ge growth on silicon surface at 250°C . The results shows that 3D structures collectively lack long range order and image contains some arbitrary shape islands, as shown in Fig. 30. We then started applying excitation laser during growth. 75 mJ/cm^2 excitation laser energy density was first used. Growth formation was studied at different germanium coverages. At 2 ML, it was observed that germanium particles

gather together on steps, shown in Fig. 30(a). As coverage was increased to ~ 4 ML, three-dimensional islands started to appear, Fig. 30(b). At this coverage, main faceting of islands is $\{105\}$ with Si(100) plane. Figure 30(c) shows those pyramidal shaped-islands along with square-based islands at 5 ML. They are all $\{105\}$ -faceted. When germanium coverage reaches to ~ 6 ML, average islands size increases while maintain the same morphology. Island density is on the order of 10^{10} islands/cm².

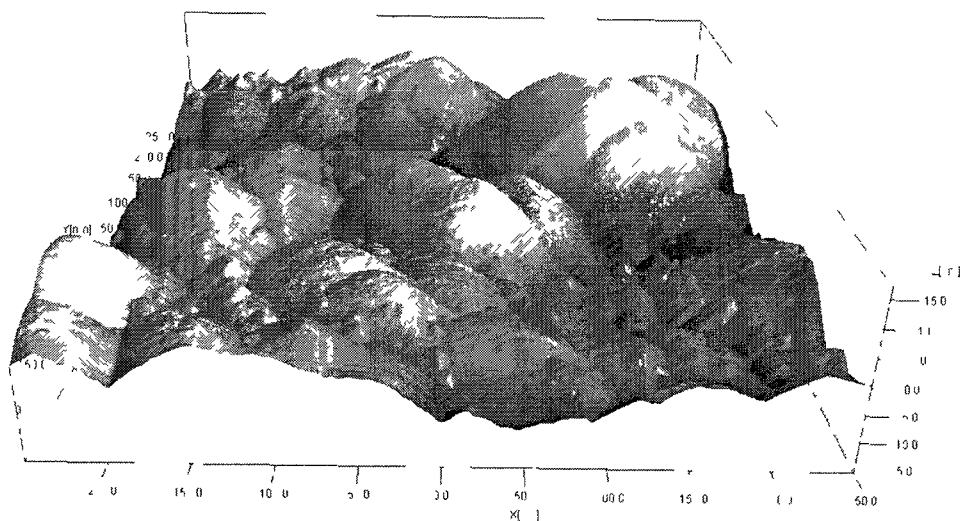


FIG. 30. Three-dimensional STM image with 500×500 nm² area obtained at 250 °C.

Different excitation laser energy density was applied to study the effect on morphology and epitaxial growth temperature. Figure 31 shows the result of ~ 6 ML germanium deposition at different excitation energy densities. Figure 31(a) shows the results when 25 mJ/cm² used. When this value increased to 50 mJ/cm², it was observed that average islands size gets bigger while island density decreased as shown in Fig.

31(b). This trend continues when laser energy density was increased to 75 mJ/cm^2 . Finally, when 100 mJ/cm^2 used, islands size become larger compared to other films. It is obvious that when small laser energy density was used most of the islands consist of pyramidal-shaped islands along with fraction of square based island. However, as the excitation values increases, we see that size distribution become more uniform.

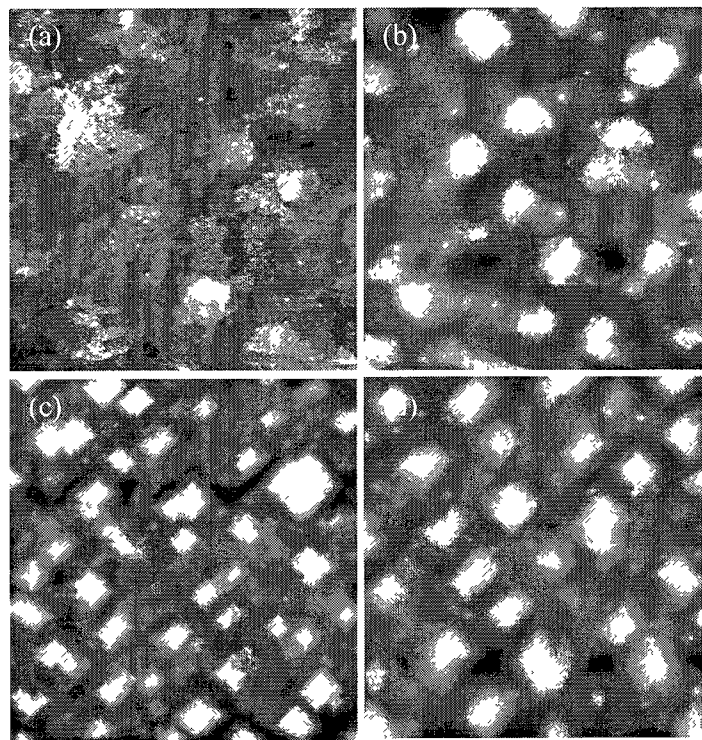


FIG. 31. Ge coverage on Si(100) at (a) 2 ML, (b) 4 ML, (c) 5 ML, and (d) 6 ML when 75.5 mJ/cm^2 excitation laser energy density was used.

Figure 32 shows individual characteristic islands at different coverages. Although morphology of final films changes due to excitation laser, faceting of the individual islands hasn't change. They are mainly $\{105\}$ -faceted islands with different shapes and sizes. When 25 mJ/cm^2 is used after ~ 6 ML germanium deposition, we generally

observed small size square based $\{105\}$ faceted islands, while at larger laser energy densities, rectangular based islands also appeared with same facetations. When 100 mJ/cm^2 is used, facetations basically remained same while size and height increases.

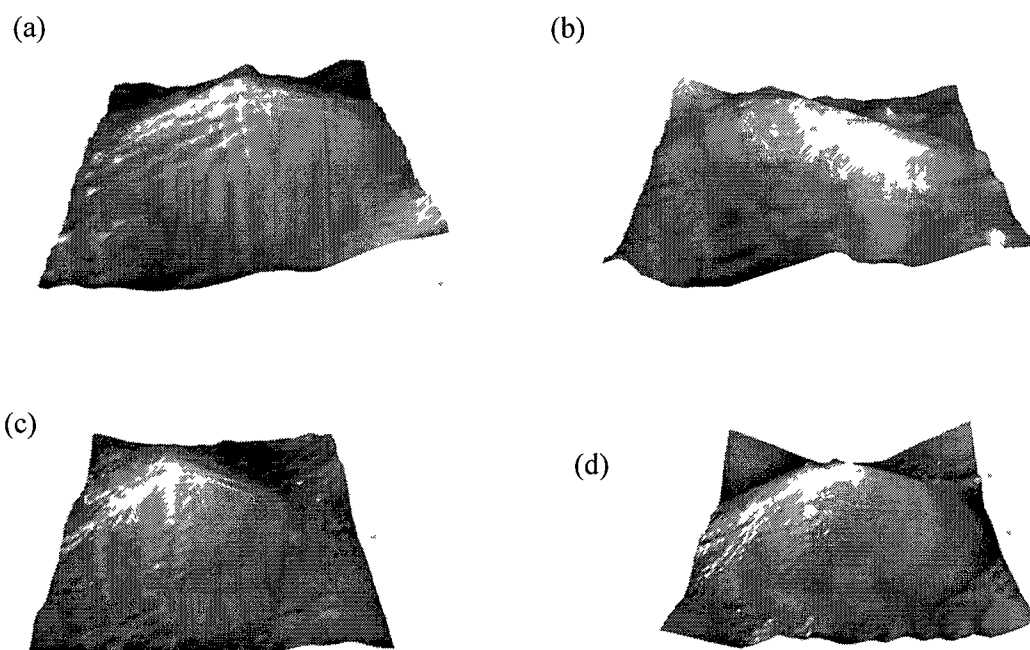


FIG. 32. Individual islands when (a) 25 mJ/cm^2 , (b) 50 mJ/cm^2 , (c) 75 mJ/cm^2 , and 100 mJ/cm^2 is used.

VIII.3.2. DISCUSSIONS

The results show that irradiation of the substrate by the excitation laser has an effect on Ge growth similar to that observed when the substrate temperature is raised. Basically, there appears to be a mechanism driven by the excitation laser that results in enhanced Ge adatom surface diffusion.

When the sample is irradiated by the pulsed laser, the initial effect is to generate electron-hole pairs. The bulk silicon is known to have an indirect bandgap of 1.12 eV. The primary effect of the 1064 nm nanosecond laser light on the Si substrate is bulk-valence excitation to generate holes and electrons with small excess energies [172]. The energy density of the ns laser pulses used is well below the melt threshold of Si [173].

The surface temperature rise due to laser heating is calculated using a one-dimensional, heat-diffusion model. According to this model, the maximum temperature rise due to absorption of the 1064 nm excitation laser in the skin depth of Si ($\sim 60 \mu\text{m}$) is $\sim 23 \text{ }^\circ\text{C}$. The surface temperature drops to the substrate temperature by heat diffusion in $\sim 0.1 \mu\text{s}$. For Ge, the skin depth for 1064 nm is 200 nm, and the maximum temperature rise in this case is $\sim 200 \text{ }^\circ\text{C}$ if irradiated with $106 \pm 10 \text{ mJ/cm}^2$, which is the maximum laser energy density used during the present work. Heat diffusion to the Si substrate limits the temperature excursion time to $< 0.1 \mu\text{s}$. The macroscopic diffusion of Ge atoms adsorbed on the Si(100)-(2x1) surface has been shown to follow the Arrhenius behavior [174]: $D = D_0 \exp[-E_T/kT]$, where $D_0 = 11 \times 10^{-4} \text{ cm}^2/\text{s}$ is a pre-exponential constant, $E_T = 1.17 \text{ eV}$ is the activation energy, and k and T are the Boltzmann's constant and temperature, respectively. The Ge atoms move just $\sim 1.6 \times 10^{-11} \text{ cm}$ in 100 ns at $250 \text{ }^\circ\text{C}$, which is clearly too small to affect the nucleation and growth mechanism. Therefore, we can exclude laser heating as a possible mechanism affecting Ge growth morphology due to the short temperature excursion time and small temperature rise.

Sumi proposed a two-hole localization (THL) model and applied it successfully to explain electronically induced bond rupture at Si and other surfaces [185]. The primary assumption in THL is that surface bond rupture leading to neutral-atomic desorption can

be induced by strong lattice relaxations associated with localization of two valence holes on the same surface bond. The localization of the second hole causes strong vibrations of the surface atom, which could lead to bond breaking. These atoms could be ejected due to this transient strong lattice vibration (phonon kick) with a distribution of translational energies that starts from a given onset [19]. Vibrational relaxation after electronic excitation would lead to many phonons being emitted. The lattice forms a continuum of motions that can absorb the energy of the vibrational relaxation. As the energy of the surface atoms increases, the bonded atoms vibrate more strongly. If the phonon kick perpendicular to the surface imparted to a surface atom is not sufficient to cause desorption, the enhanced vibrational motion could lead to increased surface diffusions.

A possible scenario involves electron-hole generation in the substrate followed by hole diffusion to the surface and two-hole localization [185]. Yu and Tanimura investigated the laser-induced desorption of Si adatoms on Si(100)-(2x1) when the surface is excited by 2.48 eV laser pulses [188]. Their results show that electronic excitation causes desorption of Si atoms from a certain adatom configuration. The desorption yield was super-linearly dependent on the laser fluence and, therefore, was consistent with the two-hole localization model. Desorption yields with successive laser pulses indicated that the adatom configuration that was reactive to desorption transformed by laser excitation into a different form that is less susceptible to desorption. The results show that free holes are more effectively trapped at surface-defect sites. This suggests that substrate excitation during deposition causes hole localization preferentially at adatom sites.

Once the Ge wetting layer is formed, two-hole localization can occur on the Ge surface. At 250 °C, the indirect Ge energy band gap is 0.57 eV and Ge has a direct band gap at 0.7 eV. The absorption coefficient of 1064 nm in Ge is $1.6 \times 10^4 \text{ cm}^{-1}$, leading to significantly higher electron-hole generation in the Ge wetting layer than the Si substrate. The hole density in Ge due to absorption of the laser pulse is $\sim 10^{23} \text{ cm}^{-3}$. The surface hole density depends on many parameters that include surface recombination and diffusion across the Si/Ge interface. We are not aware of any study done on electronic bond breaking on electronically excited Ge surfaces. However, the two-hole localization mechanism, followed by the phonon-kick, is applicable to semiconductors in general. Energetically, this mechanism could be effective on Ge surfaces. For surface bond breaking, the phonon-kick has to transfer enough energy to the top atom along the bond direction to break that bond. If that energy transfer is not sufficient for bond breaking, then the atom will have a vibrational excitation that can lead to surface hopping. Therefore, THL on the Ge surface can lead to selective energy transfer to the Ge adatoms since these atoms constitute a defect site. The energy that is preferentially given to these adsorbed atoms can result in their hopping to settle epitaxially on the surface. Measurement of Ge film thickness for different excitation laser energy densities showed the Ge coverage is not affected by the excitation laser; thus, we conclude that atom desorption by electronic excitation is too small for the studied conditions.

VIII.4. CONCLUSION

We have studied the effect of nanosecond pulsed laser excitation on the self-assembly of Ge quantum dots grown by pulsed laser deposition on Si(100)-(2x1) by STM. The morphology, growth temperature, and the facet behavior of Ge quantum dot were

studied at different excitation laser energy densities and different substrate temperature. The formation of {105}-faceted pyramids was observed right after the completion of the wetting layer. No effect on faceting was observed due to excitation laser energy. The electronic excitation during growth was found to improve the quantum dot crystalline quality, change their morphology, reduce epitaxial growth temperature, and decrease their size distribution. A purely electronic mechanism of enhanced surface diffusion of the Ge adatoms is proposed.

CHAPTER IX

CONCLUSIONS

IX.1. RHEED

We have studied Ge QD formation on Si(100)-(2x1) with different substrate temperatures and excitation laser energy densities. The excitation laser reduces the epitaxial growth temperature to 250 °C for a 22 ML film. In addition, applying the excitation laser to the substrate during the growth changes the QD morphology and density and improves the uniformity of quantum dots fabricated at 390 °C. At room temperature, applying the excitation laser during growth decreases the surface roughness although epitaxial growth could not be achieved. We have ruled out thermal effects and some of the desorption models. Although further studies are needed to elucidate the mechanism involved, a purely electronic mechanism of enhanced surface diffusion of Ge atoms is proposed. Further investigation of this electronic modification of thin film growth would benefit from surface diffusion measurement during growth and the use of *in situ* atomic probe microscopy to observe the development of the wetting layer and the quantum dots and how this is affected by electronic excitation.

Although the effects of electronic excitation on shown for Ge growth on Si(100), the basic principle involved is expected to apply to other semiconductor heteroepitaxy. Achieving low temperature epitaxial growth is an important step for high level integration. Low temperature epitaxy also limits the redistribution of impurities, reduces intermixing in heteroepitaxy, and restricts the generation of defects by thermal stress. The ability to prepare self-assembled quantum dots with reduced size distribution by electronic excitation is also important for many applications because both the optical and

electronic properties of a quantum dot depend on its size. The use of electronic excitation to provide some control on thin film and quantum dot growth could be an important tool in fabricating devices based on self-assembly.

We also have studied the surface diffusion coefficient of Ge during pulsed laser deposition of Ge on Si(100)-(2x1) with different excitation laser energy densities. Applying the excitation laser to the substrate during the growth increases the surface diffusion coefficient, changes the QD morphology and density, and improves the size uniformity of the grown quantum dots. We have ruled out thermal effects. A purely electronic mechanism of enhanced surface diffusion of Ge is proposed. The nature of this nonthermal mechanism could be due to two-hole localization followed by a phonon kick of the adsorbate. In order to determine the range of conditions for which electronic excitation is effective in low-temperature growth of epitaxial thin films and enhancing surface diffusion and understand the mechanism involved, future work will need to investigate the effect of the excitation wavelength and that of doping.

IX.2. STM

Lastly, we have studied the effect of nanosecond pulsed laser excitation on the self-assembly of Ge quantum dots grown by pulsed laser deposition on Si(100)-(2x1) by STM. The morphology, growth temperature, and the facet behavior of Ge quantum dot were studied at different excitation laser energy densities and different substrate temperature. The formation of {105}-faceted pyramids was observed right after the completion of the wetting layer. No effect on faceting was observed due to excitation laser energy. The electronic excitation during growth was found to improve the quantum dot crystalline quality, change their morphology, reduce epitaxial growth temperature, and decrease

their size distribution. A purely electronic mechanism of enhanced surface diffusion of the Ge adatoms is proposed.

BIBLIOGRAPHY

- [1] Wil McCarthy, *Hacking Matter: Levitating Chairs, Quantum Mirages, and the Infinite Weirdness of Programmable Atoms*, (Basic Books, New York, 2003).
- [2] K. L. Wang, C. Dongho, J. Liu, and C. Chen, Proceedings of the IEEE **95**, 1866 (2007).
- [3] B. A. Joyce, P. C. Kelires, A. G. Naumovets, D. D. Vvedensky, *Quantum Dots: Fundamentals, Applications, and Frontiers*, (Springer NATO Science Series, Dordrecht The Netherlands, 2005).
- [4] Y.-W. Mo, D. E. Savage, B. S. Swartzentruber, and M. G. Lagally, Phys. Rev. Lett. **65**, 1020 (1990).
- [5] M. Tomitori, K. Watanabe, M. Kobayashi, and O. Nishikawa, Appl. Surf. Sci. **76-77**, 322 (1994).
- [6] F. M. Ross, R. M. Tromp, and M. C. Reuter, Science **286**, 1931 (1999).
- [7] G. Medeiros-Ribeiro, A. M. Bratkovski, T. I. Kamins, D. A. A. Ohlberg, R. S. Williams, Science **279**, 353 (1998).
- [8] K. Brunner, Rep. Prog. Phys. **65**, 27 (2002).
- [9] M. Horn-von Hoegen, B. H. Müller, A. Al-Falou, and M. Henzler, Phys. Rev. Lett. **71**, 3170 (1993).
- [10] M. Schmidbauer, T. Wiebach, H. Raidt, M. Hanke, R. Köhler, and H. Wawra, Phys. Rev. B **58**, 10523 (1998).
- [11] W. Dorsch, S. Christiansen, M. Albrecht, P. O. Hansson, E. Bauser, and H. P. Strunk, Surf. Sci. **331-333**, 896 (1995).

- [12] J. C. Bean, T. T. Sheng, L. C. Feldman, A. T. Fiory, and R. T. Lynch, *Appl. Phys. Lett.* **44**, 102 (1984).
- [13] T. Inoue, Y. Yamamoto, and M. Satoh, *J. Vac. Sci. & Technol. A* **19**, 275 (2001).
- [14] W. Ensinger, *Nucl. Instrum. Methods Phys. Res. B.* **127/128**, 796 (1997).
- [15] A. Izumi, K. Tsutsui, and S. Furukawa, *J. Appl. Phys.* **75**, 2307 (1994).
- [16] D.-Y. Kim, K.-C. Lee, and C. Lee, *J. Korean Phys. Soc.* **44**, 341 (2004).
- [17] N. Itoh and A. M. Stoneham, *Materials Modification by Electronic Excitation*, (Cambridge University Press, Cambridge, 2001).
- [18] Y. Zhang, J. Lian, C. M. Wang, W. Jiang, R. C. Ewing, and W. J. Weber, *Phys. Rev. B* **72**, 094112 (2005).
- [19] J. Kanasaki, K. Iwata, and K. Tanimura, *Phys. Rev. Lett.* **82**, 644 (1999).
- [20] J. Kanasaki, T. Ishida, K. Ishikawa, and K. Tanimura, *Phys. Rev. Lett.* **80**, 4080 (1998).
- [21] E. Inami, K. Ishikawa, and K. Tanimura, *Surf. Sci.* **540**, L587 (2003).
- [22] J. Xu, S. H. Overbury, and J. F. Wendelken, *Phys. Rev. B* **53**, R4245 (1996).
- [23] J. Schubert, M. Siegert, M. Fardmanesh, W. Zander, M. Prömpers, C. Buchal, J. Lisoni, and C. H. Lei, *Appl. Surf. Sci.* **168**, 208 (2000).
- [24] C.-S. Kim, S. C. Song, and S. Y. Lee, *Appl. Surf. Sci.* **168**, 316 (2000).
- [25] P. Mele, K. Matsumoto, T. Horide, O. Miura, A. Ichinose, M. Mukaida, Y. Yoshida, and S. Horii, *Supercond. Sci. Technol.* **19**, 44 (2006).
- [26] P. Badica, K. Togano, S. Awaji, and K. Watanabe, *Supercond. Sci. Technol.* **19** 242 (2006).

- [27] A. Venimadhav, M. S. Hegde, R. Rawat, I. Das, and M. El Marssi, *J. Alloys and Comp.* **326**, 270 (2001).
- [28] J. -M. Liu, Q. Huang, J. Li, C. K. Ong, X. Y. Chen, Z. G. Liu, and Y. W. Du, *Mat. Lett.* **50**, 97 (2001).
- [29] J. Miao, H. Yang, W. Hao, J. Yuan, B. Xu, X. Q. Qiu, L. X. Cao, and B. R. Zhao, *J. Phys. D: Appl. Phys.* **38**, 5 (2005).
- [30] J. Ohta, H. Fujioka, H. Takahashi, M. Sumiya, and M. Oshima, *J. Cryst. Growth* **233**, 779 (2001).
- [31] D. O'Mahony, J. G. Lunney, G. Tobin, and E. McGlynn, *Solid State Electron.* **47**, 533 (2003).
- [32] C. M. Rouleau and D. H. Lowndes, *Appl. Surf. Sci.* **127-129**, 418 (1998).
- [33] A. O. Er and H. E. Elsayed-Ali, *J. Appl. Phys.* **108**, 034303 (2010).
- [34] A. O. Er and H. E. Elsayed-Ali, *J. Appl. Phys.* **109**, 084320 (2011).
- [35] M. S. Hegazy and H. E. Elsayed-Ali, *Appl. Phys. Lett.* **86**, 243104 (2005).
- [36] C. H. Hur, K. B. Han, K. A. Jeon and S. Y. Lee, *Thin Solid Films* **400**, 169 (2001).
- [37] L. Goux, M. Gervais, F. Gervais, C. Champeaux and A. Catherinot, *Int. J. Inorg. Mat.* **3**, 839 (2001).
- [38] I. B. Misirlioglu, A. L. Vasiliev, S. P. Alpay, M. Aindow, R. Ramesh, *J. Mater. Sci.* **41**, 697 (2006).
- [39] M. A. Khan, A. Garg, and A. J. Bell, *J. Phys.: Conference Series* **26**, 288 (2006).

- [40] M. S. Hegazy, T. F. Refaat, M. Nurul Abedin, H. E. Elsayed-Ali, *Opt. Eng.* **44**, 59702 (2005).
- [41] A. O. Er, W. Ren, and H. Elsayed-Ali, *Appl. Phys. Lett.* **98**, 013108 (2011).
- [42] B. Chrisey, G. K. Hubler, *Pulsed Laser Deposition of Thin Films*, (J. Wiley and Sons. Inc., New York, 1994).
- [43] R. Eason, *Pulsed Laser Deposition of Thin Films: Applications-Led growth of Functional Materials*, (J. Wiley and Sons. Inc., New Jersey, 2007).
- [44] H. M. Smith and A. F. Turner, *Appl. Opt.* **4**, 147 (1965).
- [45] V. Ruckenbauer, F. F. Hau, S. G. Lu, K. M. Yeung, C. L. Mak, and K. H. Wong, *Appl. Phys. A* **78**, 1049 (2004).
- [46] M. S. Hegazy and H. E. Elsayed-Ali, *Appl. Phys. Lett.* **86**, 243104 (2005).
- [47] M. Capitelli, A. Casavola, G. Colonna, and A. De Giacomo, *Spectrochim. Acta Part B* **59**, 271 (2004).
- [48] M. Frumar, B. Frumarova, P. Nemeč, T. Wagner, J. Jedelsky, and M. Hrdlicka, *J. Non-Cryst. Solids* **352**, 544 (2006).
- [49] S. Amoruso, R. Bruzzese, R. Velotta, and N. Spinelli, *J. Phys. B* **32**, R131 (1999).
- [50] P. Ohresser, J. Shen, J. Barthel, M. Zheng, Ch. V. Mohan, M. Klaua, and J. Kirschner, *Phys. Rev. B* **59**, 3696 (1999).
- [51] S. J. Barrington, T. Bhutta, D. P. Shepherd, and R. W. Eason, *Opt. Commun.* **185**, 145 (2000).
- [52] J. A. Venables, *Introduction to Surface and Thin Film Processes*, (Cambridge University Press, Cambridge, 2000).

- [53] D. L. Smith, *Thin-Film Deposition: Principles & Practice*, (McGraw-Hill, New York, 1995).
- [54] A. Cheenne, J. Perriere, F. Kerherve, G. Hauchecorne, E. Fogarassy, and C. Fuchs, *Mat. Res. Soc. Symp. Proc.* **191**, 229 (1990).
- [55] E. G. Gamaly, A. V. Rode, and B. Luther-Davies, *J. Appl. Phys.* **85**, 4213 (1999).
- [56] N. Itoh, J. Kanasaki, and J. Xu, *Prog. Surf. Sci.* **61**, 1 (1999).
- [57] G. Koren, A. Gupta, R. J. Baseman, M. I. Lutwyche, and R. B. Laibowitz, *Appl. Phys. Lett.* **55**, 2450 (1989).
- [58] R. Kelly, J. J. Cuomo, P. A. Leary, J. E. Rothenberg, B. E. Braren, and C. F. Aliotta, *Nucl. Inst. Meth. B* **9**, 329 (1985).
- [59] P. P. Pronko, S. K. Dutta, D. Du, and R. K. Singh, *J. Appl. Phys.* **78**, 6233 (1995).
- [60] H. E. Elsayed-Ali, T. B. Norris, M. A. Pessot, and G. Mourou, *Phys. Rev. Lett.* **58**, 1212 (1987).
- [61] P. P. Pronko, P. A. Van Rompay, and S. Sato, *Proc. SPIE- Int. Soc. Opt. Eng.* **3269**, 46 (1998).
- [62] T. Scharf and H.U. Krebs, *Appl. Phys. A* **75**, 551 (2002).
- [63] J. Haverkamp, R. M. Mayo, M. A. Bourham, J. Narayan, C. Jin, G. Duscher J. *Appl. Phys.* **93**, 3627, (2003).
- [64] M. A. Hafez, M. A. Khedr, F. F. Elaksher, and Y. E. Gamal, *Plasma Sources Sci. Technol.* **12**, 185, (2003).
- [65] S. S. Harilal, C. V. Bindhu, M. S. Tillack, F. Najmabadi, A. Gaeris, *J. Phys. D: Appl. Phys.* **35**, 2935 (2002).

- [66] W. Marine, J. M. Scotto, D'Aniello, and J. Marfaing, *Appl. Surf. Sci.* **46**, 239 (1990).
- [67] J. F. Ready, *Appl. Phys. Lett.* **3**, 11 (1963).
- [68] R. K. Singh, D. Bhattacharya, and J. Narayan, *Appl. Phys. Lett.* **57**, 2022 (1990).
- [69] D. Bhattacharya, R. K. Singh, and P. H. Holloway, *J. Appl. Phys.* **70**, 5433 (1991).
- [70] H. Dupendant, J. P. Gavigan, D. Givord, A. Lienard, J. P. Rebouillat, and Y. Souche, *Appl. Surf. Sci.* **43**, 369 (1989).
- [71] E. E. Donaldson, J. T. Dickinson, and S. K. Bhattacharya, *J. Adhesion* **25**, 281 (1988).
- [72] F. Qian, R. K. Singh, S. K. Dutta, and P. P. Pronko, *Appl. Phys. Lett.* **67**, 3120 (1995).
- [73] R. Kelly, *J. Chem. Phys.* **92**, 5047 (1990).
- [74] O. Auciello, S. Athavale, O. E. Hankins, M. Sito, A. F. Schreiner, and N. Biunno, *Appl. Phys. Lett.* **53**, 72 (1988).
- [75] X. D. Wu, R. E. Muenchausen, S. Foltyn, R. C. Estler, R. C. Dye, C. Flamme, N. S. Nogar, A. R. Garcia, J. Martin, and J. Tesmer, *Appl. Phys. Lett.* **56**, 1481(1990).
- [76] W. Braun, *Applied RHEED*, (Springer-Verlag, Berlin, 1999).
- [77] A. Ichimiya and P. I. Cohen, *Reflection High Energy Electron Diffraction*, (Cambridge University Press, Cambridge, 2004).
- [78] S. Nishikawa and S. Kikuchi, *Nature* **122**, 726 (1928).
- [79] D. Tang and H. E. Elsayed-Ali, *Phys. Rev. B* **50**, 18674 (1994).

- [80] X. Zeng, B. Lin, I. El-Kholy, and H. E. Elsayed-Ali, *Phys. Rev. B* **59**, 14907 (1999).
- [81] C. Rajapaksha and A. Freundlich, *J. Cryst. Growth* **311**, 1758 (2009).
- [82] D. W. Pashley, J. H. Neave, and B. A. Joyce, *Surf. Sci.* **603**, L1 (2009).
- [83] V. Cimalla, K. Zekentes, and N. Vouroutzis, *Mater. Sci. Eng. B* **88**, 186 (2002).
- [84] R. R. Lunt, J. B. Benziger, S. R. Forrest, *Apl. Phys. Lett.* **90**, 181932-1- 181932 (2007).
- [85] I. Hernandez-Calderon and H. Höchst, *Phys. Rev. B* **27**, 4961 (1983).
- [86] R. T. Brewer, J. W. Hartman, J. R. Groves, P. N. Arendt, P. C. Yashar, and H. A. Atwater, *Appl. Surf. Sci.* **175-176**, 691 (2001).
- [87] T. Mori, T. Hanada, T. Morimura, K. Shin, H. Makino, and T. Yao, *Appl. Surf. Sci.* **237**, 230 (2004).
- [88] A. Feltrin and A. Freundlich, *Jour. Cryst. Growth* **301-302**, 38 (2007).
- [89] S. Hasegawa, S. Ino, Y. Yamamoto, and H. Daimon, *Jpn. J. Appl. Phys* **24**, L387 (1985).
- [90] K. Saiki, T. Kono, K. Ueno, and A. Koma, *Rev. Sci. Instrum.* **71**, 3478 (2000).
- [91] P. Mazurek, A. Daniluk, and K. Paprocki, *Vacuum* **72**, 363 (2004).
- [92] S. Nagano, *Phys. Rev. B* **42**, 7363 (1990).
- [93] H. Nakahara, T. Hishida, and A. Ichimiya, *Appl. Surf. Sci.* **212-213**, 157 (2003).
- [94] Z. L. Wang, *Reflection electron microscopy and spectroscopy for surface analysis*, (Cambridge University Press, Cambridge, 1996).
- [95] D. H. A. Blank, G. J. H. M. Rijnders, G. Koster, and H. Rogalla, *Appl. Surf. Sci.* **127-129**, 633 (1998).

- [96] G. J. H. M. Rijnders, G. Koster, D. H. A. Blank, and H. Rogalla, *Mater. Sci. Eng. B* **56**, 223 (1998).
- [97] N. L. Yakovlev, P. A. Maksym and J. L. Beeby, *Surf. Sci.* **529**, 319 (2003).
- [98] Y. Shigeta and Y. Fukaya, *Appl. Surf. Sci.* **237**, 21 (2004).
- [99] H. E. Elsayed-Ali and G. A. Mourou, *Appl. Phys. Lett.* **52**, 103 (1988).
- [100] Y. Horio, Y. Hashimoto, and A. Ichimiya, *Appl. Surf. Sci.* **100-101**, 292 (1996).
- [101] P. Staib, W. Tappe, and J. P. Contour, *J. Cryst. Growth* **201-202**, 45 (1999).
- [102] U. Weierstall, J. M. Zuo, T. Kjörsvik, and J. C. H. Spence, *Surf. Sci.* **442**, 239 (1999).
- [103] Z. Mitura and J. L. Beeby, *J. Phys.: Condens. Matter* **8**, 8717 (1996).
- [104] C.-Y. Ruan, F. Vigliotti, Vladimir A. Lobastov, S. Chen, and A. H. Zewail, *Proc. Natl. Acad. Sci. USA* **3**, 1123 (2004).
- [105] X. Zeng and H. E. Elsayed-Ali, *Surf. Sci.* **497**, 373 (2002).
- [106] P. Sandström, E. B. Svedberg, J. Birch, and J.-E. Sundgren, *Surf. Sci.* **437**, L767 (1999).
- [107] A. Janzen, B. Krenzer, O. Heinz, P. Zhou, D. Thien, A. Hanisch, F.-J. Meyer zu Heringdorf, D. von der Linde, and M. Horn von Hoegen, *Rev. Sci. Instrum.* **78**, 013906 (2007).
- [108] J. W. Herman and H. E. Elsayed-Ali, *Phys. Rev. Lett.* **68**, 2952 (1992).
- [109] J. W. Herman, H. E. Elsayed-Ali, and E. A. Murphy, *Phys. Rev. Lett.* **71**, 400 (1993).
- [110] H. Bethe, *Annalen der Physik* **392**, 55 (1928).
- [111] C. Davisson and L. H. Germer, *Phys. Rev.* **30**, 705 (1927).

- [112] L.M. Peng, S.L. Dudarev and M.J. Whelan, *High Energy Electron Diffraction and Microscopy*, (Oxford University Press, Oxford, 2004).
- [113] P. A. Maksym and J. L. Beeby, *Surf. Sci.* **110**, 423 (1981).
- [114] N. Masud and J. B. Pendry, *J. Phys. C: Solid State Phys.* **9**, 1833 (1976).
- [115] N. L. Yakovlev, A. G. Banskchikov, M. M. Moisseeva, N. S. Sokolov, J. L. Beeby, and P. A. Maksym, *Surf. Interface Anal.* **28**, 264 (1999).
- [116] M. De Graef, *Introduction to conventional transmission electron microscope*, (UK University Press, Cambridge, 2003).
- [117] G. Binnig and H. Rohrer, *Rev. Mod. Phys.* **59**, 615 (1987).
- [118] C. J. Chen, *Introduction to Scanning Tunneling Microscopy*, (Oxford University Press, New York, 2001).
- [119] R. Young, J. Ward, and F. Scire, *Phys. Rev. Lett.* **27**, 922 (1971).
- [120] G. Binnig, H. Rohrer, Ch. Gerber, and E. Weibel, *Phys. Rev. Lett.* **50**, 120 (1983).
- [121] G. Binnig and H. Rohrer, *Rev. Mod. Phys.* **71**, S324 (1999).
- [122] A. Cricenti, R. Generosi, and S. Selci, *Rev. Sci. Instrum.* **65**, 80 (1994).
- [123] S. Mannsfeld, M. Toerker, T. Schmitz-Hübsch, F. Sellam, T. Fritz, and K. Leo, *Org. Electr.* **2**, 121 (2001).
- [124] H. Hövel, T. Becker, D. Funnemann, B. Grimm, C. Quitmann, and B. Reihl, *J. Electr. Spect. Rel. Phen.* **88-91**, 1015 (1998).
- [125] K.Takayanagi, Y.Ohshima, K.Mohri, Y.Naitoh, H.Hirayama, Y.Tanishiro, and Y.Kondo, *Microscopy Microanal.* **8**,414 (2002).
- [126] I. Costina, M. Schmid, H. Schiechl, M. Gajdoš, A. Stierle, S. Kumaragurubaran, J. Hafner, H. Dosch, and P. Varga, *Surf. Sci.* **600**, 617 (2006).

- [127] D. Erts, A. Löhmus, R. Löhmus, H. Olin, Appl. Phys. A Mater. Sci. Process. **72**, 71 (2001).
- [128] D. Porath, Nature Nano. **4**, 476 (2009).
- [129] S. Selci and A. Cricenti, Physc. Script. 1991 **T35**, 107 (1991).
- [130] S. Dey, S. Pethkar, S. D. Adyanthaya, M. Sastry, and C. V. Dharmadhikari Bull. Mater. Sci. **31**, 309 (2008).
- [131] E. Shapir, H. Cohen, T. Sapir, N. Borovok, A.B. Kotlyar and D. Porath, J. Phys. Chem. B **110**, 4430 (2006).
- [132] C. Bai, *Scanning Tunneling Microscopy and its Applications*, (Springer, New York, 2000).
- [133] R. Wiesendanger, D. Bürgler, G. Tarrach, T. Schaub, U. Hartmann, H. -J. Güntherodt, I. V. Shvets and J. M. D. Coey, Appl. Phys. A: Mater. Sci. Process. **53**, 349 (1991).
- [134] S.-W. Hla, J. Vac. Sci. Tech. B **23**, 1351 (2005).
- [135] D. A. Bonnell, *Scanning Probe Microscopy and Spectroscopy: Theory, Tehcniques and Applications*, (Wiley, Newyork, 2000).
- [136] R. Weisendanger, *Scanning Probe Microscopy and Spectroscopy: Methods and Applications*, (Cambridge University Press, Cambridge, 1994).
- [137] T. Furuhashi, Yoshifumi Oshima, and H. Hirayama, Appl. Surf. Sci. **253**, 651 (2006).
- [138] S. Selci, G. Latini, M. Righini, S. Franchi, and P. Frigeri, Mater. Sci. Eng. B **88**, 168 (2002).
- [139] J. Yoshikawa, S. Kurokawa, and A. Sakai, Appl. Surf. Sci. **169-170**, 202 (2001).

- [140] G. Binnig and H. Rohrer, *Surf. Sci.* **126**, 236 (1983).
- [141] A. Sinsarp, Y. Yamada, M. Sasaki, and S. Yamamoto, *Appl. Surf. Sci.* **237**, 583 (2004).
- [142] J. F. Jia, K. Inoue, Y. Hasegawa, and W. S. Yang, *Phys. Rev. B* **58**, 1193 (1998).
- [143] M. Yata, M. Ozaki, S. Sakata, T. Yamada, A. Kohno, M. Aono, *Jap. J. Appl. Phys.* **28**, L885 (1989).
- [144] M. Johnson and J. Clarke, *J. Appl. Phys.* **67**, 6141 (1990).
- [145] R. Koltun, M. Herrmann, G. Güntherodt, V. A. M. Brabers, *Appl. Phys. A Mater. Sci. Process.* **73**, 49 (2001).
- [146] C. Albonetti, I. Bergenti, M. Cavallini, V. Dediu, M. Massi, J.-F. Moulin, and F. Biscarini, *Rev. Sci. Instrum.* **73**, 4254 (2002).
- [147] J. Prokop, A. Kukunin, and H. J. Elmers, *Phys. Rev. B* **73**, 014428 (2006)
- [148] S. Murphy, J. Osing, and I. V. Shvets, *J. Magn. Magnet. Mater.* **198-199**, 686 (1999).
- [149] H. Yang, A. R. Smith, M. Prikhodko, and W. R. L. Lambrecht, *Phys. Rev. Lett.* **89**, 226101 (2002).
- [150] N. R. Wilson and J. V. Macpherson, *Nature Nanotech.* **4**, 483 (2009).
- [151] F.-K. Tung, M. Yoshimura, and K. Ueda, *J. Nanomater.* **2009**, 1 (2009).
- [152] G. I. Márk, L. P. Biró, J. Gyulai, P. A. Thiry, A. A. Lucas, and P. Lambin, *Phys. Rev. B* **62**, 2797 (2000).
- [153] K. Cho and J. D. Joannopoulos, *Phys. Rev. Lett.* **71**, 1387 (1993).
- [154] G. Binnig, H. Rohrer, Ch. Gerber, and E. Weibel, *Appl. Phys. Lett.* **40**, 178 (1982).

- [155] R. J. Hamers and U. K. Köhler *J. Vac. Sci. Tech. A* **7**, 2854 (1989).
- [156] T. Miyazaki, T. Uda, and K. Terakura, *Mater. Sci. Eng. B* **58**, 48 (1999).
- [157] D. J. Paul, *Semicond. Sci. Tech.* **19**, R75 (2004).
- [158] K. Tanimura, E. Inami, J. Kanasaki, and W. P. Hess, *Phys. Rev. B* **74**, 035337 (2006).
- [159] V. A. Fedotov, K. F. MacDonald, N. I. Zheludev, and V. I. Emel'yanov, *J. Appl. Phys.* **93**, 3540 (2003).
- [160] A. V. Dvurechenskiĭ, V. A. Zinov'ev, and Zh. V. Smagina, *JETP Lett.* **74**, 267 (2001).
- [161] V. A. Volodin, A. V. Yakimov, A. V. Dvurechenskiĭ, M. D. Efremov, I. Nikiforov, E. I. Gatskevich, G. D. Ivlev, and G. Y. Mikhalev, *Semiconductors* **40**, 202 (2006).
- [162] W. Hoheisel, M. Vollmer, and F. Trager, *Phys. Rev. B* **48**, 17463 (1993).
- [163] I. Lee, T. A. Callcott, and E. T. Arakawa, *Phys. Rev. B* **47**, 6661 (1993).
- [164] Z. Wu, *Phys. Lett. A* **131**, 486 (1988).
- [165] M. S. Hegazy and H. E. Elsayed-Ali, *J. Appl. Phys.* **104**, 124302 (2008).
- [166] A. V. Dvurechenskiĭ, J. V. Smagina, R. Groetzschel, V. A. Zinovyev, V. A. Armbrister, P. L. Novikov, S. A. Teys, and A. K. Gutakovskii, *Surf. Coat. Technol.* **196**, 25 (2005).
- [167] C. Hernandez, Y. Campidelli, D. Simon, D. Bensahel, I. Sagnes, G. Patriarche, P. Boucaud, and S. Sauvage, *J. Appl. Phys.* **86**, 1145 (1999).
- [168] Z. M. Zhang, L. M. Hanssen and R. U. Datla, *Infrared Phys. Technol.* **37**, 539 (1996).

- [169] E. Inami and K. Tanimura, *Surf. Sci.* **603**, L63 (2009).
- [170] Y. J. Chabal, S. B. Christman, E. E. Chaban, and M. T. Yin, *J. Vac. Sci. Technol. A* **1**, 1241 (1983).
- [171] W. Mönch, P. Koke, and S. J. Krueger, *J. Vac. Sci. Technol.* **19**, 313 (1981).
- [172] K. Tanimura and J. Kanasaki, *J. Phys.: Condens. Matter* **18**, S1479 (2006).
- [173] I. W. Boyd, S. C. Moss, T. F. Howson, and L. J. Willis, *Appl. Phys. Lett.* **45**, 80 (1984).
- [174] D. Srivastava and B. J. Garrison, *Phys. Rev. B* **46**, 1472 (1992).
- [175] J. A. Misewich, T. F. Heinz, and D. M. Newns, *Phys. Rev. Lett.* **68**, 3737 (1992).
- [176] H. M. van Driel, *Phys. Rev. B* **35**, 8166 (1987).
- [177] K. G. Svantesson and N. G. Nilsson, *J. Phys. C* **12**, 3837 (1979).
- [178] G. Betz and P. Varga, *Desorption Induced by Electronic Transitions—DIET IV*, (Springer, Berlin, 1990).
- [179] M. L. Knotek and P. J. Feibelman, *Phys. Rev. Lett.* **40**, 964 (1978).
- [180] D. Menzel and R. Gomer, *J. Chem. Phys.* **41**, 3311 (1964).
- [181] P. A. Redhead, *Can. J. Phys.* **42**, 886 (1964).
- [182] J. A. Bearden and A. F. Burr, *Rev. Mod. Phys.* **39**, 125 (1967).
- [183] J. Kanasaki, A. Okano, K. Ishikawa, Y. Nakai, and N. Itoh, *Nucl. Instrum. Methods Phys. Res. B* **101**, 93 (1995).
- [184] E. Inami and K. Tanimura, *Phys. Rev. B* **76**, 035311 (2007).
- [185] H. Sumi, *Surf. Sci.* **248**, 382 (1991).
- [186] J. Kanasaki, M. Nakamura, K. Ishikawa, and K. Tanimura, *Phys. Rev. Lett.* **89**, 257601 (2002).

- [187] P. W. Anderson, *Phys. Rev. Lett.* **34**, 953 (1975).
- [188] I.-K. Yu and K. Tanimura, *Solid State Commun.* **101**, 429 (1997).
- [189] J. Kanasaki, K. Katoh, Y. Imanishi, and K. Tanimura, *Appl. Phys. A: Mater. Sci. Process.* **79**, 865 (2004).
- [190] K. Ishikawa, J. Kanasaki, K. Tanimura, and Y. Nakai, *Solid State Commun.* **98**, 913 (1996).
- [191] N. Itoh, K. Hattori, Y. Nakai, J. Kanasaki, A. Okano, C. K. Ong, and G. S. Khoo, *Appl. Phys. Lett.* **60**, 3271 (1992).
- [192] K. S. Khoo, C. K. Ong, and N. Itoh, *J. Phys.: Condens. Matter.* **5**, 1187 (1993).
- [193] I.-K. Yu, J. Kanasaki, A. Okano, Y. Nakai, and N. Itoh, *J. Phys. Condens. Matter* **8**, 1475 (1996).
- [194] D. J. Eaglesham, H.-J. Gossmann, and M. Cerullo, *Phys. Rev. Lett.* **65**, 1227 (1990).
- [195] D. J. Eaglesham and M. Cerullo, *Appl. Phys. Lett.* **58**, 2276 (1991).
- [196] A. I. Nikiforov, B. Z. Kanter, and O. P. Pchelyakov, *Thin Solid Films* **336**, 179 (1998).
- [197] X. Zeng and H. E. Elsayed-Ali, *Phys. Rev. B* **64**, 085410 (2001).
- [198] X. Zeng, B. Lin, I. El-Kholy, and H. E. Elsayed-Ali, *Phys. Rev. B.* **59**, 14907 (1999).
- [199] S. Sánchez-Cortés and J. V. García-Ramos, *Langmuir* **16**, 764 (1999).
- [200] N. M. Hwang and D. Y. Kim, *Int. Mater. Rev.* **49**, 171 (2004).
- [201] K. Katayama, K. Shibamoto, and T. Sawada, *Chem. Phys. Lett.* **345**, 265 (2001).

- [202] R. Ruiz, D. Choudhary, B. Nickel, T. Toccoli, K.-C. Chang, A. C. Mayer, P. Clancy, J. M. Blakely, R. L. Headrick, S. Iannotta, and G. G. Malliaras, *Chem. Mater.* **16**, 4497 (2004).
- [203] W. Shindo and T. Ohmi, *J. Appl. Phys.* **79**, 2347 (1996).
- [204] R. Ditchfield and E. G. Seebauer, *Phys. Rev. Lett.* **82**, 1185 (1999).
- [205] G. Lengel, J. Harper, and M. Weimer, *Phys. Rev. Lett.* **76**, 4725 (1996).
- [206] R. Kometer and N. Schwentner, *J. Chem. Phys.* **104**, 6967 (1996).
- [207] Y. -W. Mo and M.G. Lagally, *Surf. Sci.* **248**, 313 (1991).
- [208] A. Dolbak and B. Olshanetsky, *Cent. Eur. J. Phys.* **4**, 310 (2006).
- [209] H. J. Kim, Z. M. Zhao, J. Liu, V. Ozolins, J. Y. Chang, and Y. H. Xie, *J. Appl. Phys.* **95**, 6065 (2004).
- [210] M. A. Hafez and H.E. Elsayed-Ali, *J. Appl. Phys.* **101**, 113515 (2007).
- [211] B. A. Joyce, P. J. Dobson, J. H. Neave, and J. Zhang, *Surf. Sci.* **174**, 1 (1986).
- [212] J. H. Neave, P. J. Dobson, B. A. Joyce, and J. Zhang, *Appl. Phys. Lett.* **47**, 100 (1985).
- [213] D. H. A. Blank, G. J. H. M. Rijnders, G. Koster, and H. Rogalla, *Appl. Surf. Sci.* **138-139**, 17 (1999).
- [214] V. Cherepanov and B. Voigtländer, *Phys. Rev. B* **69**, 125331 (2004).
- [215] R. Hull and J. C. Bean, *Germanium Silicon: Physics and Materials* (Academic Press, San Diego, 1999).
- [216] L. Bardotti, P. Jensen, A. Hoareau, M. Treilleux, and B. Cabaud, *Phys. Rev. Lett.* **74**, 4694 (1995).

- [217] K. Oura, V. G. Lifshits, A. A. Saranin, A. V. Zotov, and M. Katayama, *Surface Science: An Introduction*, (Springer, Berlin, 2003).
- [218] J. M. Wen, S. -L. Chang, J. W. Burnett, J. W. Evans, and P. A. Thiel, *Phys. Rev. Lett.* **73**, 2591 (1994).
- [219] A. Bogicevic, S. Liu, J. Jacobsen, B. Lundqvist, and H. Metiu, *Phys. Rev. B* **57**, R9459 (1998).
- [220] F. Vigliotti, S. Chen, C.-Y. Ruan, V. A. Lobastov, and A. H. Zewail, *Angew. Chem. Int. Ed.* **43**, 2705 (2004).
- [221] T. LaGrange, M. R. Armstrong, K. Boyden, C. G. Brown, G. H. Campbell, J. D. Colvin, W. J. DeHope, A. M. Frank, D. J. Gibson, F. V. Hartemann, J. S. Kim, W. E. King, B. J. Pyke, B. W. Reed, M. D. Shirk, R. M. Shuttlesworth, B. C. Stuart, B. R. Torralva, and N. D. Browning, *Appl. Phys. Lett.* **89**, 044105 (2006).
- [222] Michael R. Armstrong, Bryan W. Reed, Ben R. Torralva, and Nigel D. Browning, *Appl. Phys. Lett.* **90**, 114101 (2007).
- [223] Judy S. Kim, Thomas LaGrange, Bryan W. Reed, Mitra L. Taheri, Michael R. Armstrong, Wayne E. King, Nigel D. Browning, and Geoffrey H. Campbell, *Science* **321**, 1472 (2008).
- [224] B. S. Swartzentruber, *Phys. Rev. Lett.* **76**, 459 (1996).
- [225] M. C. Tringides and M. Hupalo, *J. Phys.: Condens. Matter* **22**, 264002 (2010).
- [226] J. Bonse, S. Baudach, J. Krüger, W. Kautek, and M. Lenzner, *Appl. Phys. A* **74**, 19 (2002).
- [227] Y. Pauleau, *Materials Surface Processing by Directed Energy Techniques*, (Elsevier, Amsterdam, 2006).

[228] D. J. Eaglesham and M. Cerullo, *Phys. Rev. Lett.* **64**, 1943 (1990).

[229] G. Jin, J. L. Liu, and K. L. Wang, *Appl. Phys. Lett.* **83**, 2847 (2003).

APPENDIX A

PULSED LASER DEPOSITION SYSTEM EQUIPPED WITH RHEED

A. 1. SYSTEM DESIGN AND COMPONENTS

The main components of the system are shown in Fig. 33. Images for the rest of the components will appear later in the operation description.

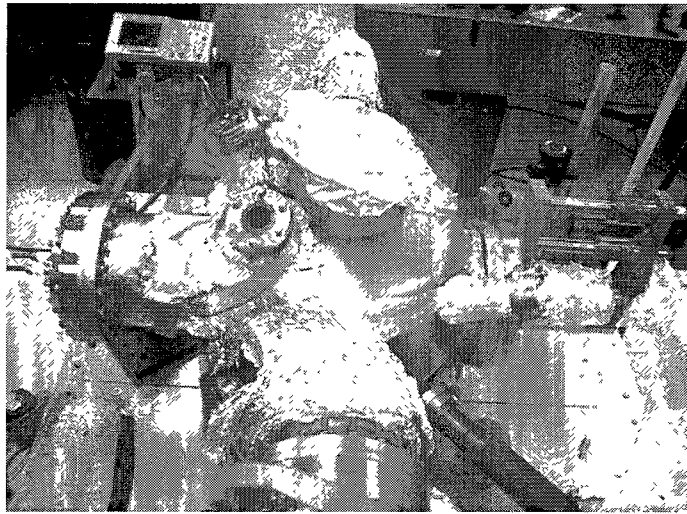


FIG. 33. RHEED chamber top view.

A. 2. PUMPING UP AND OPENING THE SYSTEM

When you need to open the chamber, you must follow the procedure below very carefully. Make sure that electron gun is off. Otherwise, filament will oxidize at high pressure easily and will be burnt.

1. Make sure that vent valve of the turbo is closed.
2. Turn on the roughing mechanical pump after few seconds turn ON the turbo pump.
3. Turn off the ion pump.

4. Close the butterfly valve to separate the ion pump from the chamber.
5. When pressure in the chamber reaches $\sim 10^{-7}$ Torr, open the right angle UHV valve slowly.
6. Wait for a few minutes, while the system is pumped by the turbo and the roughing pump so that pressure difference between chamber and hose come into equilibrium.
7. Turn off the turbo and then the mechanical pump.

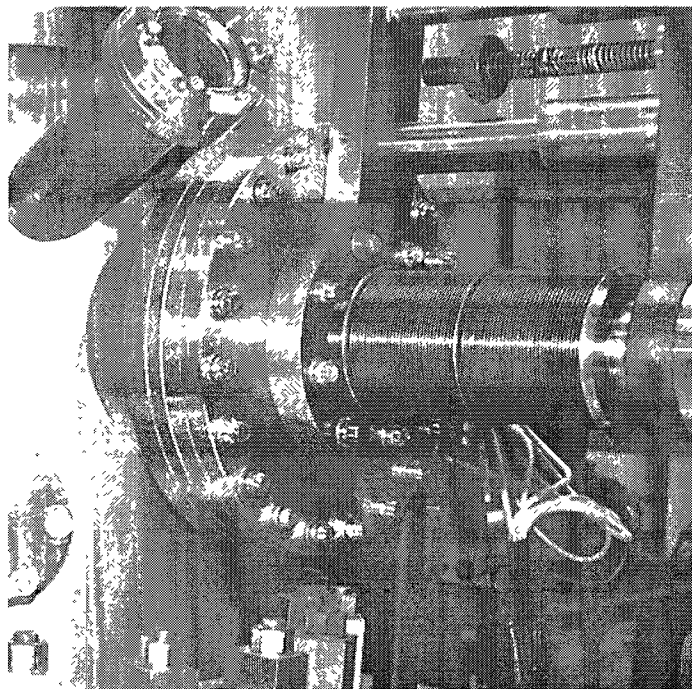


FIG. 34. Sample manipulator.

8. After around 10 seconds open the turbo vent valve very slowly till the turbo stops and the chamber is completely filled by air. If you open it fast, you may damage the turbo pump blades.
9. Unscrew the screws of the 8" flange holding the sample manipulator, Fig. 34.

10. Take the sample manipulator out; place it on a clean bench and close the open port with a plastic cap, Fig. 35. When taking out sample manipulator, be careful not to hit it inside the chamber.

A. 3. CLEANING AND CHANGING THE SUBSTRATE

You have to change the substrate after each run. It is recommended to have at least a few chemically cleaned samples. Sample cleaning is made by using modified Shiraki method. More information is given below.

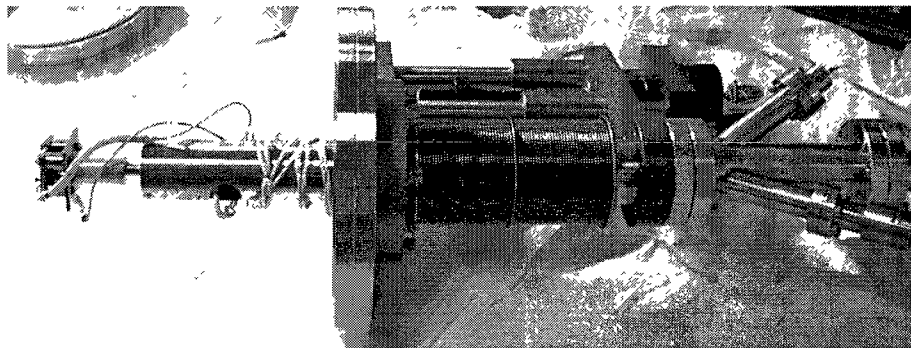


FIG. 35. Sample manipulator and substrate holder.

1. Clean the substrates, using the following method: The samples are dipped into a solution of H_2SO_4 (97 wt %): H_2O_2 (30 wt %) = 4:1 (by volume) for 10 min, rinsed with ultra pure water for 10 min, then dipped into a solution of HF (50 wt %): H_2O = 1:10 (by volume) for 1 min. **Caution: HF is a very dangerous solution, avoid direct exposure to skin and do NOT inhale its fumes.** Unused clean samples are stored under ethanol.
2. Install the new sample and put the thermocouple between the clips and the sample so that it firmly touches the sample's surface.

3. Install the sample holder back to the manipulator. Make sure to measure the resistance of the sample and make sure that there is no short circuit anywhere.
4. Install the sample manipulator back to the system and securely fastened all screws. Remember to change the gasket. **Caution: Do NOT risk scratching the knife edge of the conflat flange when changing the gasket.**

A. 4. CHANGING THE TARGET

1. Unscrew the 8" flange holding the target holder, Fig. 36.

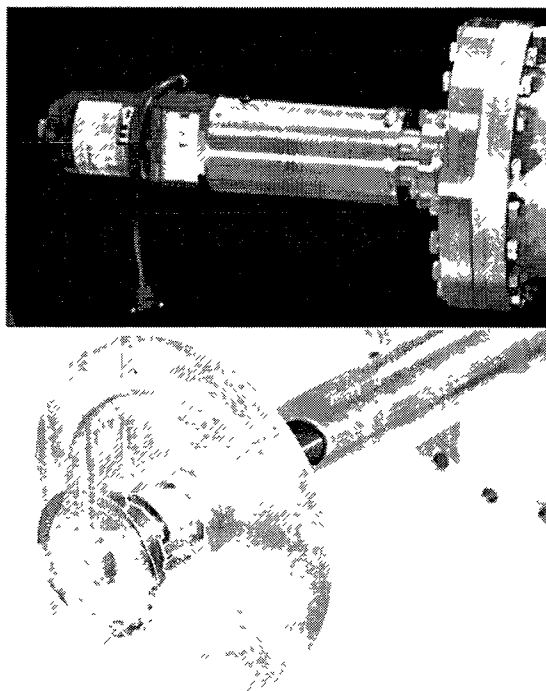


FIG. 36. Germanium target and target holder.

2. To remove the installed target, hold your fingers around the target, Fig. 36, and rotate it clockwise, then pull it out.
3. Place the target upside-down on a clean surface.

4. Using a heat gun, heat the target-holder interface for a few minutes till the “Torr Seal” completely cures and the target is detached from the base holder. You will need to heat the entire circumference uniformly by directing the heat gun to different areas. Remove the residual Torr Seal by razor.
5. Wet a clean tissue with ethanol and place the Ge wafer upside-down, then rotate it gently on the wet tissue
6. Prepare Torr Seal for 2:1 volume to glue Ge target to the shaft.
7. Install the target holder base to its location and rotate it anti-clockwise.
8. Install the flange back and tighten all the screws.

A. 5. PUMPING THE SYSTEM DOWN AND BAKEOUT THE SYSTEM

Before you start pump down, make sure that vent valve on turbo pump is completely closed, the new gasket is installed, and fan is working to cool down turbo pump. And from time to time, use anti-seize for bolts to prevent galling.

1. Turn on the roughing pump and turbo pump. Watch the speed and temperature of the turbo pump during pumping down. Normally, turbo pump should come to maximum speed in couple of minutes. If not, check the vent valve, check if there is any untightened screws. Lastly, you can turn off turbo and mechanical pump and restart them again.
2. When the turbo reaches its maximum pumping speed, turn ON the ion gauge.
3. In several hours, base pressure should be low 10^{-6} Torr. Then, you can start bake out procedure under turbo and mechanical pump.
4. Burp the ion pump several times when baking under turbo and mechanical pump.
5. When pressure low 10^{-6} Torr, turn on ion pump.

6. Wait at least 12 more hours.
7. Pressure should be low 10^{-7} Torr. Then, start cool down the chamber.
8. After another 24 hours, pressure should be high 10^{-10} Torr.



FIG. 37. Lumonics YAG Master (YM) 200 laser system.

You don't need to use TSP in RHEED chamber unless it is really necessary. During bakeout, you can set the sample temperature to $\sim 500^\circ$. This will make degassing better.

A. 6. ND:YAG LASER OPERATION

The Lumonics YAG Master 200 laser was used to ablate germanium and excite silicon substrate, shown in Fig. 37. Make sure that you enough cooling water inside chiller located at the bottom of power supply. Once every month, water level must be checked.

A.6.1. TURN ON PROCEDURE

1. Make sure that you and everyone within sight of laser is wearing laser eye protection.
2. Turn ON the external cooling city water supply.
3. Rotate the “red” mains to ON position. The cooler pump will start.
4. Allow at least 30 minutes for the coolant and the HGA ovens to reach the operating temperature.
5. Turn the ENABLE key switch on the control unit clockwise to the horizontal ON position.
6. After a delay of 5 seconds the power supply is enabled and the ON LED, next to the key switch will light up indicating the start of the flashlamp.
7. From the pockels cell divider buttons, push the button to deliver the desired frequency (by dividing the default 50 Hz).
8. Using the “oscillator” flashlamp selector, choose the required value.
9. Press the shutter “OPEN” button.
10. Press the oscillator “ON” button, the flashlamp will begin to pulse.
11. Check, using an IR viewer, along the beam path that there are no unwanted reflections and that the beam is safely contained.
12. To momentarily stop the beam, simply press the OPEN shutter pushbutton.

A.6.2. TURN OFF PROCEDURE

1. Press the oscillator OFF pushbutton and press the shutter CLOSE the button.
2. Turn the ENABLE key switch to the vertical OFF position.
3. Leave the cooler pump ON for at least 30 minutes to cool down the system.
4. Switch OFF the cooler.

APPENDIX B

**PULSED LASER DEPOSITION SYSTEM EQUIPPED WITH SCANNING
TUNNELING MICROSCOPE**

B.1. SYSTEM DESIGN AND COMPONENTS

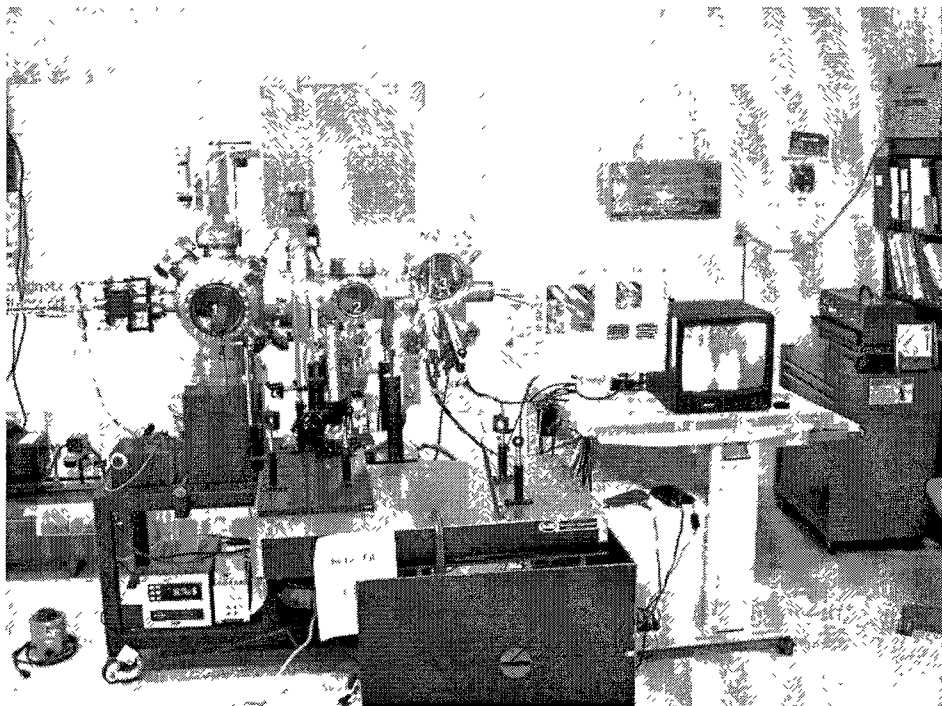


FIG. 38. System design and components.

Image of PLD STM system in our lab could be seen in Fig. 38. Our system consists of deposition chamber, analysis chamber coupled with Omicron VT STM, and load lock. In our system, we do have oil-free roughing pump, turbo molecular pump connected to main chamber, turbo molecular pump connected to load lock, ion pump, and titanium sublimation pump (TSP). We use two ion gauges to monitor pressure in main chamber and in load lock. We also have convectron gauge that shows pressure from ambient to

millitorr range. Always keep the system under vacuum even if you don't use the system. For sample transfer, two magnetic transporters are used. This will keep the chamber clean and enable you to get UHV in subsequent pump downs.

B.2. PUMPING UP PLD STM CHAMBER WITHOUT USING LOAD LOCK

1. Turn the Turbo and mechanical pump on while all valves are closed. Wait ~15 minutes until you get pressure inside roughing hose $\sim 10^{-6}$ Torr.
2. By using the gate valve, shown in Fig. 39, close the connection between two chambers.

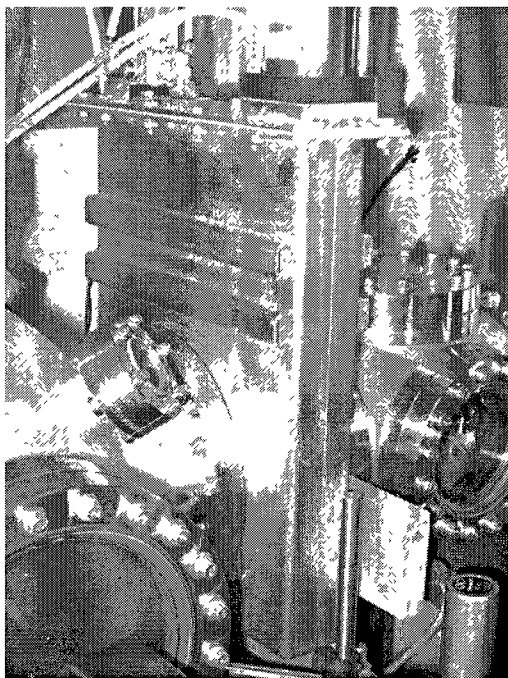


FIG. 39. Gate Valve.

3. Use the pressure switch to close the gate valve. Make sure that it is closed completely. When it is completely closed, you will hear a rattling noise. Meanwhile, deposition chamber is still under UHV. The first chamber is under Turbo pump. Note that

pressure required to open gate valve is 20 psi. However to close it, we need higher pressure around 60 psi.

4. Having waited for enough time, open the valve between Turbo pump and deposition chamber.
5. After you get first chamber's pressure around ambient pressure, turn the turbo and mechanical pump off.
6. Rotate the vent valve slowly to let the air in.
7. Unscrew the 6" port. (Do it diagonally).

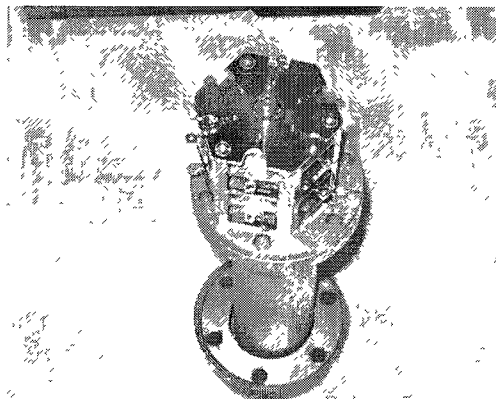


FIG. 40. Carousel for samples and tips.

8. Put the red cap with tissue to cover the port.
9. Loose the screw under the carousel and then take the carousel out. Make sure that you put the gloves on and be careful not to drop washers, shown in Fig. 40.
10. Change the tip and samples by recording what you did on the sample change information sheet.
11. Change the gasket whenever you open the system. In this case change 6" gasket.
12. Close the port.

B.3. REPLACING THE SAMPLE

1. Put the sample plate on hot plate at 350° to melt the silver paste.
2. Scrape the silver paste off by screwdriver.
3. Put the sample plate in to acetone.
4. After there is no residue on the sample plate, put a dab of silver paste on your plate. This will hold your sample after it dries.
5. Stick your new sample on the sample after you immerse with HF. Don't touch the middle of the sample always use edges whenever you need to remove the samples. When you change the sample in the direct heating sample stage, be careful with direction of ceramic and short circuit.
6. Put the sample plate back in to carousel.

B.4. REPLACING THE TIP

1. Hold the tip holder from two legs, Fig. 41.

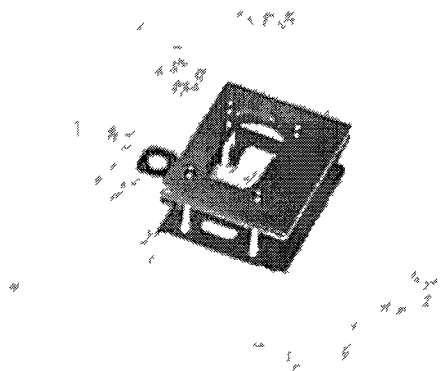


FIG. 41. Tip Holder.

2. Move it to the right and then take it out.
3. Take the new one and carefully replace it.

4. Note that magnet side of the tip should be in line with magnet of the tip holder.

B.5. BAKING OUT PLD STM CHAMBER

Before baking out the STM system, do the following two important steps to prevent any damage to the equipments.

- i- Make sure that matrix is turned off.
 - ii- Disconnect preamplifier and matrix control cable and connect short circuit plugs, Fig. 42.
1. Start bake out when pressure is 10^{-6} Torr range under turbo and mechanical pump.
Connect the connector cable in replace of preamplifier and matrix control cable.

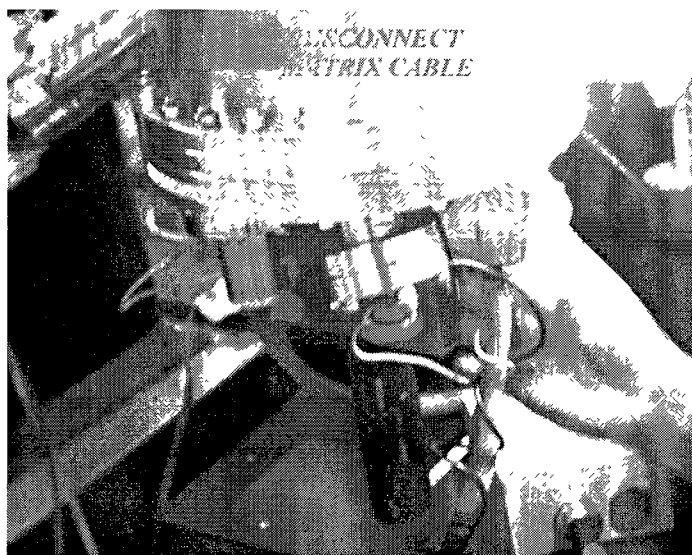


FIG. 42. STM Matrix cable connections.

2. Disconnect the motor cable that is used to rotate sample during deposition.
3. Cover the chamber with aluminum foil, Fig. 43.
4. Wrap heat tape around the chamber.

5. Connect the heating tape to the variac.
6. Make sure that chamber is grounded always.
7. Shield the system with aluminum foil.
8. Burp ion pump and degas TSP filaments several times when chamber is pumped down by turbo and molecular pump.

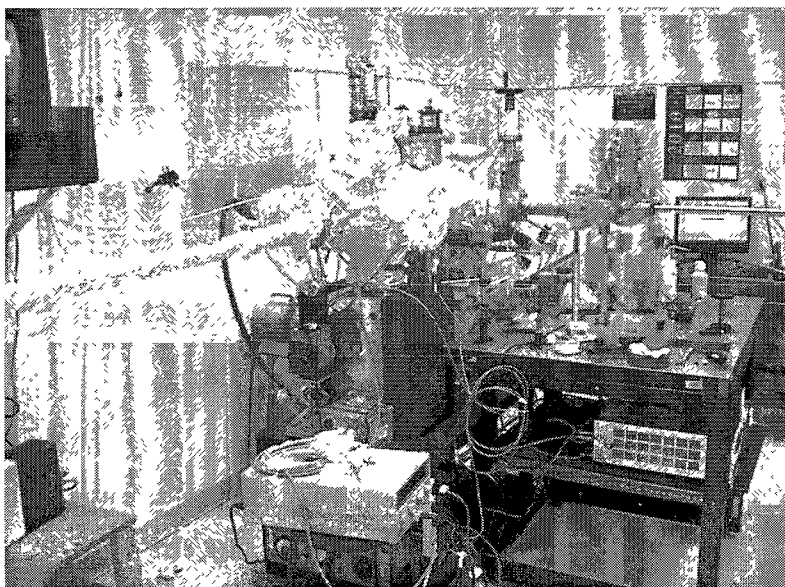


FIG. 43. PLD STM bake out.

9. When pressure low 10^{-6} Torr, turn on ion pump, leave it 12 hours more. Pressure should $\sim 1.0 \times 10^{-7}$ Torr at the end of this cycling.
10. Cool down system for another 24 hours. Start to degas silicon substrate at 600°C . If all goes well, pressure should be $\sim 4.0 \times 10^{-10}$ Torr.
11. Turn on TSP filament after let the water pass through the cooling shroud. Leave it ~ 1 min at 48 Amp. You may need to do this several times. Pressure should be 7.0×10^{-11} Torr.

12. Make sure that when you flash the silicon sample, pressure stays in 10^{-10} Torr range. If sample holder is new, use dummy sample to degas it at least one day at very high current. For the sample we use, set the current 6.5 Amper and leave it for 24 hours to degas. This will help to keep the base pressure lower in the subsequent flashing.

Because the STM is sensitive equipment, you should check the bake out temperature with a thermocouple attached to chamber. Keep it less than 150 °C.

B.6. STM OPERATION

1. Lower the PPM all the way down and secure it by rotating it to the right or to the left.
2. Turn on the Matrix by rotating power switch clockwise to the on position.

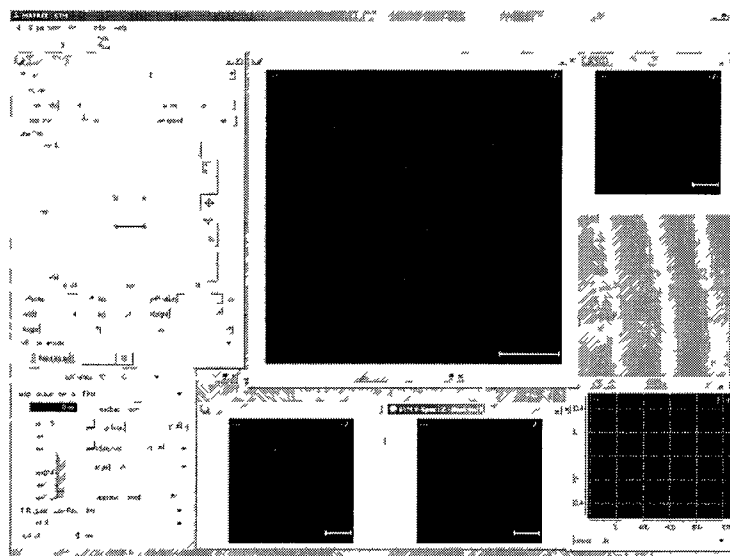


FIG. 44. Matrix interface software.

3. Log in to the computer using the username: matrix and no password.

4. Wait for ~1 minute till the communication between the PC and the Matrix via TFTP32 is established.
5. Start Matrix 2.2 software on desktop.
6. Select “STM” mode. Then select “STM Spectroscopy” mode.
7. In the Matrix software interface, shown in Fig. 44, go to the Z regulation panel, and enter the parameters that are suitable for the sample under study. For Si(100) samples, the parameters in the figure are found to be suitable starting parameters. Remember that you will need to change these parameters when you zoom in. You will need to tune the V-gap voltage, loop gain, and I-set point until you get the best images depending on your sample and on the scanned area.
8. Adjust the parameters in the XY scanner control panel. Always, start with large scan area ~500 nm and then zoom in to the smaller area of interest. You will need to tune the “raster time” depending on your sample and the scanned area.
9. Use the Matrix remote box to control the tip approach to the surface. Upon switching on the MATRIX CU the remote box display will come on and display the OMICRON logo together with the head that has been configured. Press DOWN to proceed to the BACK menu, i.e. scan piezo fully retracted and coarse positioning functions active. Operate the $\pm X$, $\pm Y$, APPR (approach) and RETR (retract) coarse motion buttons ($\pm F1$ to $\pm F3$) On the remote box. Turn regulator "SPEED" to the maximum (“10”). As the coarse steps are so small (40 nm to 400 nm at room temperature) you have to look closely to see the motion. Different directions normally have different speeds (up to a factor of 3). When you are

close to the sample reduce the step width and approach very slowly (speed of 3-4). Use the TV monitor to know how close the tip is to the surface.

You may not get atomic resolution right away. There may be several reasons behind this. Sample may not be completely clean or tip may be blunt. You can understand if the tip is in good condition from I-V spectra. However, this is not always dependable. You can click single point spectroscopy on any place in sample and then immediately move the tip into another area to get rid of some of the dirt. Alternatively, you can increase gap voltage suddenly to very high value such as 10 V for couple of scan lines. Tip will retract itself due to high voltage and when voltage is decreased to its original value, tip will be longer and high voltage cause to desorb some of the dirt on it. There are several other in-situ tip treatment models available in literature. Those need special equipments. If none of the above methods give you atomic resolution, you may crash your tip onto silicon sample softly. By doing this, tip will pick up a silicon atom and leave a defect on the surface. This method was reported to give clean image. If you still cannot get good image, you may want to change tip.

B.7. BAKE OUT PROCEDURE IN ORDER TO ACHIEVE UHV

UHV is very crucial for PLD-STM system to achieve atomically clean surfaces. Chamber walls and other UHV components are good sources of outgassing, especially when they are exposed to air. We have to bake the system out thoroughly in order to get UHV. Baking temperature should be as high as possible. For PLD-STM system, bake out temperature shouldn't exceed 150 °C as it can damage the electronics in STM. A bake out of the system over a period of at least 24 hours at temperatures around 150 °C speeds up the outgassing rate of surfaces in the vacuum system in order to get a faster and

cleaner pump down to vacuum pressures. It is recommended that temperature change shouldn't be higher than 20-25 °C per hour to minimize strain on the components in UHV system. We use heat tape to bake out our vacuum system. The heating tapes are powered by controls that can vary the voltage level of the power supply. The heating tapes were attached to the outer surfaces of the chamber walls. Aluminum adhesive tape and high temperature silicon glue could also be used to keep the tapes on the surfaces. As electrical power is sent through the tapes, the resistances of the tapes allow the tapes to be heated to the desired temperature. Because of the different geometry of our chamber, heating tape should be customized for each part. A couple of K-type sticky thermocouples have been mounted on the chamber walls at different places. The thermocouples measure the temperature of the chamber walls, providing a way of monitoring the bake out temperature. This is important because it minimizes the amount of contact with the relatively cool air outside of the chamber walls, hence providing an accurate reading of the temperature of the chamber walls. We have also used a portable thermocouple to monitor the temperature of the various parts of the vacuum chamber. Aluminum foil provides insulation and distribution of temperature evenly on all over the surface when baking out the vacuum system. Aluminum foil should be tightly wrapped around all areas of the vacuum system that require baking out. Aluminum foil should be blanked out first, then wrap the heating tapes around. Finally, cover the whole system with aluminum foil again.

There are also other things we need to be careful to maintain clean UHV system. For example, anything that will be placed inside the chamber must be made of low outgassing and low vapor pressure material. And it should be clean-free from oil, dirt,

contaminants, or coated with material which is not safe for UHV system. In case of dirt in UHV system, we have to use acetone first to remove oil and isopropanol or methanol to remove residue left due to acetone. We should take extreme precaution for PLD-STM system as it is very sensitive and even simple repair can cause thousands of dollars. Always use clean gloves and clean kimwipes when touching inside the chamber or even when removing something from chamber. When you store something, make sure that you don't damage knife edge on the flanges. First, wrap them with Kimwipes and then wrap this around aluminum foil before storing. You can also put used gasket on flanges that will be stored in order to prevent any damage on knife edge. When installing or taking off flanges always use anti-seize for bolts since the screws and nuts may seize to each other due to high bake out temperature. And clean the dirty areas on the flange due to use of anti-seize lubricant. Acetone and ethanol works well to clean anti-seize residue. Please also put a note on the stored items for possible future use.

APPENDIX C

FEMTOSECOND LASER

C.1. OVERVIEW

A femtosecond (i.e., one millionth of a billionth of a second) laser is a type of laser which emits optical pulses in a femtosecond domain (~typically between 5 to 100 fs), which is sometimes called ultrafast lasers. Femtosecond laser is nowadays indispensable tool for research labs since it has great importance over a wide range of applications such as time-resolved studies of chemical reactions, resonant multiphoton interaction with molecules, probing very fast chemical reactions, time-resolved dynamics of molecules and clusters, dynamics of photoexcited charge carriers in semiconductors, material science, and environmental, biological, and medical studies. Ultrafast laser light sources produces peak emission powers on the order of petawatts in a pulse duration less than 10 fs, directly from simple laser. This high emission leads to peak power equivalent to that produced at nuclear power plants and greater than that of the entire solar flux incident onto pinhead. The amplifier gain media is a titanium-doped sapphire (Ti: sapphire) crystal. Ti:sapphire was selected because of its two very useful properties:(a) it has a broad absorption band in the blue and green, which allows it to be pumped by the frequency-doubled output of a Nd:YLF or a Nd:YAG laser, the absorption band of the laser is from 400 nm to 630 nm with peak absorption at 490nm, and (b) Ti:Sapphire emission spectrum ranges from 660-1180nm and is tunable within this range, shown in Fig. 45.

Ti:sapphire is a crystalline material produced by introducing Ti_2O_3 into a melt of Al_2O_3 , where Ti^{3+} (titanium) ions replace a small percentage of the Al^{3+} (aluminum) ions.

The Ti^{3+} ion is responsible for the lasing action in Ti: sapphire. The electronic ground state of the Ti^{3+} ion is split into a pair of vibrationally broadened levels.

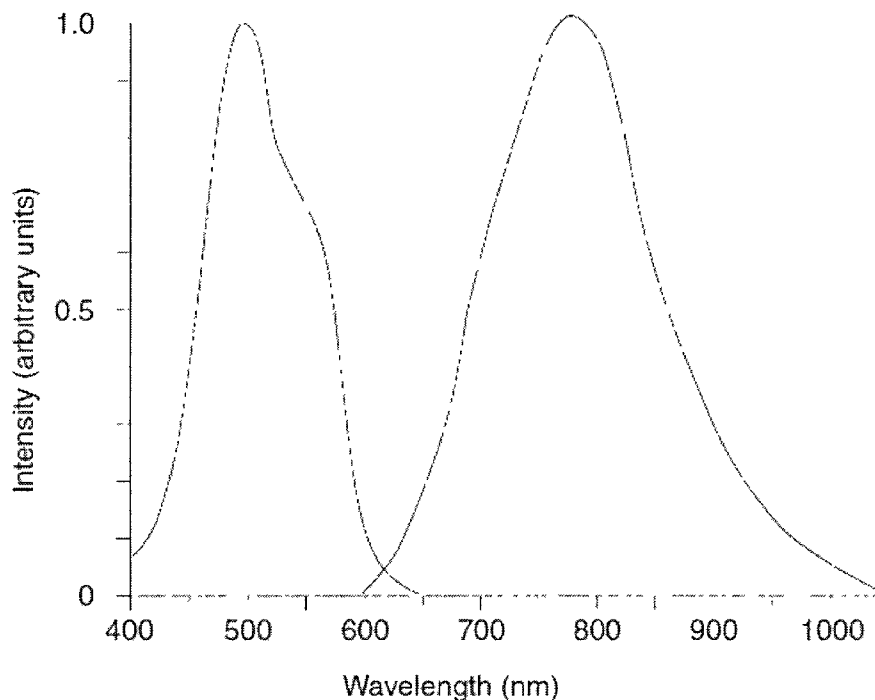


FIG. 45. Absorption and emission spectra of Ti:Sapphire.

Absorption transitions occur over a broad range of wavelengths from 400 to 600 nm (only one of which is shown in Fig. 45). Fluorescence transitions occur from the lower vibrational levels of the excited state to the upper vibrational levels of the ground state. The resulting emission and absorption spectra are shown in Fig. 45. Although the fluorescence band extends from wavelengths as short as 600 nm to wavelengths greater than 1000 nm, lasing action is only possible at wavelengths longer than 670 nm because the long wavelength side of the absorption band overlaps the short wavelength end of the fluorescence spectrum. Additionally, the tuning range may be reduced by variations in

mirror coatings, tuning element losses, pump power, and pump mode quality. Nevertheless, Ti:sapphire possesses the broadest continuous wavelength tuning range of any commercially available laser. This broad tuning range allows Ti:sapphire lasers to produce and amplify optical pulses of extremely short duration. As a corollary, the same factors that allow Ti:sapphire a broad, tunable wavelength range might also affect the production and amplification of these ultrashort pulses. The Ti:sapphire crystal is known to have high resistivity to thermally induced stress which is the reason to be optically pumped at relatively high average powers without danger of fracture. However, it can't handle the high peak powers that would result from directly amplifying femtosecond pulses. A technique called chirped pulse amplification (CPA), which temporally stretches the pulse prior to amplification and then recompresses it following amplification, circumvents this limitation.

C.2. CHIRPED PULSE AMPLIFICATION

When an intense beam travels through a Ti:sapphire crystal, it tends to “self-focus.” Self-focusing is a nonlinear optical effect in which an intense light beam modifies the refractive index of the material it is passing through, causing the beam to focus and intensify even further. This can potentially result in a run-away condition that causes permanent damage to the crystal. Therefore, self-focusing makes it necessary to limit the peak power of a pulse in the Ti:sapphire crystal to less than 10 GW/cm^2 . Chirped pulse amplification (CPA) allows a Ti:sapphire crystal to be used to amplify pulses beyond this peak power, while keeping the power density in the amplifier below the damage threshold of the crystal. CPA is accomplished in three steps, shown in Fig. 46. The first step stretches the very short seed pulse that is supplied by a stable, mode-locked

picosecond or femtosecond laser. The term mode-locked refers to the laser operating in a manner in which a set of frequencies (modes) are locked in phase and destructively interfere everywhere within the cavity except at one point in the cavity where the frequencies add together to create the pulse. Stretching the pulse (i.e., increasing its duration) reduces its peak power, which greatly reduces the probability of damage to the Ti:sapphire amplifier crystal.

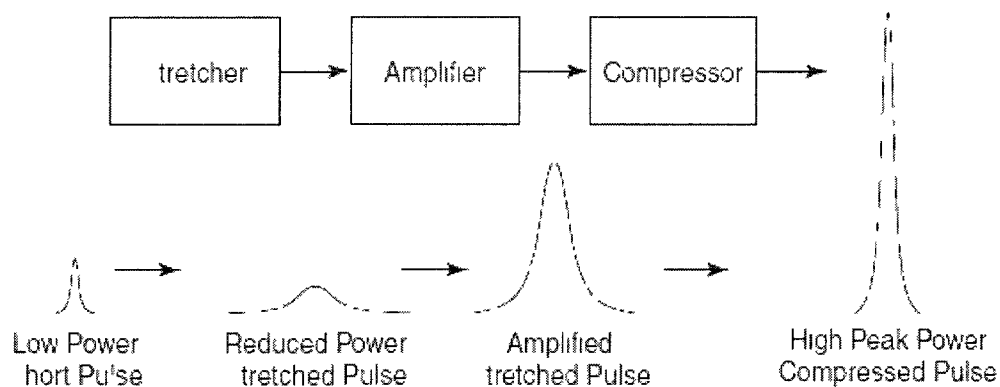


FIG. 46. Principle of chirped pulse amplification (CPA).

The second step amplifies the stretched pulse: a pump laser provides a synchronous energy pulse to the Ti:sapphire crystal to excite it just prior to the arrival of the stretched seed pulse. The seed pulse causes stimulated emission, which amplifies the pulse at the same wavelength and direction. (This is, in contrast to “spontaneous emission”, within the gain medium that typically is amplified to become laser output in other systems.) The third step recompresses the stretched, amplified pulse as close as possible to its original duration. The fundamental relationship that exists between laser pulse width and bandwidth is that a very short pulse exhibits a broad bandwidth, and vice versa. For a Gaussian pulse, this relation is given as

$$\Delta\nu \cdot \Delta t > 0.441 \quad (37)$$

where $\Delta\nu$ is the bandwidth and Δt is the laser pulse width. As it can be seen from the equation, the longer the bandwidth is, the shorter the output pulse is. For example, for a 100 fs duration pulse at $\lambda = 800$ nm, the corresponding bandwidth is more than 9 nm. Therefore, a device that can delay certain frequencies (or wavelengths) relative to others can stretch a short pulse so that it lasts a longer time. Likewise, such a device should also be able to compress a long pulse into a shorter one by reversing the procedure. The phenomenon of delaying or advancing some wavelengths relative to others is called group velocity dispersion (GVD), shown in Fig. 47, or, less formally, “chirps.”

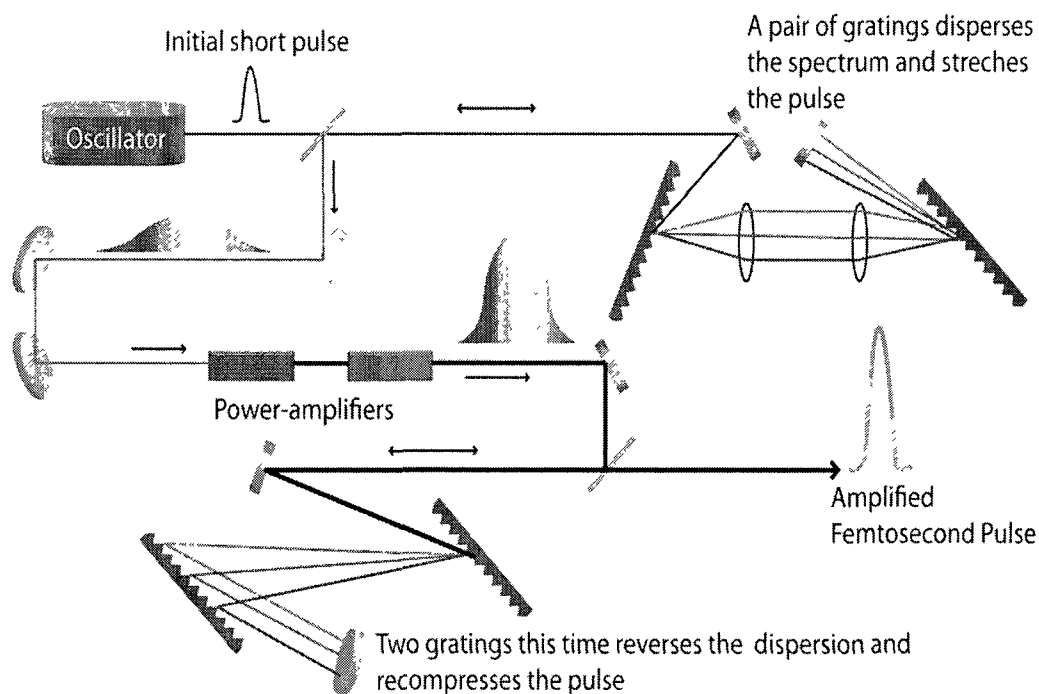


FIG. 47. Principle of pulse stretching using negative GVD.

A pulse is said to have positive GVD, or to be positively chirped, when the shorter (bluer) wavelengths lead the longer (redder) wavelengths. Conversely, if the bluer light is delayed more than the redder light, it has negative GVD or chirp. For CPA, a combination of dispersive optics are used to form a “pulse stretcher” where low-energy, short-duration pulses can be lengthened by as much as 10^4 . Then the energy in these pulses is increased by passing them. A light pulse incident on a diffraction grating experiences dispersion; that is, its component wavelengths are spatially separated, and so too are its frequency components. The dispersed spectrum can be directed through a combination of optics (usually the same diffraction grating can be used) to send the different frequencies in slightly different directions. Longer (or redder) wavelengths can be made to travel over a longer path than the shorter (or bluer) wavelengths components of the beam, or vice versa. The result is to lengthen the duration of the pulse, which reduces its peak power (it is the same energy under the curve, only spread out more now). A prism, which is a simpler optic than a diffraction grating, can also be used for these purposes. However because the pulse passes *through* a prism, negative GVD is introduced by the glass or quartz of the prism body— blue frequencies are delayed relative to the red frequencies each time the pulse passes through the prism. Therefore, gratings are the better choice for CPA because they simplify the process of compensating for dispersion caused by other components in the optical path. The grating and the routing mirrors can be chosen so that, in the stretcher, the bluer frequency components of the spectrum travel further than the redder components, causing the redder frequency components to exit the stretcher first. In the compressor, the spatially spread beam is

flipped so that the redder component have to take the long path, thereby allowing the bluer frequencies to catch up. This recompresses the pulse. A short pulse is spectrally spread and then, by making one end of the spread pulse travel farther than the other end, the pulse is temporally broadened. The same optical components act as a compressor when the leading component of a temporally stretched pulse is forced to take the longer path, thereby allowing the trail-stretcher amplifier compressor.

C.3. OPERATION

Our laser system consists of oscillator and amplifier which consist of stretcher, amplifier, and compressor. We do have three chillers: one for the oscillator, one for pump laser Darwin, and the other big one to help Darwin chiller and to cool down controller. One should follow the following procedure to turn on the oscillator and amplifier.

- First turn on the chiller for oscillator. Once temperature is around 20 °C, turn the key clockwise and a bit forward as you start car.

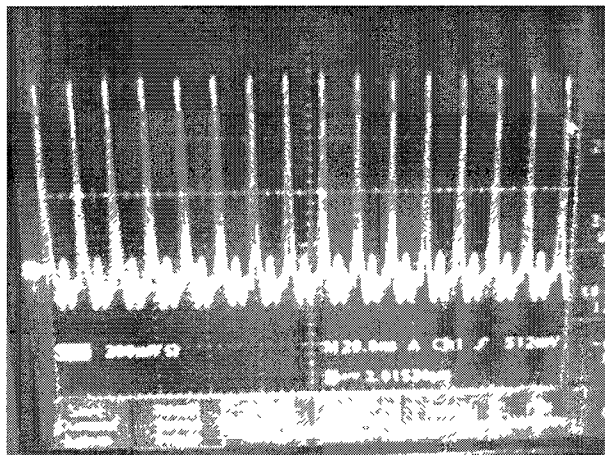


FIG. 48. Photodiode signal from oscillator shows modelocking.

- Choose “start with last current”.

- Once current reaches the set point, click modelocking button at the back of the oscillator. Just to make sure, pulse train is ok; check it in long time range, you should see something like in Fig. 48. You may get a good individual pulse in short time interval. This may not give you accurate result. Increase the time scale, pulse train should have straight pulses if modelocking is obtained properly.

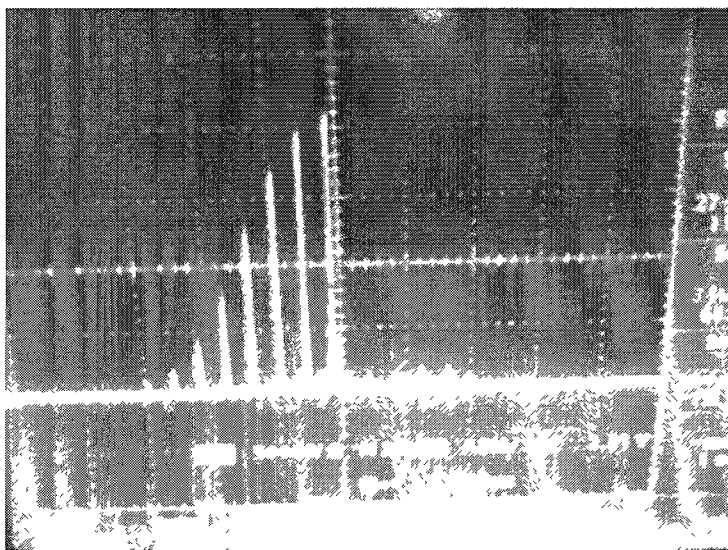


FIG. 49. Pulse train from amplifier.

- Once you check spectrometer, pulse train and power from oscillator then you can go ahead and start the amplifier.
- Turn on big chiller which is dedicated to amplifier.
- Turn the key clockwise and a bit further. Wait ~10 minutes for amplifier to warm-up. You may have error sign on Darwin chiller display upon starting the amplifier. That should be gone in couple of minutes.
- After ~10 min, click Menu and set the temperature to 18.0 °C.

- Select PRF source from internal to external.
- Once temperature is around $\sim 18.0 \pm 0.1$, open the shutter and increase the current value slowly to ~ 30.4 A.

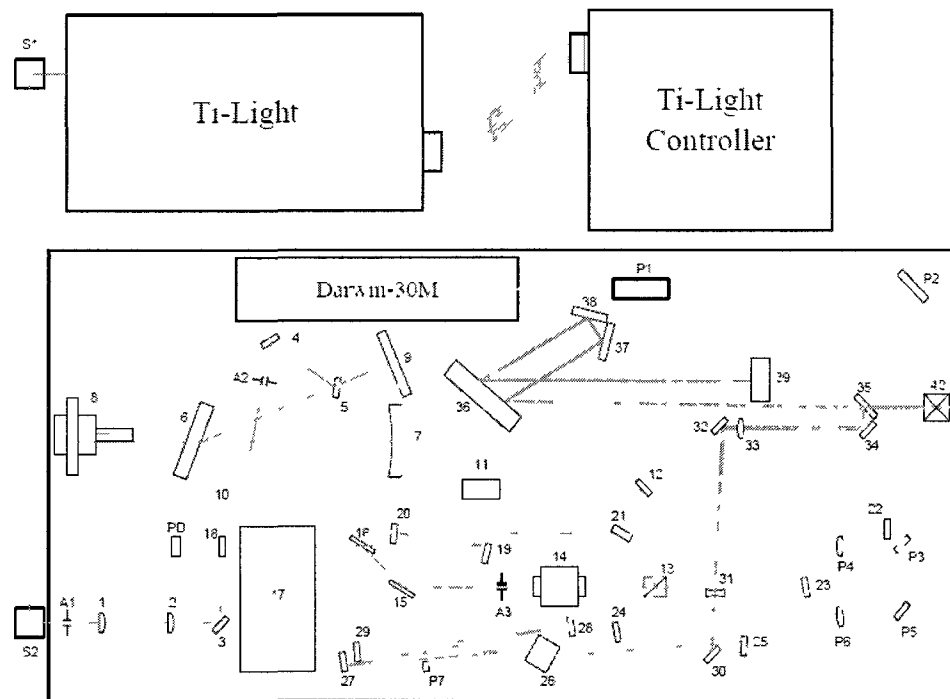


FIG. 50. Amplifier beam path.

Watch out pulse train from amplifier. If necessary, touch two pump mirrors in amplifier to have a better pulse train shape, shown in Fig. 49. To optimize power and shape, touch three mirrors in multipass while watching the power, shown in Fig. 50. Note that the most stable performance is obtained by adjusting the timing (V_b controls the cavity dumping time) so that the pulse train includes the one pulse that is just past the maximum.

C.4. MAINTENANCE

- Clean the crystal when power drop accelerates or mode locking becomes difficult
- Tune-up of CW power ONLY at the CW-max position 11.90mm – this is not always necessary after crystal cleaning, the less tune-up the better
- For tune-up use only the output coupler, whenever power is optimized, bring to CW-max position and double check mode-locked has stopped
- After tune-up of Ti-Light the amplifier seed input mirrors may need to be tweaked
- If repeatedly cleaning does not improve performance and strong green scattering remains on the first surface, move the crystal a very small distance with the special tool – do not move just to improve power
- Upper limit for N₂ flow rate ~2 liters per minute, keep lowering it to see if still effective
- Possible to stop N₂ when the green pump is off
- Teflon tube for N₂ better than Tygon (organic out gassing)
- Main parameter about purging: clean, no dust, no organic compounds (oil!)

C.4.1. TI-LIGHT PERFORMANCE

Ti-Light output: ~360 mW mode locked, ~220mW when out of ML, ~600mW at CW-position mode locking stable now, over wider range of C2 position, easy to start mode lock output power amplifier shown with customer power meter: 2.30-2.40 W

C.4.2. TI-LIGHT SETTINGS

Do not change: set current: 15.1 A; chiller water: 20.0 °C, C1 position: 1.85mm, pump lens position: 6.06mm prism position: 69mm, slit fully open, **only** touch

when spectrometer is used to see spectrum. C2 CW-max position 11.90mm (slightly higher CW power may be possible at other position, but stay here!)

ML position: 12.10mm - +/- 5 divisions (+/- 0.05mm) possible and still mode lock

C.4.3. TI-LIGHT OPTIMIZATION

After turning on the laser system, wait around 15 min for Colibri warm-up. Don't forget to turn on the chiller although it is not an essential part for oscillator operation, it is important for stability and performance.

C.4.4. OPTIMIZATION PROCEDURE

If modelocking gets worse, and cleaning of the crystal and optics don't do that much, you have to optimize the power. Please follow the steps below very carefully.

- Write down all micrometer settings for your reference (This is extremely important!!!).
- Fully open the slit.
- Stop modelocking by blocking the beam inside the cavity and then measure the CW power.
- Move the second curved mirror to CW max position (away from crystal, farther from green laser). This is generally around 20 divisions from ML position.
- Optimize the CW-power by adjusting one of the end mirrors. Output coupler first and then high reflector. Use the horizontal key first.
- Maximize the power. You don't have to move OC and HR too much to maximize the power. Most of the times, just a little bit touch should be enough.
- Find the modelocking range by doing the following steps.

- ❖ Move second curved mirror closer to the crystal again in small steps, first 3-4 divisions and then 1 division as you approach old ML position.
 - ❖ In each step, push the prism and watch the spectrum to see if you can get modelocking.
 - ❖ Write down first ML position. At this position, you may see Gaussian pulse with a spike on the edge. This generally occurs at the outer edge of the modelocking range.
 - ❖ Keep moving the mirror until you get inner edge of ML range. Normally, you should have ~10 division of clear modelocking range.
- Check the difference between ML and CW power. ML power should always be higher than CW-power.
 - Check the spectrum to see center wavelength, if necessary, move the prism accordingly.
 - Narrow the slit again.

Alternatively, you can do fine alignment as follow. But in this case, you should be very careful as it is very sensitive.

- Open the slit, and then check the spectrum is roughly where you want it. Don't worry too much about being at 780-790, it can be fine tuned later
- Try to really see the green and IR spot with the IR-viewer as I described on the phone. Locking at the first curved mirror (from the direction of the sapphire crystal) both spots have to be at the same horizontal level and the IR has to be just on the right side of the green. The green spot is really weak in the IR viewer, but it should be possible to see it weaker and smaller than the IR. To make it stand

out, block and unblock the IR cavity as we talked about. It is not easy to judge how close together they should be, so try the following strategy (but make sure they are in the same horizontal line!).

- Put the alignment keys in both HR and OC for the horizontal adjuster (lower one), and as always be at the cw-max position for power optimization.
- Then pick a direction for the HR, e.g. clockwise, and go a small bit, like 5min turn on the clock.
- As a result the power will drop slightly, now max it back up with the other mirror, the OC. This way you walk the cavity and the overlap will change.
- Don't worry too much about the absolute cw power for now
- now translate the C2 back towards ML range and find out the ML range as we discussed: the residual cw peak disappears on the "outer" edge, and the inner edge is defined by the laser losing ML again
- Write down how many divisions.
- Then repeat the process, by going back to cw-max, keep moving the key in the HR the next tiny step.
- If the picked direction for the HR key was wrong, i.e. the ML gets worse, try going the other way.

In this way it is searching for optimal ML behavior in a systematic way, not just with the cw power as a feedback, but rather the ML range to be expanded. It is more work, and it may take a while, so patience is also needed, unfortunately. While you do this, try to see the IR/green spots in the IR viewer, it will take some practice.

C.5. IMPORTANT NOTES

- Do not re-optimize the power with the mirror position in ML-range, no matter if it is in CW or ML.
- Always, power optimization must be done at least 10 divisions away from modelocking position since we want laser to prefer ML over CW.
- It is good to clean crystal, *only if* necessary. You must exercise extreme caution when doing that. Fold a lens tissue carefully so that you can have tip at the end. This should be smaller than crystal surface size so that when you clean it, you don't touch indium foil. Otherwise, you can get crystal dirty.
- If modelocking power drops in long term operation, always check if crystal needs to be cleaned. In that case, kill ML, block pump laser by blocking and then clean the crystal. Normally, when you push prism, you should get modelocking again.

C.6. DIAGNOSTIC RECOMMENDATIONS

- Set up power meter and spectrometer to operate simultaneous while Ti-Light is seeding the amplifier
- Spectrometer and display dedicated to oscillator
- Simple oscilloscope to permanently monitor build-up in regenerative amplifier
- Auto-correlator to measure pulse length

VITA**Ali Oguz Er**

PhD

Physical Electronics Research Institute
Department of Physics, Old Dominion University
Norfolk, VA 23529, USA
757-676-2414
aerxx001@odu.edu
<http://www.alioquzer.com>

Education

- Ph.D. Old Dominion University
Physics, Norfolk, VA, April 2011
- M.Sc. Old Dominion University
Physics, Norfolk, VA, May 2005
- B.Sc. Middle East Technical University
Physics, Ankara, Turkey, December 2003

Publications**Journal Articles**

1. **Ali Oguz Er** and Hani Elsayed-Ali, *Excitation-induced Ge quantum dot formation on Si(100)-2x1*, Journal of Applied Physics 108, 034303-10 (2010)
2. **Ali Oguz Er**, Wei Ren, and Hani Elsayed-Ali, *Low temperature epitaxial growth of Ge quantum dot on Si(100)-2x1 by femtosecond laser excitation*, Applied Physics Letters 98, 013108-3 (2011) [selected for February 2011 issue of **Virtual Journal of Ultrafast Science**]
3. **Ali Oguz Er** and Hani Elsayed-Ali, *Electronically enhanced surface diffusion during Ge growth on Si(100)*, Journal of Applied Physics 109, 084320-6 (2011)
4. **Ali Oguz Er** and Hani Elsayed-Ali, *Femtosecond pulsed laser deposition of Ge quantum dot growth on Si(100)-(2x1)*, Applied Surface Science 257, 8078-8084 (2011)
5. **Ali Oguz Er** and Ashraf Farha, *Generation of plasma plume from Ge target by nanosecond laser*, IEEE Transaction on Plasma Science (In Press)